



**HAL**  
open science

# Fabrication of suspended plate MEMS resonator by micro-masonry

Adhitya Bhaswara

► **To cite this version:**

Adhitya Bhaswara. Fabrication of suspended plate MEMS resonator by micro-masonry. Micro and nanotechnologies/Microelectronics. Université Toulouse III Paul Sabatier, 2015. English. NNT : . tel-01291780v1

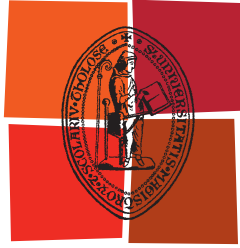
**HAL Id: tel-01291780**

**<https://theses.hal.science/tel-01291780v1>**

Submitted on 22 Mar 2016 (v1), last revised 14 Dec 2016 (v2)

**HAL** is a multi-disciplinary open access archive for the deposit and dissemination of scientific research documents, whether they are published or not. The documents may come from teaching and research institutions in France or abroad, or from public or private research centers.

L'archive ouverte pluridisciplinaire **HAL**, est destinée au dépôt et à la diffusion de documents scientifiques de niveau recherche, publiés ou non, émanant des établissements d'enseignement et de recherche français ou étrangers, des laboratoires publics ou privés.



Université  
de Toulouse

# THÈSE

En vue de l'obtention du

## DOCTORAT DE L'UNIVERSITÉ DE TOULOUSE

Délivré par :

Université Toulouse 3 Paul Sabatier (UT3 Paul Sabatier)

---

**Présentée et soutenue par :**

**Adhitya BHASWARA**

Le mercredi 25 novembre 2015

**Titre :**

Fabrication of Suspended Plate MEMS Resonator by Micro-Masonry

---

ED GEET : Micro et Nanosystèmes

**Unité de recherche :**

Laboratoire d'analyse et d'architectures des systèmes (UPR 8001)

**Directeur(s) de Thèse :**

Docteur Liviu NICU

Docteur Thierry LEICHLE

**Rapporteurs :**

Professeur Isabelle DUFOUR

Docteur Lionel BUCHAILLOT

**Autre(s) membre(s) du jury :**

Professeur Frederic MORANCO - Examineur

Docteur Vincent AGACHE - Examineur



Ever tried.

Ever failed.

No matter.

Try again.

Fail again.

Fail better.

- *Samuel Beckett*



# Acknowledgement

I would like to first and foremost thank my supervisors, Thierry Leichle and Liviu Nicu, for giving me a chance to do a Ph.D, after being away from science for around a year. I found their guidance and care for the graduate students uncommon and welcome surprise, and this shows in the relatively high satisfaction level and performance of their graduate students. Their knowledge in the subject matter is deeply appreciated and helpful for students which come from diverse scientific backgrounds. Both of them are a good role model on what it means to become a teacher and a scientist. Special thank is given to Thierry for dealing with review and revision of my thesis and scientific papers, which is expensive in time and energy due to my inexperience. Their competence results in them being put in position of higher responsibilities, which I believe will benefit LAAS in particular and scientific community in general. I wish them success in their future live and career.

Extended gratitude is given to all faculty members of nanobiosystems (NBS) group of LAAS. Their contribution in form of discussions and feedbacks is influential to the quality improvement of this work. I would like to give special thanks to Bernard Legrand who, although not formally listed as a supervisor, has given significant contribution into my understanding of microsystems and measurement systems in general. His joining in the NBS group at LAAS is a welcome surprise, and let us identifies problems that have remained for months. I am convinced that future students will find his guidance valuable and helpful during their studies and beyond. I would also like to thank the jury members for their feedback and valuable insight.

As with the majority of experimental science projects, most of the students' time is spend for bench work, whether for fabrication or characterization of samples. As such, credit to the support staff which helped me a lot during my studies is in order. I would like to thank members of TEAM for their support, especially Adrian, Aurelie, Benjamin, Bernard, David, Laurent, Ludovic, and Pascal. I would also like to thank Fabrice, whose expertise in electronics and measurement systems influences the device design of this study. Their formal and tacit knowledge regarding specific processes, although intangible, is invaluable to the success of this work as a whole.

This work would not be started, let alone finished, without the involvement from our collaborators from University of Illinois at Urbana-Champaign: Prof. Seok Kim along with his graduate students Anthony Hohyun Keum and Sang Il Rhee. Their specialty in micro-masonry technique, which is unique among all microfabrication techniques, makes this project possible. I would like to thank them for perfecting the micro – masonry process and identifying and solving new problems that arises during this study. They would be delighted to hear that during the thesis defence, some of the jury members are interested in applications of micro-masonry for other types of MEMS devices. I wish that collaboration between us would continue to provide fruitful results.

I have travelled far and long in the pursuit of my studies, both on the occident and on the orient. In all cases, I have learned different languages (with mixed results) and cultures, some of which are opposite of the other. About the common thing I have obtained is friends with varying backgrounds and interesting personalities, and this three years in France is no different. I would like to thank fellow graduate students of LAAS, inside and outside of NBS team: Aude, Yingning, Denis, Pattamon, Rafael, Laurene, Valentina, Carlos, Sabrina, Cecile, Maxim and Aliko for mind-opening discussions, companionship and moral support. I have learned much from all of them, especially the value of perseverance and good work ethic in face of adversity. The experiences and memories they have given me is a treasure I will cherish in the future. I wish them all the best for their lives and their future career.

I thank my family back at home in Indonesia for distant morale support and encouragement. Homesickness is a common problem that affects foreign students, especially those that has been away from home for many years. Personally this has been not a problem that affects me, and while this may be the result of mild case of Asperger's, some parties helped to make Toulouse home away from home. I would like to thank the Indonesian Student Association in Toulouse for providing moral support, especially in form of delicious foods and conversation in my mother language. Most importantly, I would like to thanks to my French "family", my landlady Mrs. Christiane Fontas and my housemates: Tiangang, Donju, Fred, Alexhandro, Fei, and Reza. I wish you the best in whatever place you chose to build your life, and I hope we will meet again one day. This meeting with my adopted family would not be possible were it not for Mrs. Catherine Stasiulis of the International Office of UPS, and for this and countless amount of support, I would extend my heartfelt thanks to her.

Similar to most research work, this thesis is far from perfect, and the responsibility for all errors and mistakes belongs to me. Indeed, this work would most probably be read (if being read at all) by a graduate student, most probably in search for a solution to a problem which needs to be solved before s/he needs to graduate. Some of these students might feel that their work is inadequate and considering to quit their studies. For these students, I would like to conclude my acknowledgement here by quoting my favourite story about perfection, which is called "the parable of the black belt":

*Picture a martial artist kneeling before the master sensei in a ceremony to receive a hard-earned black belt. After years of relentless training, the student has finally reached a pinnacle of achievement in the discipline.*

*"Before granting the belt, you must pass one more test," says the sensei. "I am ready," responds the student, expecting perhaps one final round of questioning. "You must answer the essential question: What is the true meaning of the black belt?"*

*"The end of my journey," says the student. "A well-deserved reward for all my hard work." The sensei waits for more. Clearly, he is not satisfied. Finally, the sensei speaks. "You are not yet ready for the black belt. Return in one year."*

*A year later, the student kneels again in front of the sensei. "What is the true meaning of the black belt?" asks the sensei.*

*“A symbol of distinction and highest achievement in our art,” says the student. The sensei says nothing for many minutes, waiting. Clearly, he is not satisfied. Finally, he speaks. “You are still not ready for the black belt. Return in one year.”*

*A year later, the student kneels once again in front of the sensei. Once again, the sensei asks: “What is the true meaning of the black belt?”*

*“The black belt represents the beginning – the start of a never ending journey of discipline, work, and the pursuit of an ever-higher standard,” says the student.*

*“Yes. You are now ready to receive the black belt and begin your work.”*

The morale of the story is simple: Ph.D is the beginning, not the end. A student should finish it as best as he can, as soon as possible, and pursue continuous improvement beyond his studies. Thus, being a gamer and a geek myself, I would revise my closing remarks from

~~Congratulations ! You have beaten the boss and completed the game!~~

Into

Tutorial completed.

The financial support NANOBIOD-2013 from the INSIS-CNRS is gratefully acknowledged. This work was partly supported by the French RENATECH network.



# Table of Contents

Table of Contents .....	1
Introduction .....	5
Chapter 1 .....	7
1.1 Brief description and history of MEMS .....	8
1.2 Common MEMS structures.....	12
1.3 Applications of Suspended plates.....	15
1.3.1 Mass sensors.....	15
1.3.2 Pressure sensor .....	18
1.3.3 Acoustic sensors and actuators.....	21
1.3.4 Actuators in Microfluidics.....	23
1.4 Common fabrication methods of suspended plates .....	25
1.4.1 Bulk micromachining .....	25
1.4.2 Surface micromachining techniques.....	27
1.4.3 Wafer bonding technique .....	28
1.5 Micro masonry as a method to fabricate suspended structures .....	29
1.6 Basic concept of the thesis project .....	31
1.8 Summary .....	33
References .....	34
Chapter 2 .....	39
2.1 Theoretical considerations.....	40
2.1.1 Basic theory of vibrations.....	40
2.1.2 Q factor as a measure of dissipation.....	43
2.1.3 Theoretical description of molecular damping.....	45
2.1.4 Theoretical description of squeeze film damping .....	47
2.1.5 Fundamental frequency of a vibrating plate .....	50
2.2 Design and fabrication of suspended structures using micro-masonry. ....	52
2.2.1 Design and fabrication of the passive structures .....	52
2.2.2 Design and fabrication of the active devices .....	58
2.3 Summary .....	63
References .....	64
Chapter 3 .....	67
3.1 Overview of dynamic optical measurement systems .....	68

## Table of Contents

3.1.1 Strobe video microscopy .....	68
3.1.2 Laser doppler vibrometry .....	70
3.1.3 Fabry-Perot interferometry .....	71
3.2 Calibration of Fabry-Perot interferometer using thermal noise.....	74
3.3 Calibration of Fabry-Perot cavity using harmonics.....	75
3.4 Overview of electrical measurement .....	76
3.4.1. Fundamentals of parallel-plate capacitive resonator .....	77
3.4.2 Compensated capacitive measurement technique .....	79
3.5 Experimental setup and equipment .....	80
3.6 Summary .....	80
References .....	81
Chapter 4 .....	83
4.1. Failure modes in devices fabricated using the micro-masonry technique.....	84
4.1.1 Buckling of the nanoplate structures .....	84
4.1.2 Delamination of the nanoplate structures .....	85
4.1.3 Yield of the micro-masonry process.....	91
4.2 Measurement results for passive structures .....	92
4.2.1 Characterization of single cavities in vacuum.....	93
4.2.2 Characterization of single cavities in varying air pressure.....	99
4.2.3 Characterization of multiple cavities in vacuum .....	104
4.2.4 Characterization of multiple cavities in atmospheric pressure .....	105
4.3 Characterization of active devices.....	107
4.3.1 Optical characterization of active devices .....	108
4.3.2 Capacitive characterization of active devices.....	109
4.3.3 Variation of peak height and resonant frequency with respect to $V_{DC}$ .....	110
4.3.4 Stress in active devices.....	111
4.3.5 Q factor of active devices in atmospheric pressure and in vacuum.....	111
4.4 Other Results .....	112
4.4.1 Base structure fabrication using PECVD and thermal oxide .....	112
4.4.2 Passive structure fabrication with thick plates .....	113
4.4.3 Transfer printing of silicon plates onto gold surface.....	115
4.4.4 Modelling of laser heating using COMSOL .....	116
4.4.5 Effective parameter determination using Fabry-perot setup .....	118
4.5 Summary .....	120
References .....	121
Chapter 5 .....	123

Table of Contents

5.1 Conclusion..... 124

5.2 Perspectives for Future Work..... 125

Appendix A ..... 127

Appendix B ..... 145

Table of Contents

# Introduction

Micro-electro mechanical systems (MEMS) are microscale structures that contain both mechanical and electrical elements. MEMS devices are used in a wide range of applications, from consumer electronics to automotive devices in the form of accelerometers, gyroscopes, projection displays, and mass sensors. The mechanical structures commonly used in MEMS devices include cantilevers, bridges, trampolines, suspended plates, and wine glass structures. The unique property of suspended plate structures that is not shared with other mechanical structures is the possible presence of a sealed cavity, which can contain vacuum, gas, or liquid between the plate and the substrate. This property is utilized in various applications such as pressure sensors, acoustic transducers, microfluidic actuators, or biosensors operating in real-time in liquid.

Several techniques exist to fabricate suspended structures such as bulk micromachining, surface micromachining, and wafer bonding. In bulk micromachining, the substrate itself is used as the plate material, and some part of it is etched away to form a suspended structure. In surface micromachining, the suspended plate is formed on top of the substrate by deposition of material on top of a sacrificial layer, which is etched away to form a suspended structure. In wafer bonding technique, a silicon on insulator (SOI) wafer is used as the plate material, while another wafer with etched cavities is used as the suspending structure. Both wafers are anodically bonded together, and the bulk and buried oxide layers of the SOI wafer are etched away to reveal the suspended plate structure. Each of these techniques has its own limitations, such as possible stiction as a failure mode, involvement of complicated processes, and limited selection of materials for the plate constituent.

Micro-masonry is a simple technique that offers a unique alternative that overcomes some of these limitations. In this technique, a special stamp with a reversible adhesion is used to transfer a material from one substrate to another, which is then permanently bonded by thermal annealing. The ability of the technique has been demonstrated by fabricating static and quasistatic structures such as stacks of silicon nanoplates and electrostatic switches.

This study explores the potential of micro-masonry as a simple and straightforward fabrication technique for suspended structures used as mechanical resonators. Background information regarding suspended structures such as most relevant applications, basic theory, and current methods of fabrication are first reviewed. Two kinds of suspended plate resonators are then presented and fabricated: passive structures and active devices with integrated capacitive actuation and sensing. Finally, we discuss the characterization results of both devices in terms of performances and limitations.



# Chapter 1

## Background

*In this chapter, we present the background and motivations of our study, which consists in investigating the possibility of using micro-masonry for the realization of nanoplate resonators with integrated actuation and detection schemes and assessing the advantages and the drawbacks of this approach. To this aim, first, we provide a general description of micro-electro mechanical systems (MEMS) and structures that are commonly used in MEMS are presented with examples of their applications. We then focus our discussion on the type of structures that are addressed in this work: the suspended plates. Fabrication methods commonly used for the fabrication of suspended plates are listed and micro-masonry is then presented as an alternative fabrication method to create such MEMS structures. Finally, the objectives of this thesis and a summary of each chapter of this manuscript are presented.*

## 1.1 Brief description and history of MEMS

Micro-Electro Mechanical Systems (abbreviated as MEMS) is a term referring to a group of devices that contains mechanical and electrical elements having size in the micrometer range (typically between 1 mm – 1  $\mu$ m). MEMS manufacturing techniques are derived from the fabrication technologies developed for the semiconductor industry, such as etching and thin film deposition. MEMS devices are typically employed as miniature transducers, which include sensors such as accelerometers, gyroscopes, or microbalances (mass sensors), and actuators such as RF switches, speakers, micropumps, and microvalves. Further development and miniaturization of these devices led to Nano-Electro Mechanical Systems (NEMS), which operate at the nanoscale (size < 100 nm) and are now the source of active research.

The history of MEMS is tightly related to the history of the semiconductor industry, which major milestones include the invention of the integrated circuit (IC) by Jack Kilby [1] from Texas Instruments in 1958. Before the invention of the IC, the basic electronic components such as transistors, capacitors, inductors, resistors, and wires were fabricated separately before being assembled together to form an electrical circuit. This approach was time consuming, and the whole assembled structure had a large footprint due to the relatively large size of both the components and the packaging necessary to protect them. The integrated circuit is an approach where the different components necessary to form an electrical circuit are fabricated in a single substrate, resulting in a compact device containing all of the functionalities of a traditional device assembled from separate components. The first IC in the world is shown in Figure 1.1.a ; it was made on a germanium chip, containing 1 transistor, 1 capacitor, and 3 resistors. Further development of this idea led to the invention of the first silicon IC shown in Figure 1.1.b by Robert Noyce [2] from Fairchild semiconductors in 1961. The adoption of silicon is a significant step for the semiconductor industry; while inferior to germanium in terms of electrical properties, silicon is cheaper and easier to process than germanium. This started the age of research and development of electronic component miniaturization among semiconductor companies, mainly due to economic reasons. Assuming same functionality, smaller components reduces the cost associated to the electronic-grade materials, which is expensive due to the high level of purity needed. Processes such as photolithography, wet etching, reactive ion etching, evaporation, and sputtering techniques were developed with this end in mind.

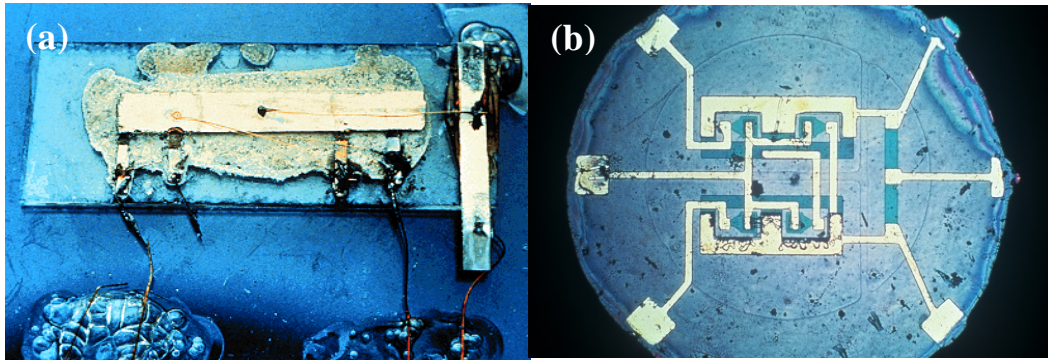


*Figure 1.1. (a) The first integrated circuit (IC) in the world, invented by Jack Kilby from Texas Instruments in 1958. The IC was fabricated on top of a germanium wafer, and it contained 1 transistor, 1 capacitor, and 1 resistor [3]. (b) The first silicon integrated circuit in the world, invented by Robert Noyce from Fairchild Semiconductors in 1961. The invention of IC leads to development of modern semiconductor fabrication technique in quest for miniaturization, which would be used to create MEMS devices afterwards [4].*

Around the same time period, another spark of MEMS development came from academia. In 1959, Nobel Prize laureate Richard Feynman gave his famous lecture “There’s plenty of room at the bottom” [5]. Ahead of his time, Feynman discussed some basic concepts of microfabrication: microcontact printing, ion beam lithography, photolithography, compact disc technology, laser, radio frequency (RF) technology and metal and oxide evaporation. He also discussed about problems that might be encountered at such a small scale and in fact would be encountered decades later, including homogeneity of materials, problems of resolution, dominance of surface effects, and heat generation in integrated circuits. Of special interest was the discussion of micromachines, which included medical implants (“You put the mechanical surgeon inside the blood vessel and it goes into the heart and ”looks” around“) and micro-actuators (“a billion little lathes”). The lecture ended with the presentation of two challenges: the first one was to build a micromotor (“a rotating electric motor which can be controlled from the outside and, not counting the lead-in wires, is only 1/64 inch cube”) and the second one was to write in nanoscale (“take the information on the page of a book and put it on an area 1/25,000 smaller in linear scale”). The first challenge was met within 6 months of the lecture by William Mclellan [6], who fabricated the motor using contemporary bulk machining techniques (Figure 1.2.a). The second challenge, considerably more difficult, was achieved 15 years later by Tom Newman using electron beam (E-beam) lithography techniques (Figure 1.2.b) [7].

The MEMS device was born when it was realized that the fabrication technologies used to manufacture ICs could also be used to manufacture mechanical devices. The first patented MEMS device is the resonant gate transistor (Figure 1.3), which was conceived in 1965 by Harvey Nathanson from Westinghouse [8]. The resonant gate transistor is a cantilever switch

actuated by electrostatic principles; when the device is at resonance, a closed electrical circuit is created, thus making it a form of mechanical frequency filter. It was fabricated by repeated deposition and selective etching of materials, with some materials acting as a supporting layer for the structural material. Thus, this first MEMS device is also the first microcantilever, the first microcapacitive device, the first micro-RF device, and the first mechanical device fabricated using surface micromachining technologies.

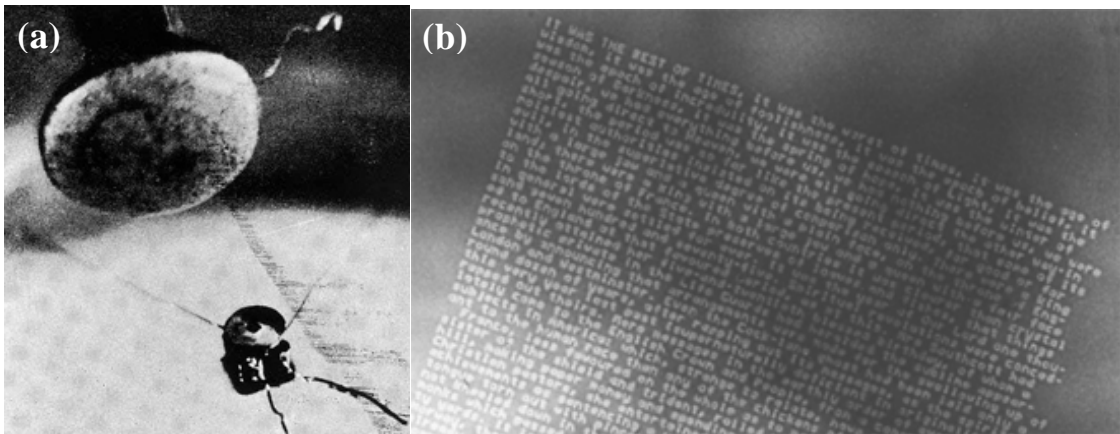


Figure 1.2. (a) One of the first micromotors in the world, fabricated by William McLellan in 1960. The motor was fabricated using precision machining techniques that were available, and did not involve micromachining techniques that are currently used [6]. (b) The first page of *A Tale of Two Cities* written using *e*-beam lithography by Tom Newman in 1985. The page shown has a dimension of  $5.9\mu\text{m} \times 5.9\mu\text{m}$  [7].

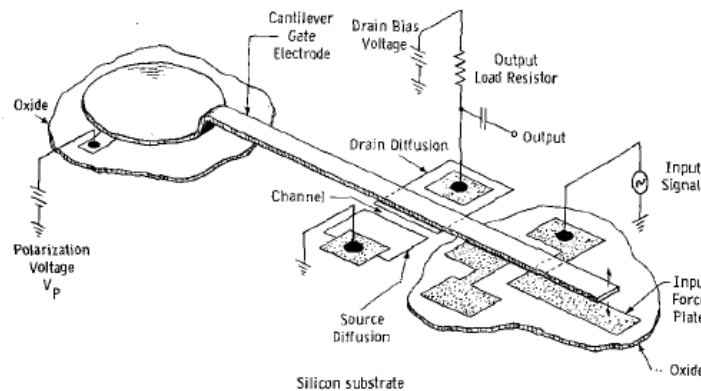


Figure 1.3. The first patented MEMS device, the resonant gate transistor device. The device is a cantilever actuated electrostatically that allows a current to pass through at its resonant frequency, thus acting as a frequency filter [8].

The MEMS devices developed rapidly and moved from being a research object to commercial products between the 1970's and the 1990's. Examples of such products are shown in Figure 1.4. The first commercially successful MEMS device was the silicon pressure sensor, invented in 1970 (IBM) [9]. This was followed by the introduction of thermal inkjet technology in 1979 (HP) [10], atomic force microscopy in 1986 (IBM) [11], and accelerometer ADXL50 for automotive airbags in 1993 (Analog Devices) [12]. The MEMS devices also emerged as one of the competing display technologies with the introduction of digital light processing (DLP) technology by Texas Instruments in 1993 [13]. The rise of consumer electronic devices such as digital cameras, smartphones, gaming consoles, tablets, and fitness trackers in the 2000's created a huge demand for MEMS accelerometers. As a result, in 2014, the commercial MEMS market has a total value of around \$ 11.1 billion, with the largest market share taken by accelerometers (28%), followed by inkjet printers (17%), RF MEMS (16%) and microphones (11%) [14]. It is projected that the MEMS market value will grow to more than \$ 20 billion in 2020, with the majority of growth arising from accelerometers and pressure sensors.

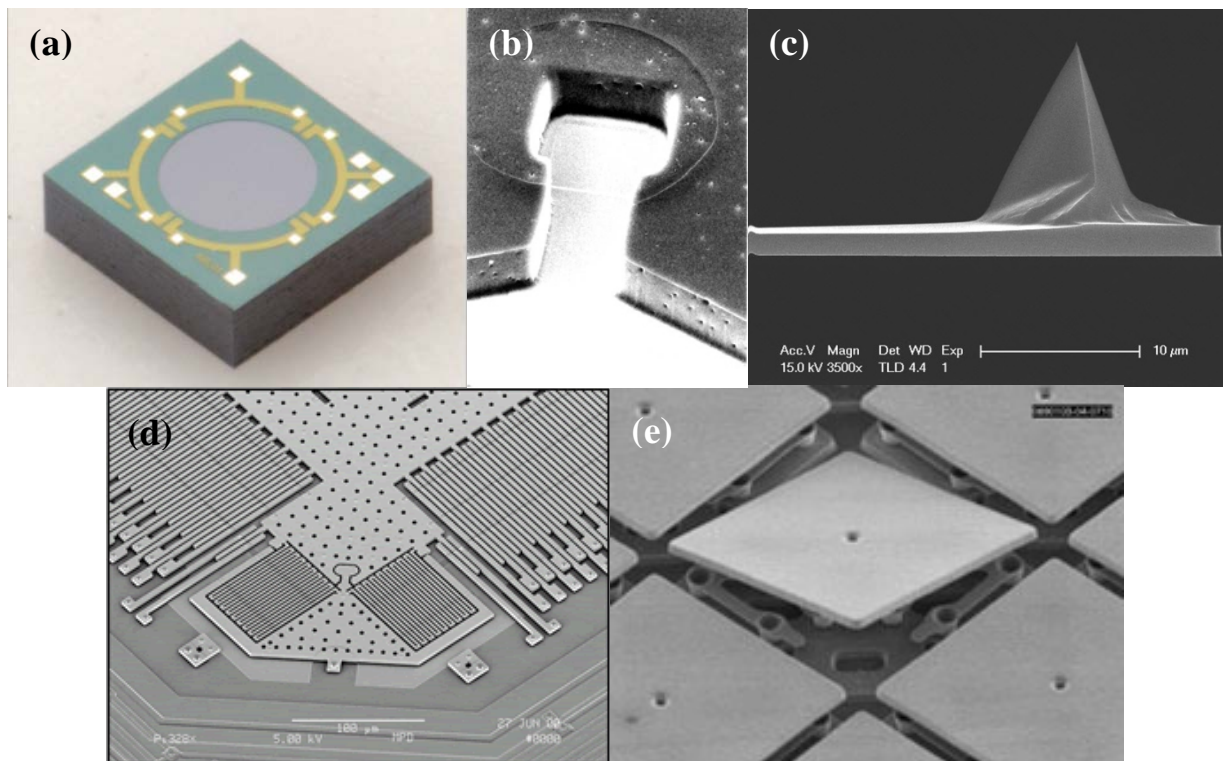


Figure 1.4. Examples of commercially important MEMS devices and structures: (a) piezoresistive pressure sensor (2s MPP-03 by OMRON) [15], (b) SEM image of a thermal inkjet head [16], (c) SEM image of an atomic force microscope tip (RESPA – 10 by Bruker) [17], (d) SEM image of a MEMS accelerometer with comb capacitor sensing (ADXL 202 by Analog Devices) [18], (e) SEM image of a tilting micromirror used for projection display technologies (DLP by Texas Instruments) [13].

## 1.2 Common MEMS structures

While MEMS devices might utilize different actuation and sensing mechanisms depending on the applications, the majority of them share the same basic mechanical structures. Based on the position of the support or clamp relative to the moving parts, the mechanical structures of MEMS devices can be classified into cantilevers, bridges, trampolines, suspended plates, and wine glass structures.

A cantilever is a beam that is supported or clamped from one of its ends. As stated before, the cantilever is historically the oldest of all MEMS structures, being used for the first patent granted to a MEMS device. The simplicity of the structure lends itself to easier fabrication and making it the best understood among other three structures described later on in this section. For these reasons, it has found itself in various applications, including atomic force microscopy (AFM) tips [11], memory devices [19], RF switches [20, 21], and biomedical sensors [22] (Figure 1.5). A detailed review has been written regarding applications of cantilevers [23], and readers are encouraged to peruse it for further study.

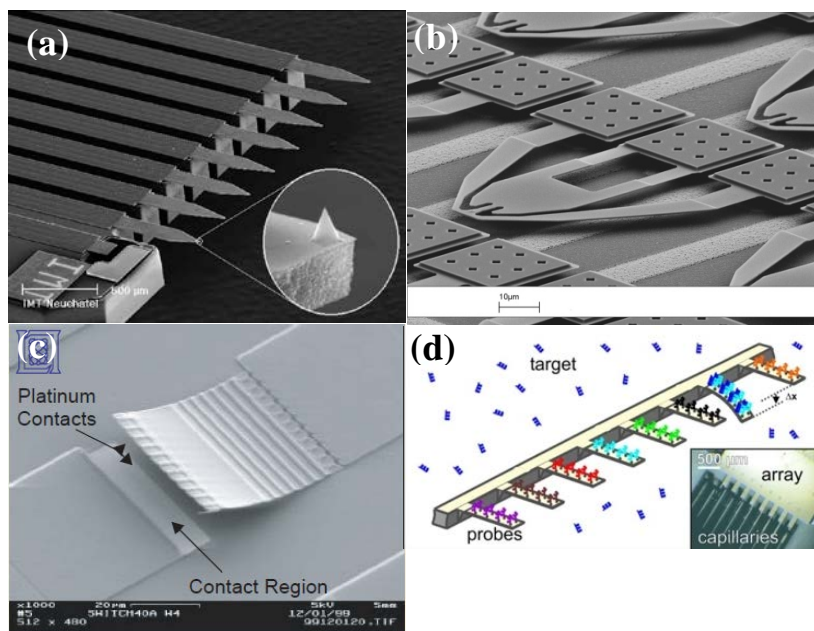


Figure 1.5. Examples of applications for cantilever structures: (a) atomic force microscope array for space applications [24], (b) millipede MEMS memory device [19], (c) cantilever RF switch [20], (d) cantilever functionalized with probes for mass detection [22].

A bridge is a beam that is supported or clamped on both of its ends. Due to this clamping scheme, the structure is more rigid compared to a cantilever of similar size, which also result in higher resonant frequency if used as a mechanical resonator. On the other hand, the double clamping scheme also means that unlike cantilevers, compressive stress might accumulate inside the structure, causing it to fail by buckling. This structure found a commercially significant application in DLP devices by Texas Instruments [13] (Figure 1.6.a). The DLP consists of a micromirror mounted on top of a bridge structure, which acts as a torsion spring. The micromirror can be tilted using electrostatic actuation to reflect a light to a specific direction, thus turning a pixel on and off. Compared to the competing liquid-crystal on silicon technology (LCOS), the DLP technology offers better color contrast and power efficiency since the light do not have to pass through the LCD before reaching the screen. However, the DLP technology has limitations in terms of resolution, since the size of the micromirror is larger than the current LCD pixel. Other applications include RF switches (Figure 1.6.b) [20] and gas sensors [25] (Figure 1.6.c), where the relatively high stiffness of bridge structures compared to cantilevers provide advantage in terms of response time and resonant frequency.

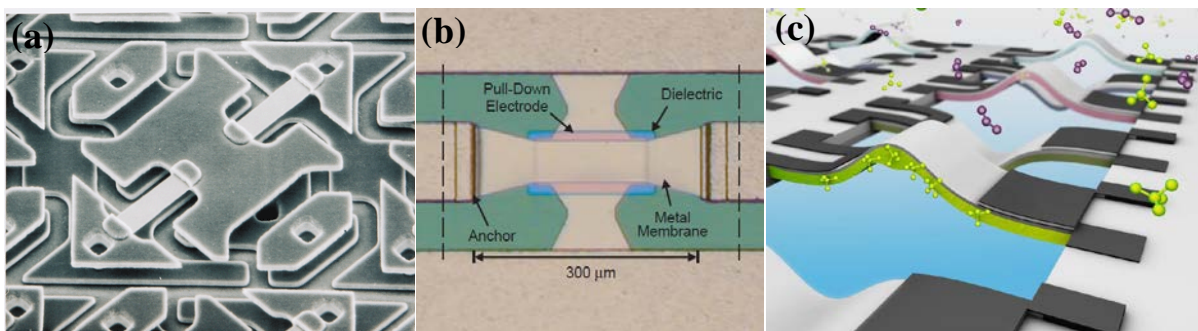


Figure 1.6. Some examples of applications for bridge structures: (a) Digital micromirror device [13], (b) RF MEMS switch [20], and (c) Gas sensor (IMEC / Holst Center) [26].

A trampoline structure is, in general, a plate that is supported or clamped on more than two sides. Unlike the previous two structures, it is not uncommon to use meander or rosette structures between the plate and the solid substrate support. One of the main applications of this type of structure is in MEMS accelerometers, as shown in Figure 1.7.a [27]. In this example, the main plate acts as a proof mass, which is supported by meander beams on four sides. Detection of the structure displacements is carried out using capacitive methods, which is enhanced by the comb structure between the proof mass and the static structure. The meander beams acts as a spring, which effective spring constant is determined by the beam width, the beam thickness, and the loops. This arrangement enables relatively large displacement of the proof mass and higher acceleration measurement span compared to what is possible using a straight beam support. Other possible applications of this structure are mechanical resonators (Figure 1.7.b) and micro-hotplate gas sensors (Figure 1.7.c).

A suspended plate structure is a plate that is supported or clamped along its entire circumference. The suspended plate is also referred to as a membrane or diaphragm, although the two structures can be differentiated based on the ratio between the displacement and its lateral size [30]. Due to its enclosed cavity, this kind of structure is suitable for applications where isolation of fluid from the cavity is desirable, such as for pressure sensors or liquid mass sensor. Since it is the main focus of this study, we will discuss in details the applications and the fabrication methods used to obtain suspended plate structures in the following subchapters.

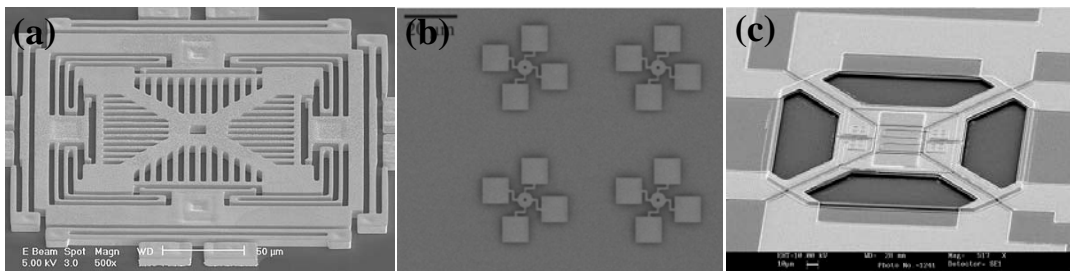


Figure 1.7. Some examples of applications for trampoline structures: (a) triaxial capacitive accelerometer [27], (b) trampoline structure for mass sensing purposes [28], and (c) micro-hotplate for gas sensing purpose [29].

Unlike the structures described previously, which are clamped or supported from their edge, a wine glass structure is a plate that is supported in its center by a stem, similarly to a mushroom or a wine glass (Figure 1.8.a) [31]. The wine glass structures mainly find applications as mechanical resonators with high mechanical quality factors ( $Q$ ) in vacuum conditions ( $Q \geq 10^6$  [31,32]). These high performances are possible because of the unique mode shapes exhibited by wine glass resonators (Figure 1.8.b), which minimize displacements of the resonators around the clamped axis, and thus minimize clamping losses of the devices.

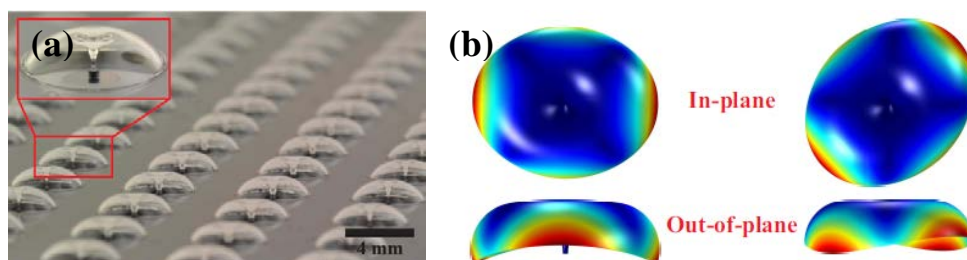


Figure 1.8. (a) An array of inverted wine-glass resonators fabricated using the glass-blow technique and using capacitive transduction. [31], (b) 1<sup>st</sup> and 2<sup>nd</sup>  $n=2$  vibration mode for the inverted wine glass resonator. It can be observed that minimum displacement is observed near the stem, which minimizes clamping loss [31].

### **1.3 Applications of Suspended plates**

In this subchapter, we discuss in more details the various applications of suspended plate structures. The first one concerns mass sensing, which is the original purpose of this work. The second application is for pressure sensing, which is historically the first commercially successful application of MEMS devices. Then, we discuss applications related to acoustic actuators and sensors, where suspended device MEMS are competing with more established and mature technologies. Finally, we present applications of suspended plate structures in the relatively young field of microfluidics.

#### **1.3.1 Mass sensors**

The general principle of a MEMS mass sensor is as follows. The MEMS device is exposed to the environment where an analyte or some material to be detected is present. Interactions of this analyte/material, that adheres to the device or passes through it, cause some changes on the device's mechanical properties. These changes are then measured and quantified to determine the amount of analyte/material in the environment. Aside from differences in geometries and materials used for the mass sensor itself, there are also notable differences between mass sensors regarding the use or not of a dedicated interface to specifically capture an analyte, as for biodetection applications, as well as the approach for measuring the mechanical perturbations caused by the presence of the compound.

In some cases, there is no need to functionalize the surface of the MEMS device, i.e. no need of any surface coating for specific recognition, to measure the presence of the compound. An example of this case is the application of quartz crystal microbalance (QCB) [33] to measure the thickness of thin film deposited by chemical or physical means. Since thin film deposition occurs in vacuum, only the vapor of the thin film or its precursors contributes to the change of the QCB's effective mass, enabling accurate determination of thin film thickness and deposition rate. However, in more general cases, the analyte coexist with other substances that share the same physical phase (i.e. liquid or gas) or chemical composition. In addition, it is not uncommon that the analyte concentration is so low that it is undetectable for MEMS device without any surface treatment. A surface coating that captures specifically the analyte is commonly applied to the device to solve the abovementioned problems. This surface coating might range from ZnO layer for methane [34], Au layer for molecules with thiol groups [35] to antibodies for proteins or cells detection [36]. As a result, a single type of MEMS structure can be used for detecting various kinds of analytes simply by changing its surface coating or functionalization. On the other hand, this also means that the sensitivity of a MEMS mass sensor strongly depends both on its mechanical properties and on the adhesion and the properties of its surface coating.

Static deflections of a structure or change in resonant frequency are the most commonly used means to quantify changes in mechanical properties of a MEMS mass sensor. Figure 1.9.a shows an example of a suspended plate mass sensor that undergoes static deflections [37]. The suspended plate is fabricated out of silicon and coated with antibodies specific to the targeted analyte in solution. As the analyte molecules bind to the surface of the plate, it introduces some surface stress within the plate and causes it to buckle. The amount of buckling is determined by shining a laser through the plate onto a photodiode placed underneath the plate, creating a current that can be amplified and measured. Since the gap between the plate and the photodiode forms a Fabry-Perot interferometer, the displacement of the sensing plate functionalized with antibodies can be deduced by comparison between its photodiode current with the one of a control plate, that is not functionalized, does not capture any analyte, and thus does not deflect. One can then deduce the amount of analyte in solution from the displacement of the plate functionalized with antibodies.

An example of a resonator mass sensor implemented with a suspended plate structure is shown in Figure 1.9.b [38]. In this example, a suspended plate structure fabricated out of silicon nitride includes a graphene layer on its surface. The analyte molecules that adhere onto the graphene layer cause an increase in the plate effective mass that result in a decrease of its resonant frequency. The example given here is unique since the analyte detection can be achieved by measuring the change in resonant frequency, but also by characterizing the plasmonic resonance and the graphene's electronic properties.

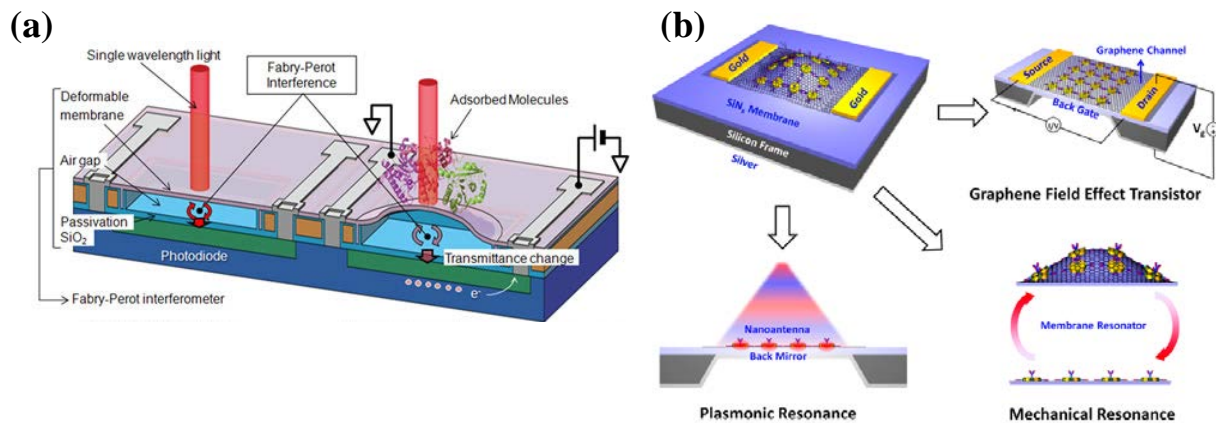


*Figure 1.9. Mass sensors relying on suspended structures with different detection principles: (a) the plate is deflected statically due to surface stress of adhering analyte, which is detected by optical interferometric principles. [37], (b) the plate's effective mass increases due to the additional mass of adhering analyte, which is detected by monitoring the resonant frequency of the plate [38]. In this example, the detection can also be done by plasmonic resonance and I-V measurement.*

Suspended plates have several advantages when used as mechanical resonator mass sensors compared to cantilever and bridge structures, the first one is in terms of sensor performance. For the same mass (*i.e.* same area for devices of the same thickness), the suspended plates have a higher resonant frequency compared to cantilever and bridge structures [30]. This higher resonant frequency results in lower molecular damping of the device in atmospheric pressure, a typical environment for practical MEMS sensors [39]. Both of these facts contribute to the increased sensitivity of the suspended plate mass sensor in air. The second advantage of suspended structures lies in the possibility to fabricate devices that are suitable for operation in liquid environment. One of the approaches to create a MEMS device compatible with liquid operation is to encapsulate the structure in a waterproof, insulating layer that protects the actuating and sensing elements from short circuit. While this approach seemed to be straightforward, depositing an insulating layer conformably all around a cantilever or bridge structure is not simple. The fabrication process of an electrostatically actuated cantilever that operates in liquid is presented in Figure 1.10.a [40]. In this example, the encapsulated layer and the cantilever are fabricated by multiple deposition processes to ensure complete coverage of the side walls and the bottom surface of cantilever. In addition to the complicated process steps, the open gap below the cantilever is filled with liquid during operation that impedes its movement. The liquid between the top and bottom electrode also degrades the electrostatic actuation ability of the device due to higher permittivity of the liquid compared to air. In contrast, encapsulation of a suspended plate structure is simpler and does not suffer from the same limitations (Figure 1.10.b) [41]. Assuming a tight (hermetic) seal between the plate and its support structure, only a single conformal deposition process of encapsulation layer is necessary to liquid-proof the device. The gap between the plate and the bottom of the substrate is either in vacuum or filled with air, having less mechanical damping and requiring less voltage to actuate compared to a gap filled with liquid. Thus, suspended plate structures have advantages compared to the cantilever or the bridge structure when it comes to liquid-proof encapsulation.

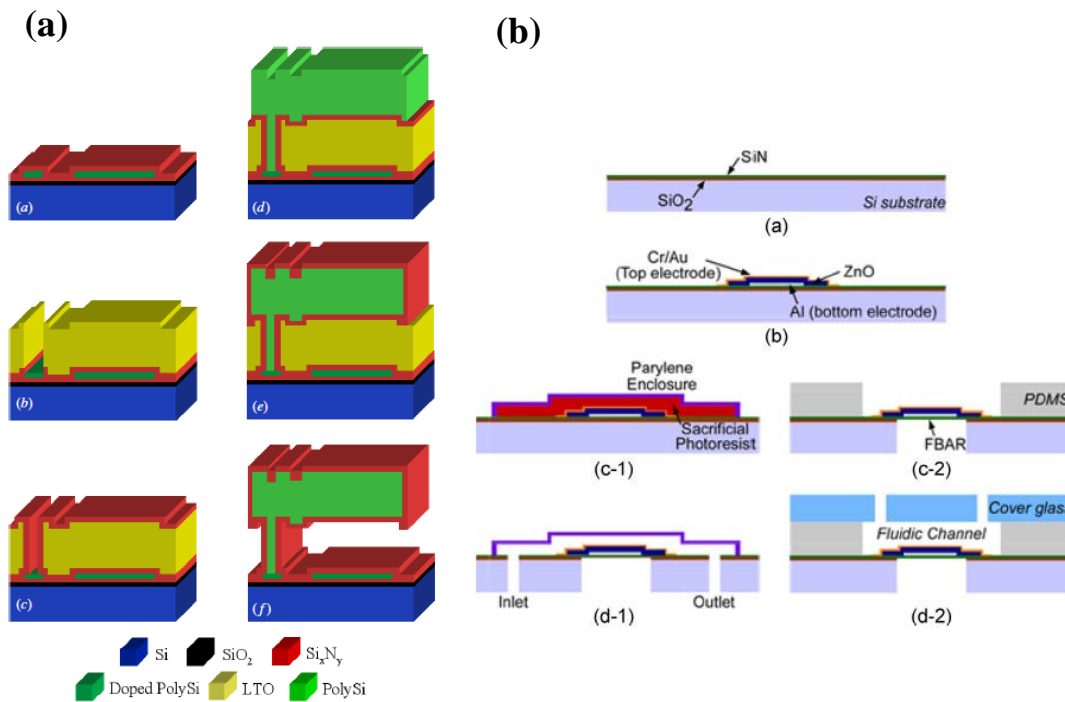


Figure 1.10. Comparison of fabrication process for two different structures used as mass sensors in liquid. (a) Cantilever operating with electrostatic actuation, with silicon nitride as the encapsulation layer. Multiple steps are required to ensure complete encapsulation of the cantilever on its sides and bottom surface, along with the electrode [40]. (b) Suspended plate operating with electrostatic actuation, with parylene as the encapsulation layer [41]. Note the complicated process required to encapsulate the cantilever, due to the necessity to encapsulate the backside and bottom electrode.

### 1.3.2 Pressure sensor

Suspended plate structures are ideal to create MEMS pressure sensors due to their inherent ability to create an enclosed, hermetic cavity. Besides the straightforward application for pressure measurement, it is also common to use the air pressure as a proxy for measuring altitude, such as for navigation inside buildings. Based on their operating principles, MEMS pressure sensors can be divided into two categories, static and dynamic.

In a static pressure sensor, the suspended plate is exposed to two different pressures on both sides of its surface, the reference pressure and the external pressure. The reference pressure is typically constant (atmospheric pressure or vacuum, depending on the application), and is defined by the air pressure inside the sealed cavity. The external pressure is variable, and is

defined by the air pressure of the environment surrounding the sensor. The pressure differential induces stress and strain on the plate, which can be detected through various transduction schemes. Historically speaking, the first static pressure sensor used a piezoresistive element fabricated on one side of the plate (Figure 1.11.a) [42]. The pressure differential causes strain on the suspended plate and the piezoresistive element, thus resulting in a change in electrical resistance that can be directly measured. Another transduction scheme relies on the use of a piezoelectric material. In that case, the strain induced on the plate results in a potential difference across the piezoelectric element and pressure is deducted by a voltage measurement. Capacitive transduction method is also commonly encountered in static pressure sensors, as shown in Figure 1.11.b [42]. In capacitive measurement scheme, the pressure differential causes the plate to buckle, changing the gap size between the plate and the substrate. This change of gap size is then evaluated by measuring the capacitance of the cavity. The capacitance of a suspended plate with a certain plate area depends on its gap size, which can be observed from the equation for parallel plate capacitors. For a device with a flat plate as described above, the gap size is a nonlinear function of pressure and position on the plate, with the exception in the case of small deflections. Since nonlinearity complicates and introduces errors to the measurement, several alternative device designs are available to increase linearity of pressure vs. capacitance.

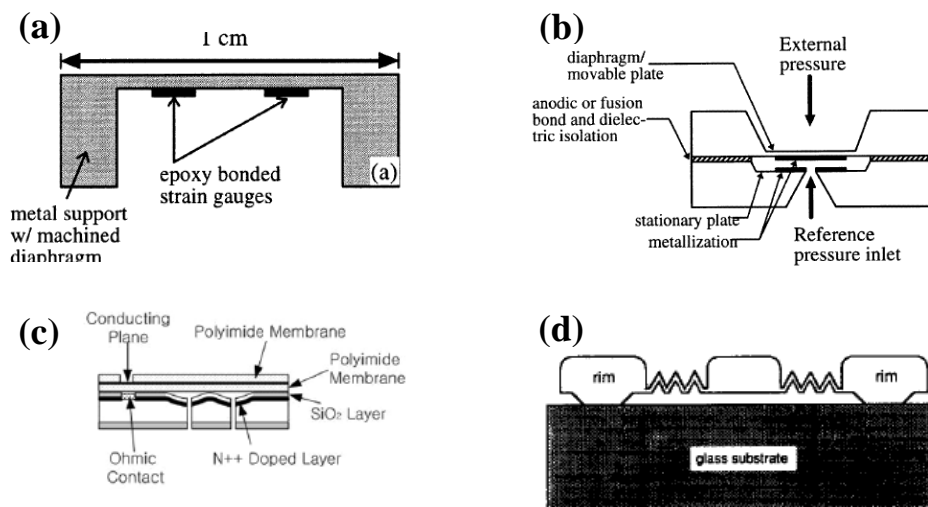


Figure 1.11. Examples of pressure sensors made using suspended plate structures. (a) Pressure sensor with strain gauges to detect deflection of the plate, fabricated using bulk micromachining technique [42]. (b) Pressure sensor with conventional capacitive sensing [42]. (c) Pressure sensor with touch-mode capacitive sensing [43]. (d) Pressure sensor with variable cross section [44].

One alternative design is a contact-mode capacitive pressure sensor, as shown in Figure 1.11.c [43]. This design relies on the variation of the effective capacitor area instead of the variation

of the cavity gap. In this mode, the geometry of the device is designed such that the top electrode plate comes into contact with the bottom part of the device, which consists of a metal coated with a dielectric. The pressure difference between two sides of the plate causes the contact area between the plate and the bottom electrode to change linearly, while the gap size is defined by the thickness of the dielectric and remains constant. Another alternative design that increases the linearity of the capacitive sensor is the usage of bossed plates, as shown in Figure 1.11.d [44]. This design still relies in the variation of the gap size with an attempt to make the gap size a function of pressure only while being independent of position on the plate. This is achieved by making a non-uniform plate cross-section, with thinner section on the extremities close to the anchor and thicker section on the center part. As a result, the strain caused by pressure difference mainly concentrates on the thinner edge of the plate, while the center part of the plate experiences very little change in shape and remains flat. As a result, the device behaves more closely to a parallel plate capacitor with a variable gap compared to the parabolic profile of a capacitive device with a uniform cross section.

Some works have also used optical detection schemes for measuring the deflection of suspended plates [45] (Figure 1.12.a,b). In this regard, this kind of devices is similar to the static mass sensor described in the previous subchapter [37], with the difference that the source of external plate stress comes from fluid pressure instead of accumulation of analyte on the sensor surface. The usage of interferometric techniques enables the detection of very small deflections down to sub-nm levels, making this detection scheme ideal to detect very small pressure differences. The separation between the plate and the optical sensing element enables the structure to be extremely miniaturized and to be positioned in small volumes inaccessible to other MEMS sensors, such as the interior of a cell.

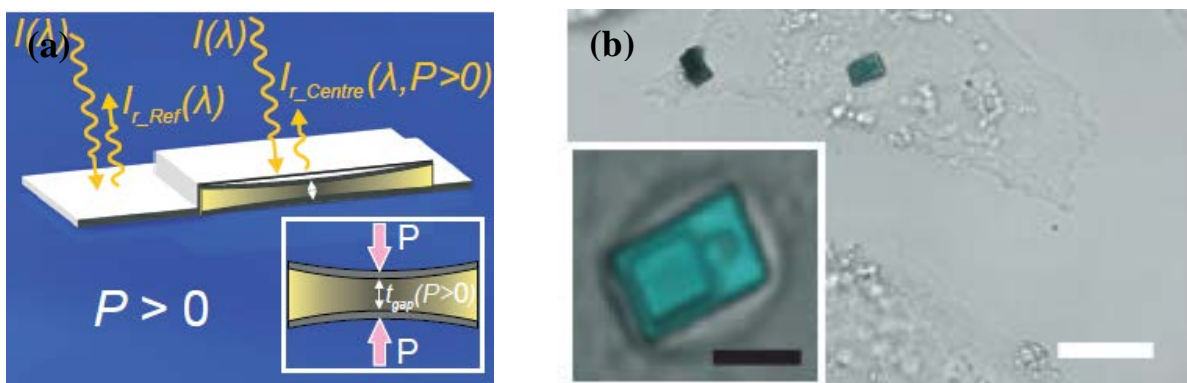


Figure 1.12. A suspended plate intracellular pressure sensor that operates using optical interference sensing. [45] (a) The working principle of the device. The pressure difference between the interior of the cell and the air inside the cavity deflects the plate, which creates detectable change in intensity. (b) Optical microscope image of the device inside a cell. The separation between the sensing mechanism and the plate enables pressure measurement in very small volumes.

Aside from the static pressure sensors described above, several works have been done to explore the possibility of using resonant devices as pressure sensors. These resonant sensors have advantages in terms of signal to noise ratio compared to their static counterparts. Several variations of these resonant sensors are available, each operating with different sensing principles. One type of resonant pressure sensor relies on the strain introduced by the pressure differential to change the resonant frequency of the device, as shown in Figure 1.13 [46]. This type of device shares the same basic design as the static capacitive device described earlier, with the additional requirements that the structures' resonant frequency lies within the measurement bandwidth and that the quality factor of the device within its operating range is high enough to ensure sufficient signal to noise ratio. Another type of resonant pressure sensor utilizes the variation of Q factor with squeeze film damping due to changing air pressure to measure the pressure [47]. Naturally, the squeeze film effect pressure sensor is open to its operating environment, which can be an advantage in terms of design (designs such as cantilevers and bridges are usable) and fabrication (no need to ensure airtight sealing) or limitations in terms of applications (might be unsuitable for corrosive or conductive fluids).

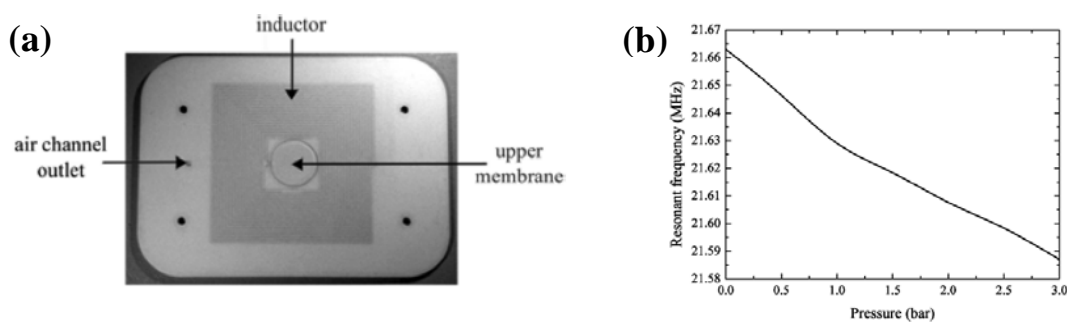


Figure 1.13. (a) Optical microscope image of a suspended plate pressure sensor with resonant frequency sensing method. (b) Plot of the sensor resonant frequency vs. pressure.

### 1.3.3 Acoustic sensors and actuators

Related to the application of micromachined suspended plates for pressure sensing, these structures can also be utilized to measure acoustic waves in different mediums such as in gas and in liquid. Since acoustic waves consist of periodic variation of pressure, they can in theory be measured using an air pressure sensor. However, the high frequency and small magnitude of typical acoustic waves require some modifications in the design of typical air pressure sensors. Figure 1.14.a shows an example of a MEMS capacitive microphone, also known as a condenser microphone [48, 49]. The difference between the microphone and the capacitive pressure sensor described previously is the usage of both a perforated bottom

electrode and a large, deep cavity below the suspended plate: the purpose of these design choices is mainly to reduce squeeze film damping on the suspended plate, which is inversely proportional to the size of the gap (see chapter 2). Reducing the damping increases the sensitivity of these devices and enables them to measure the sound wave with high stability and flat response. Analogous to the usage of capacitive microphone, the suspended plate structure can also be used to measure acoustic waves in liquid, which is known as a hydrophone [50]. In this application, the challenge is to ensure good acoustic impedance matching with the liquid medium. This is mainly ensured by filling the cavity between the plate and substrate with liquid instead of air or vacuum, which example is shown in Figure 1.14.b.

While the two above examples describe the usage of suspended plate structures for sensing, the same basic structures can also be used for actuation by applying a driving signal on the electrodes (electrostatic actuation). Acoustic waves can be generated in air by MEMS speakers, an example of which is shown in Figure 1.15.a [51]. In this example, the membrane is made out of silicon and electromagnetic actuation is used to drive the membrane. While not easy to fabricate, this actuation scheme offers the advantages of high power density, low actuation voltage, and linear response compared to its electrostatic counterparts. The suspended plate structures also found applications in capacitively machined ultrasonic transducers (CMUTs) [52 - 54], in which the structure both acts as the sensor and the generator of ultrasonic waves (Figure 1.15.b). Commonly fabricated in arrays, CMUTs mainly found applications in medical imaging as an alternative to the more established piezoelectric transducers.

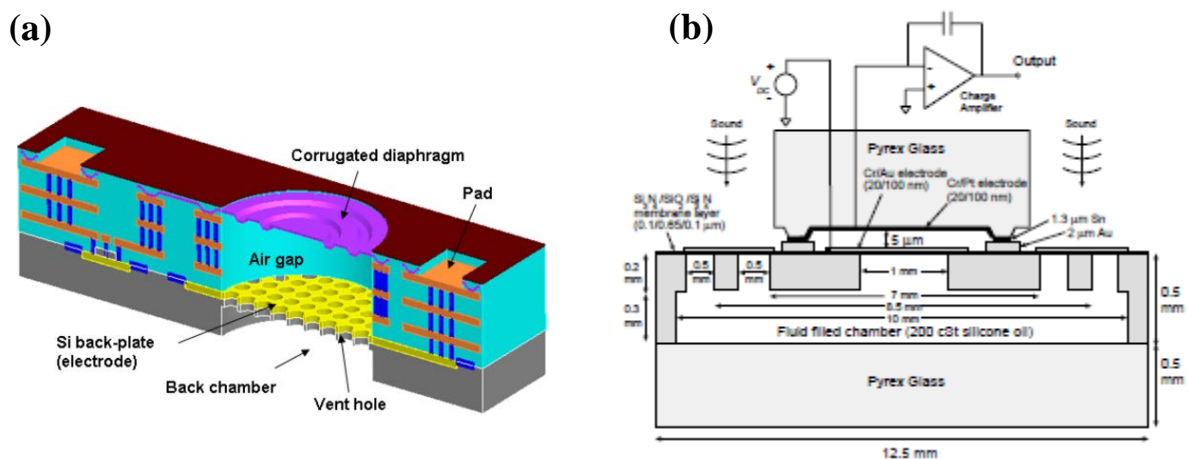


Figure 1.14. (a) A capacitive MEMS microphone. While it shares a similar structure with a typical pressure sensor, the back electrode is perforated to reduce squeeze film damping effect [48]. (b) Capacitive MEMS hydrophone. The cavity between the plate and the glass substrate is filled with liquid for impedance matching with the liquid acoustic medium [50].

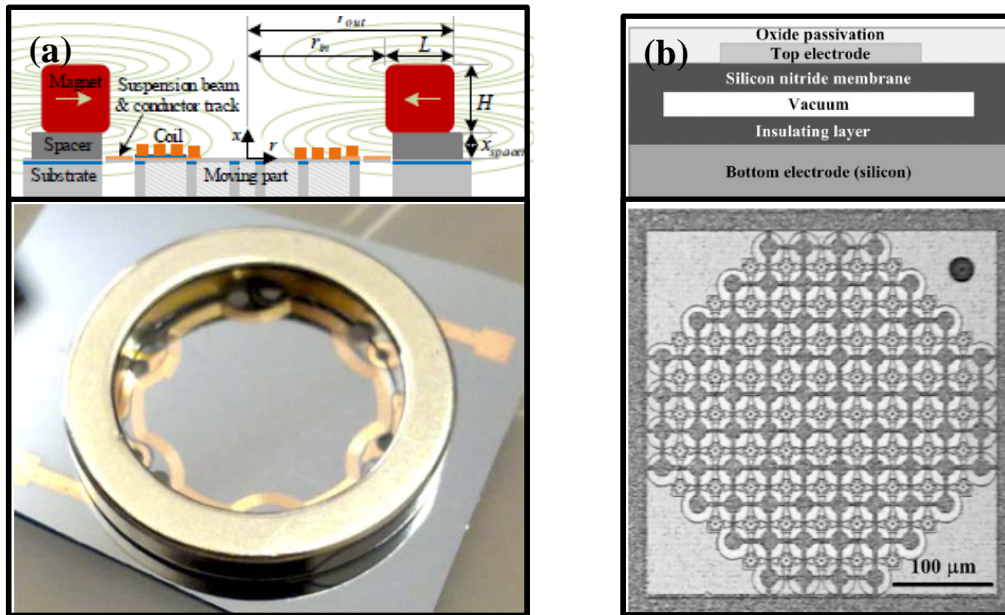


Figure 1.15. (a) Cross-section and photo of a MEMS speaker device. The speaker plate is fabricated out of silicon with magnetic coils for its actuation mechanism [51]. (b) Cross-section and optical microscope image of a capacitive micromachined ultrasonic transducers (CMUT) array. The device acts as both sensors and actuators, with applications in medical imaging systems [54].

### 1.3.4 Actuators in Microfluidics

Microfluidics is the manipulation of liquid at the micro and nanoscale, where typically the influence of surface tension dominates and the Reynolds number is small, resulting in laminar flows in microchannels. Started with applications in inkjet printing during the 1980's, microfluidics has found wider applications in medicine and biology such as electrophoresis, DNA arrays, lab on a chip, and mechanical characterization of cells. Suspended plates and membranes with enclosed cavity found applications in microfluidics as actuators such as pumps and valves.

A typical example of a microfluidic pump that uses a suspended membrane is shown in Figure 1.16. [55, 56]. In this example, the polymer membrane separates the two channels, each of which contains air and liquid. The pump is operated by sending pneumatic driving signals on the air side of the membrane in a pulse pattern; this causes the membrane to expand and contract, displacing the liquid along the channel. Three of such membranes are connected in series to enable flow control in one chosen direction of the channel. Pumps that use this kind of liquid displacement mechanism, which is analogous to the way liquids and solids are moved in biological digestion systems, are known as peristaltic pumps. Actuation systems

other than pneumatics can also be used in the same pumping scheme, such as piezoelectric peristaltic pumps.

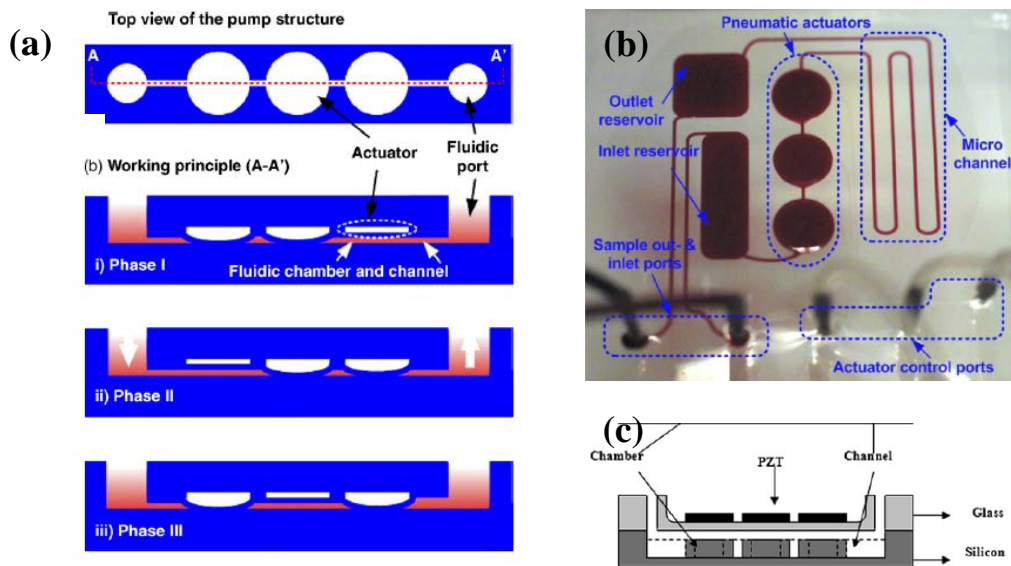


Figure 1.16. (a) Top view and working principle of a peristaltic micropump based on pneumatic actuation. The 3 actuators are inflated and deflated in series repeatedly, causing displacement of the liquid from one side to the other [55]. (b) Photograph of the pneumatic peristaltic pump, along with microfluidic network in the chip [55]. (c) Cross-section schematic of a peristaltic pump with piezoelectric actuators [56].

Another application of suspended plates in microfluidics is their use as valves, an example of which is shown in Figure 1.17 [57]. In this example, the plate is positioned perpendicularly to an opening in a liquid channel. By application of appropriate pneumatic signal (air pressure), the plate will deflect and flatten to close and open the channel, controlling the liquid flow. Compared to conventional bulk components, such pumps and valves have a fast response time, and can be easily integrated within microfluidic systems.

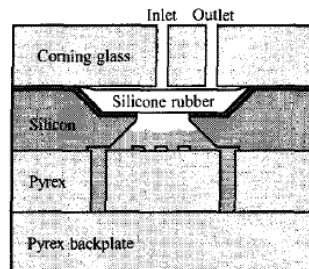


Figure 1.17 cross sectional view of a suspended plate microfluidic valve. This valve is controlled by pneumatic signal on the topside of the device, which can close the valve when air pressure is applied [57].

## 1.4 Common fabrication methods of suspended plates

In this subchapter, we present and discuss the fabrication processes commonly used to make suspended plate structures. These include bulk micromachining techniques, surface micromachining techniques, and wafer bonding techniques.

### 1.4.1 Bulk micromachining

In bulk micromachining, the silicon wafer itself is viewed as the main material from which the MEMS components are made. This fabrication approach differs from surface micromachining, where all components are fabricated by deposition and etching on top of the silicon wafer, which is merely viewed as a “substrate”. Bulk micromachining was widely used in fabrication of silicon pressure sensors, which are the first commercially successful MEMS devices.

One way to fabricate suspended plate using bulk micromachining technique is the back-etch technique, which is illustrated in Figure 1.18 [58]. In this approach, the backside etching is achieved by silicon wet etching in a KOH bath using a heavily doped layer as an etch stop. First, the surface of the wafer is doped using boron (P-type impurities), with a specific dose that depends on the desired thickness of the plate. Afterwards, the shape of the suspended plate is patterned using photolithography on the opposite surface of the wafer (*i.e.* its backside). The wafer is then etched anisotropically using KOH solution, which etches silicon until it reaches the doped layer where the etch rate is significantly lower. The photoresist is then stripped away, and the desired suspended plate is obtained. Several variations of this technique exist, mainly differing in terms of etch stop and etching process itself. For example, a reactive ion etching (*i.e.* dry etch) process can be used to obtain a more accurate plate form because of the higher anisotropy of this etching process. Also, silicon-on insulator (SOI) wafers can be used to obtain suspended plates with very precise thickness (same as the top/device layer thickness). In that case, the buried silicon oxide layer is used as a stop layer and can be subsequently removed using an HF solution.

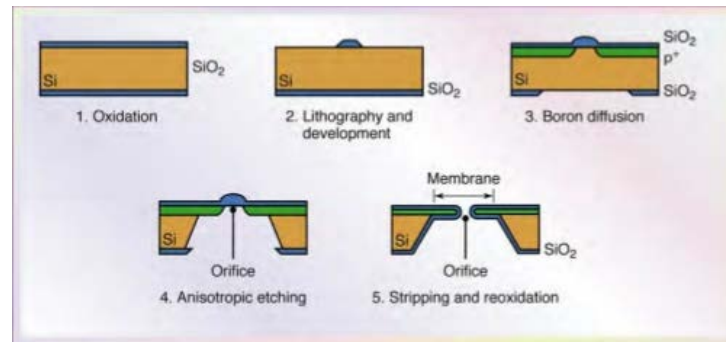


Figure 1.18. Illustration of a bulk micromachining process used to create a suspended structure, in this case a membrane with an orifice. Boron is diffused in the silicon substrate to act as an etch stop layer. The wafer is then anisotropically etched from the backside until it reaches the heavily doped silicon layer to form the suspended membrane. Afterwards, the silicon layer is reoxidized to create a passivation layer [58].

Related to the approach shown above is the front etch technique, which is illustrated in Figure 1.19.a for the fabrication of a trampoline structure [59]. In this approach, the top layer of an SOI wafer is first patterned using photolithography. RIE techniques are then used to etch the general shape of the device, which contains large gaps between the beams that reach the anchor of the structure. The wafer is then immersed in an HF solution that etches away the buried oxide layer isotropically through the gaps between the beams. By careful timing the wet etch duration, it is possible to obtain a complete etch of the oxide underneath the defined plate area (without fully etching the oxide underneath the anchors) and obtain a high-quality suspended plate/membrane with small gap size defined by the thickness of the buried oxide layer. In the case of suspended plates with large areas (Figure 1.19.b), small via holes can be defined during the photolithography step to increase the HF flow below the plate and reduce the chance of incomplete release.

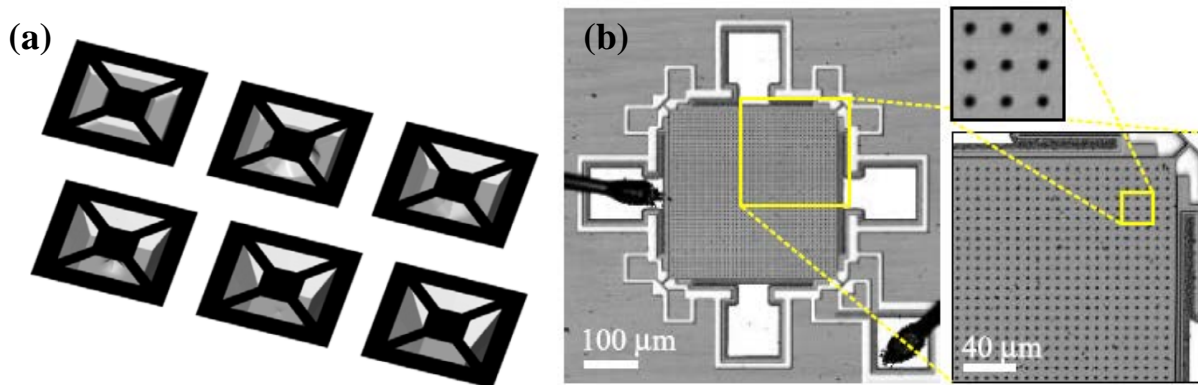


Figure 1.19. (a) Simulation of a trampoline structure fabrication based on isotropic front side etching. After patterning using lithography and reactive ion etching, the structure is released by wet etching the buried oxide layer in HF [59]. (b) An example of via holes patterned on top of device with large surface area. These via holes increase the contact area between the HF solution and the silicon oxide layer underneath the device, thus aiding the release of the suspended structure [60].

The advantage of the bulk micromachining techniques is the use of high quality material constituting the plate in terms of defects and stress. This is due to the single crystal nature of the material, which is typically a silicon wafer fabricated for CMOS specifications. The same cannot be said for surface micromachining techniques, which has to deal with crystal growth mechanisms and the internal stress between the different deposited materials. The limitation of this technique is the additional post-processing step necessary to fabricate a complete device with actuation and sensing elements, such as bonding to another substrate and wafer thinning if small gap is desired (*i.e.* such as in capacitive devices). In addition, the devices fabricated using this bulk micromachining techniques have a tendency to be bulkier than those made using surface micromachining, and the process is not always suitable for chip-level integration of MEMS + CMOS systems.

### 1.4.2 Surface micromachining techniques

In the surface micromachining approach, suspended plate structures are fabricated by the alternating deposition, patterning and etching of various materials on the surface of a substrate wafer. The key behind this technology is the usage of a sacrificial layer that is used to support the primary structural material onto which it is deposited. After depositing and patterning the structural material, the sacrificial material is selectively etched away in order to release the suspended plate structure. Figure 1.20 shows an example of a process flow used to fabricate a CMUT device, which includes eight steps [53]. First, a sacrificial layer (silicon oxide) is

deposited and patterned according to the shape of the suspended plate and its support pillars. Next, the structural material of the suspended structure (in this case, silicon) is deposited over the entire substrate. Via holes are then etched through the silicon until the underneath oxide layer is reached. The suspended structure is then released by wet etch using HF. Finally, the device undergoes metallization to form the electrical interconnects. Note that in this case, the suspended structure and the sacrificial layer are created from a material deposited on the substrate and not from the substrate itself, hence the name surface micromachining.

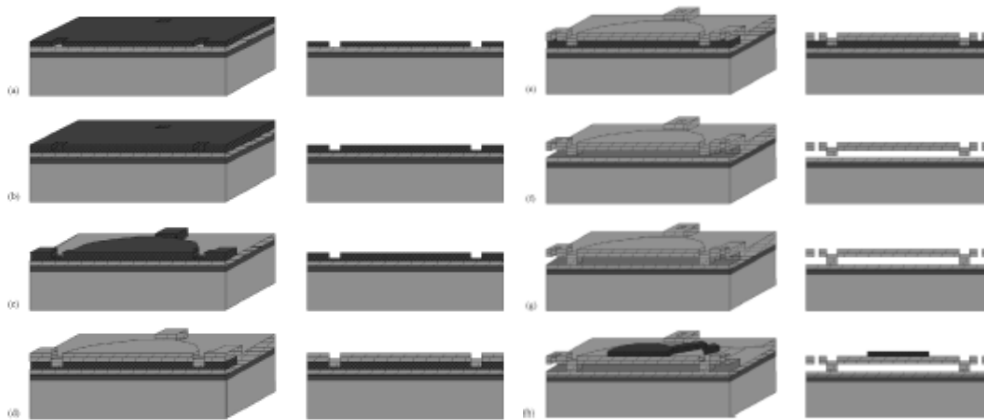


*Figure 1.20. Illustration of a surface micromachining process used to create a suspended structure, in this case a CMUT device. Sacrificial layer (silicon dioxide) is deposited and patterned on the substrate, followed by the deposition of the structural material (silicon). The sacrificial layer is then etched away using HF solution through the via holes, leaving a suspended plate structure. Note that the resulting suspended structure is not created using elements from the substrate itself [53].*

The advantage of this method is its compatibility with standard CMOS processing techniques, thus making it more suitable for integration on a chip level without additional packaging steps. This makes it ideal for lab on chip applications that requires small device footprint. The limitation of this method is the lower quality of the material used to create the suspended plate, in terms of mechanical and electrical properties, relative to single - crystal material commonly used in bulk micromachining techniques.

### 1.4.3 Wafer bonding technique

A more flexible fabrication technique is the wafer bonding technique, which is illustrated in Figure 1.21 [53]. In this approach, two wafers are used. On the surface of the first wafer, the supporting structure is defined using thermal oxidation, photolithography, and RIE etching.

Afterwards, the second wafer, which is an SOI wafer, is anodically bonded to the first wafer, with the top SOI layer in contact with the supporting structure. The bulk and buried oxide layers of the SOI are then etched away, leaving away the top SOI layer as the plate layer.

The separation of the plate and the support element in this technique brings an inherent advantage over the previously described techniques. First, it enables to optimize separately the processes carry out on the plate and the supporting structure. These processes might have different requirements in terms of thermal budget, critical dimensions, etc.. This technique can be thought of as “macro-masonry” in analogy to the micro-masonry technique used in this study, which will be described further.

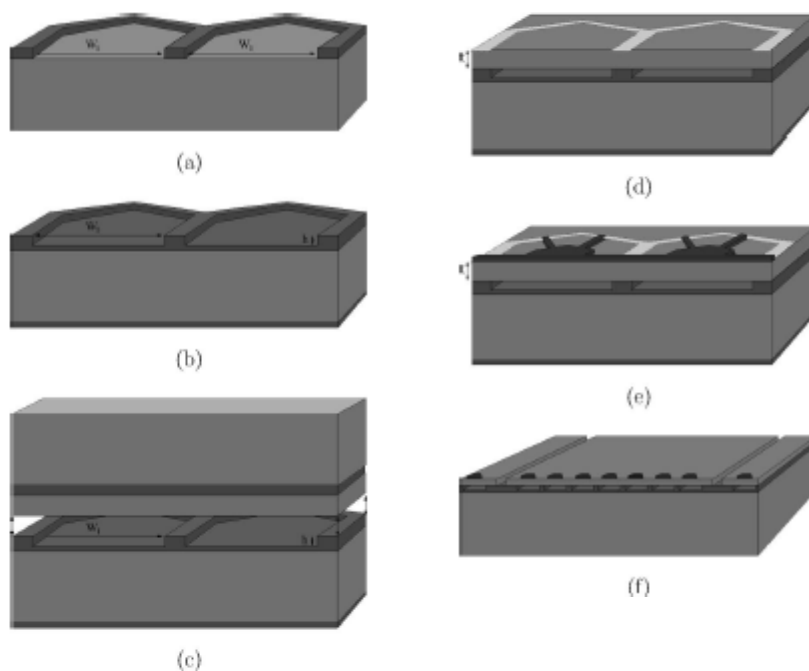


*Figure 1.21 Illustration of wafer bonding process to create a suspended structure, in this case a CMUT device. On the first wafer, a support layer is defined using photolithography and etching. A second wafer (a silicon on insulator, SOI wafer) is then bonded on top of the first wafer using anodic bonding process. The second wafer is then etched away leaving the device layer as the suspended plate [53].*

### 1.5 Micro masonry as a method to fabricate suspended structures

Transfer printing is a class of fabrication techniques that uses a polymeric stamp to transfer a material (referred to as the ink) from one substrate (donor substrate) to another substrate (acceptor substrate). In its most general terms, this include the well-known technique

microcontact printing, although the term “transfer printing” more commonly refers to techniques for which the ink is a solid material. Transfer printing has been used to transfer diverse materials such as metal lines [61]; photoresist patterns [62]; and semiconductor nanowires [63], offering a unique alternative solution for the fabrication of suspended plate structures. An excellent review article has been written regarding this subject [64], and the reader is encouraged to peruse it for detailed overview of this technique.

One of the main challenges of transfer printing is the control of adhesion between the ink, the stamp, the donor substrate, and the acceptor substrate. The transfer printing process can be divided into two steps: the pickup step where the ink is transferred from the donor substrate onto the stamp, and the drop step where the ink is transferred from the stamp onto the acceptor substrate. For the pickup step to be successful, the adhesion between the ink and the stamp must be larger than the one between the ink and the donor substrate. Conversely, for the drop step to be successful, the adhesion between the ink and the stamp must be smaller than the one between the ink and the acceptor substrate. For cases where one of the ink surfaces is in full contact with the ink, the donor substrate, and acceptor substrate, the adhesion is directly proportional to its surface energy. A problem is encountered if the amount of ink-stamp adhesion necessary for successful pickup step is larger than the ink-acceptor substrate adhesion necessary for successful drop step. This problem is obvious if the surface of both the acceptor and donor surface are of the same kind, for example between thermal silicon oxide and PECVD silicon oxide.

Micro-masonry is an advanced approach of transfer printing that provides a solution to this problem [65, 66]. The answer lies within in the stamp itself, which contains pyramid-shaped tips (Figure 1.22.a). During the pickup step, the pressure applied to the stamp deforms the tip and the ink comes into contact with both the tips and the entirety of the stamp surface. This ensures high adhesion between the stamp and the ink, enabling it to be picked up from the donor substrate. When the stamp is pulled away from the donor substrate together with the ink, the elasticity of the tips pushes the ink away from the stamp surface, resulting in the ink being held by the small area corresponding to the stamp tips. This ensures low adhesion between the stamp and the ink, enabling it to be deposited to the acceptor substrate. Thus, the adhesion strength of the stamp is a function of peeling rate, as plotted in Figure 1.22.b. The capability of this technique to create static structures, actuators, and comb-drive resonators has been shown on previous works [65-69].

In this work, we explore the possibility of using the transfer printing technique to fabricate silicon nanoplate resonating structures by studying the influence of this fabrication technique on the device performances.

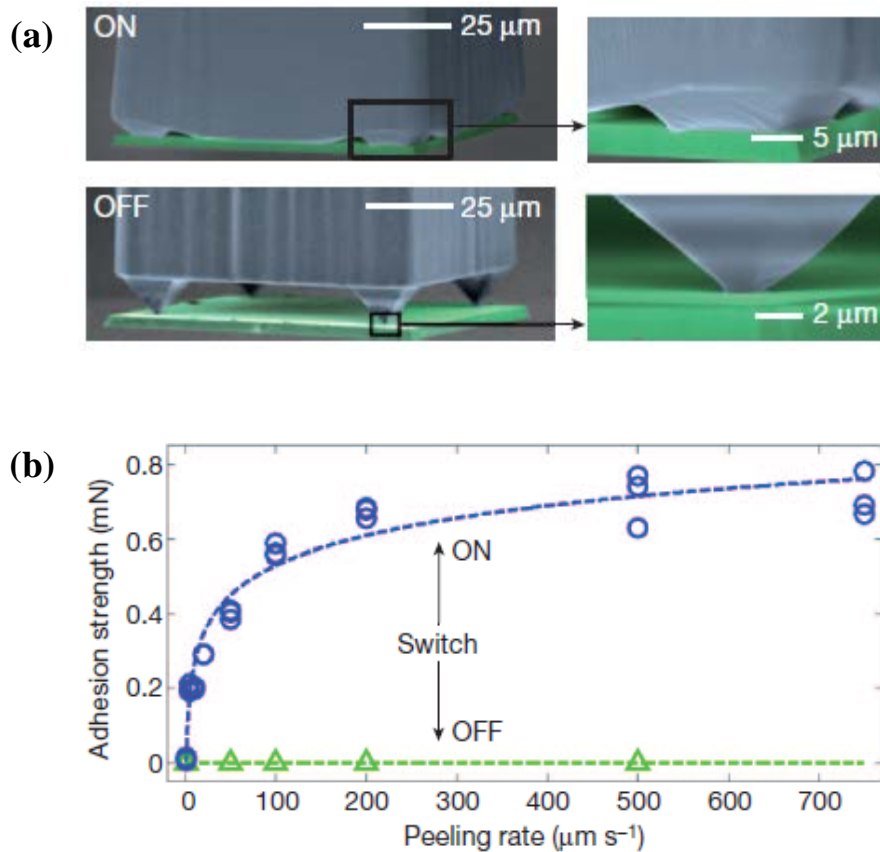


Figure 1.22. (a) SEM false color image of the microtip stamp used in micro-masonry technique, along with the silicon nanoplates used as an ink. When the stamp is pushed into the ink during the pickup step (ON), the ink comes into contact with the deformed pyramid tips and the center of the stamp, creating a large contact area and large adhesion. When the stamp is retracted (OFF), the elasticity of the pyramid tips pushes the ink away from the stamp, resulting in a small contact area at the pyramid tips and low adhesion [66]. (b) Measurement results of stamp adhesion force vs. peeling rate of the stamp [66].

## 1.6 Basic concept of the thesis project

The basic idea of the devices studied in this thesis project is illustrated in Figure 1.23. Structures with cavities (the “base structures”) are fabricated on a silicon substrate (the “acceptor”). Each base structure includes single or multiple cavities with varying shapes. Silicon nanoplates (the “ink”) are fabricated from another wafer, specifically from the top layer of a silicon on insulator (SOI) wafer (the “donor”). The micro-masonry technique is then used to transfer the ink on top of the base structures, creating a suspended structure. The acceptor wafer with the suspended structures is then annealed at high temperature to create a rigid bond between the base structures and the ink. The structures can then be used as a passive structure, or can undergo further processing to create devices with actuation and sensing elements. This approach should ideally enable creation of suspended structures out of

different material and thickness on a single substrate, thus making it more flexible compared to previously mentioned fabrication technique.

This work is carried out in collaboration with Professor Seok Kim from the University of Illinois at Urbana Champaign, USA, who is an expert in micro-masonry. As a result, the structures presented in this thesis were fabricated at LAAS, except for the micro-masonry step that was achieved in Professor Kim's lab.

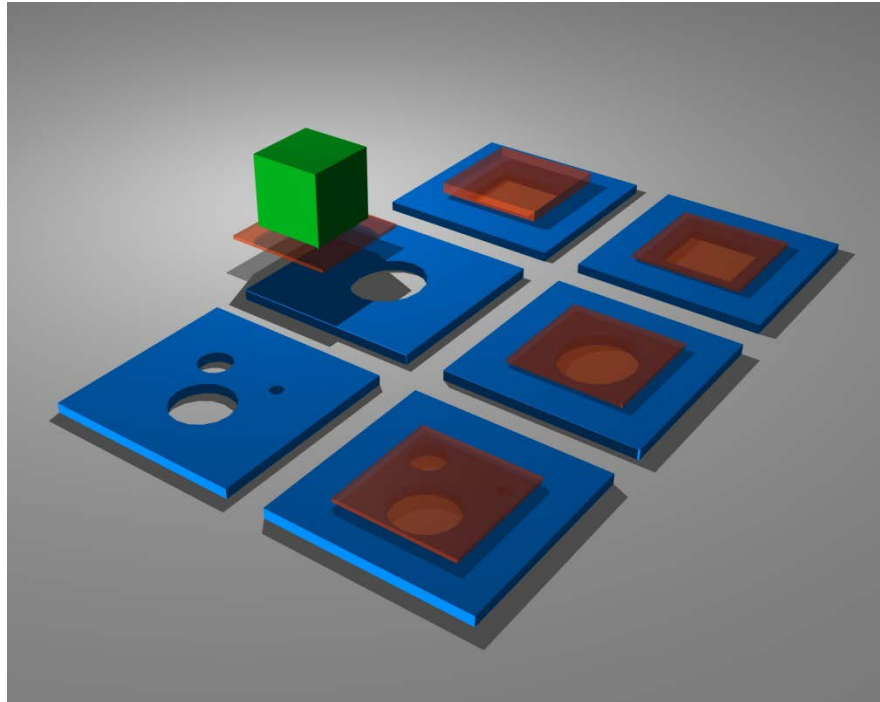


*Figure 1.23. Illustration of the application of micro-masonry for the fabrication of suspended plate devices. The base structures (blue) contain single or multiple cavities and is fabricated on top of the acceptor substrate. The silicon nanoplate ink has a square layout and is fabricated from the device layer of a silicon on insulator (SOI) donor substrate. The ink is transferred from the donor wafer to the base structures using microtip stamps, creating suspended structures. The combined structures are then thermally annealed to create a rigid bond between the ink and the suspended structures.*

More specifically, the objective of this work is as follows:

1. To fabricate passive suspended plate structures using micro-masonry as an alternative method of suspended plate fabrication and characterize the structure.

2. To fabricate a functional suspended plate device with integrated actuation and sensing using micro-masonry and characterize the device.
3. To demonstrate the successful operation of the active device in liquid environment.
4. 1.7 Organization of the thesis

This thesis is organized into five chapters. The second chapter, entitled “Theory, Design, and Fabrication Process” gives fundamental theories about mechanical resonators, provides descriptions of the design of the structures and devices realized in this study, and presents the fabrication processes employed to make them. The third chapter, entitled “Characterization and Measurement”, contains theoretical basis of measurement and the experimental setup used in this study. The fourth chapter, entitled “Results and Discussion”, contains the main results of this study for both passive structures and active devices. The fifth chapter, entitled “Conclusion”, summarizes the important findings of the study, along with perspectives regarding future work.

### **1.8 Summary**

MEMS are microscale structures that contain both mechanical and electrical elements, with applications such as accelerometers, gyroscopes, projection displays, and mass sensors. Structures that are commonly used in MEMS device include cantilever, bridge, trampoline, suspended plate, and wine glass structures with the current study focusing on the suspended plate structures. Examples of applications of suspended plate structures include mass sensors, pressure sensors, acoustic transducers, and microfluidic actuators. Fabrication methods that are commonly used to fabricate these structures include bulk micromachining, surface micromachining, and wafer bonding. Micro-masonry is a variant of the transfer printing technique that uses stamps with microtips to achieve controllable adhesion, and offers an alternative fabrication method for suspended plates. In this work, we propose to study the possibility to use micro-masonry for the fabrication of nanoplate resonators.

## References

- [1] Morris P R 1990 *A History of the World Semiconductor Industry* (IET)
- [2] Noyce R N 1961 Semiconductor device-and-lead structure US patent 2981877 A, April 25, 1961
- [3] Ti.com. 50th anniversary of the IC - Photos [Internet]. 2015 [cited 1 October 2015]. Available from: <http://www.ti.com/corp/docs/company/history/technologyforinnovators/photos.shtml> Ti.com
- [4] Fairchildsemi.com. History and Heritage | Fairchild [Internet]. 2015 [cited 1 October 2015]. Available from: <https://www.fairchildsemi.com/about/history-heritage/>
- [5] Feynman R P 1960 There's plenty of room at the bottom *Engineering and science* **23** 22–36
- [6] Staff 1960 The Month at Caltech *Engineering and Science* **24** 16–9
- [7] Dietrich J S 1986 Engineering and Science, Volume 49:3, January 1986 *Engineering and Science*
- [8] Nathanson H C, Newell W E, Wickstrom R A and Davis J J.R. 1967 The resonant gate transistor *IEEE Transactions on Electron Devices* **14** 117–33
- [9] Petersen K E 1978 Dynamic micromechanics on silicon: Techniques and devices *IEEE Transactions on Electron Devices* **25** 1241–50
- [10] Heinz J and CH Hertz 1985 Ink-jet Printing *Advances in Electronics and Electron Physics* 65 91.
- [11] Binnig G, Quate C F and Gerber C 1986 Atomic Force Microscope *Phys. Rev. Lett.* **56** 930–3
- [12] Schuster M 1996 Increasing the Frequency Response of the ADXL Series Accelerometers *Analog Devices Application Note AN-377*
- [13] Hornbeck L J 1993 Current status of the digital micromirror device (DMD) for projection television applications *Electron Devices Meeting, 1993 Technical Digest.*, 381–4
- [14] Mounier E, Troadec C, Guillaume G, Charentenay Y 2015 Status of The MEMS Industry 2015 *Yole Developpement report*
- [15] Omron.com. OMRON Global [Internet]. 2015 [cited 1 October 2015]. Available from: <https://www.omron.com/>
- [16] Wang Y and Bokor J 2007 Ultra-high-resolution monolithic thermal bubble inkjet print head *J. Micro/Nanolith. MEMS MOEMS* **6** 043009–043009 – 10
- [17] Brukerafmprobes.com. RESPA-10 - Bruker AFM Probes [Internet]. 2015 [cited 1 October 2015]. Available from: <http://www.brukerafmprobes.com/p-3935-respa-10.aspx>
- [18] Analog.com. Mixed-signal and digital signal processing ICs | Analog Devices [Internet]. 2015 [cited 1 October 2015]. Available from: <http://www.analog.com/en/index.html>
- [19] Vettiger P, Despont M, Drechsler U, Durig U, Haberle W, Lutwyche M I, Rothuizen H E, Stutz R, Widmer R and Binnig G K 2000 The Millipede; More than thousand tips for future AFM storage *IBM Journal of Research and Development* **44** 323–40

- [20] Rebeiz G M and Muldavin J B 2001 RF MEMS switches and switch circuits *IEEE Microwave Magazine* **2** 59–71
- [21] Yao J J 2000 RF MEMS from a device perspective *J. Micromech. Microeng.* **10** R9
- [22] McKendry R, Zhang J, Arntz Y, Strunz T, Hegner M, Lang H P, Baller M K, Certa U, Meyer E, Güntherodt H-J and Gerber C 2002 Multiple label-free biodetection and quantitative DNA-binding assays on a nanomechanical cantilever array *Proc Natl Acad Sci U S A* **99** 9783–8
- [23] Boisen A, Dohn S, Keller S S, Schmid S and Tenje M 2011 Cantilever-like micromechanical sensors *Rep. Prog. Phys.* **74** 036101
- [24] Akiyama T., Gautsch S., De Rooij N. F, Staufer U., Niedermann P, Howald L, ... & Hecht M H 2001 Atomic force microscope for planetary applications *Sensors and Actuators A: Physical* **91**(3), 321-325
- [25] Howe R T and Muller R S 1986 Resonant-microbridge vapor sensor *IEEE Transactions on Electron Devices* **33** 499–506
- [26] Www2.imec.be. Imec news-imec [Internet]. 2015 [cited 1 October 2015]. Available from: [http://www2.imec.be/be\\_en/press/imec-news/gassensor.html](http://www2.imec.be/be_en/press/imec-news/gassensor.html)
- [27] Chomas L.C. et al. 2003 Low-cost manufacturing/packaging process for MEMS inertial sensors *Proc 36th Intl. Symposium on Microelectronics (IMAPS 2003)*
- [28] Waggoner P S, Varshney M and Craighead H G 2009 Detection of prostate specific antigen with nanomechanical resonators *Lab Chip* **9** 3095–9
- [29] Chan P C H, Yan G, Sheng L, Sharma R K, Tang Z, Sin J K O, Hsing I-M and Wang Y 2002 An integrated gas sensor technology using surface micro-machining *Sensors and Actuators B: Chemical* **82** 277–83
- [30] Schomburg W K 2011 *Introduction to Microsystem Design* vol 1 (Berlin, Heidelberg: Springer Berlin Heidelberg)
- [31] Senkal D, Ahamed M J, Ardakani M H A, Askari S and Shkel A M 2015 Demonstration of 1 Million -Factor on Microglassblown Wineglass Resonators With Out-of-Plane Electrostatic Transduction *Journal of Microelectromechanical Systems* **24** 29–37
- [32] Lee J E-Y and Seshia A A 2008 Square wine glass mode resonator with quality factor of 4 million 2008 *IEEE Sensors* 2008 IEEE Sensors pp 1257–60
- [33] Marx K A 2003 Quartz Crystal Microbalance: A Useful Tool for Studying Thin Polymer Films and Complex Biomolecular Systems at the Solution–Surface Interface *Biomacromolecules* **4** 1099–120
- [34] Bhattacharyya P, Basu P K, Mondal B and Saha H 2008 A low power MEMS gas sensor based on nanocrystalline ZnO thin films for sensing methane *Microelectronics Reliability* **48** 1772–9
- [35] Gau J-J, Lan E H, Dunn B, Ho C-M and Woo J C S 2001 A MEMS based amperometric detector for E. Coli bacteria using self-assembled monolayers *Biosensors and Bioelectronics* **16** 745–55
- [36] Carrascosa L G, Moreno M, Álvarez M and Lechuga L M 2006 Nanomechanical biosensors: a new sensing tool *TrAC Trends in Analytical Chemistry* **25** 196–206
- [37] Takahashi K, Oyama H, Misawa N, Okumura K, Ishida M and Sawada K 2013 Surface stress sensor using MEMS-based Fabry–Perot interferometer for label-free biosensing *Sensors and Actuators B: Chemical* **188** 393–9

- [38] Zhu A Y, Yi F, Reed J C, Zhu H and Cubukcu E 2014 Optoelectromechanical Multimodal Biosensor with Graphene Active Region *Nano Lett.* **14** 5641–9
- [39] Stifter M, Sachse M, Sauter T, Hortschitz W and Keplinger F 2012 Pressure dependence of the quality factor of a micromachined cantilever in rarefied gases *J. Phys.: Conf. Ser.* **362** 012033
- [40] Rollier A-S, Legrand B, Collard D and Buchaillot L 2006 The stability and pull-in voltage of electrostatic parallel-plate actuators in liquid solutions *J. Micromech. Microeng.* **16** 794
- [41] Xu W, Zhang X, Choi S and Chae J 2011 A High-Quality-Factor Film Bulk Acoustic Resonator in Liquid for Biosensing Applications *Journal of Microelectromechanical Systems* **20** 213–20
- [42] Eaton W P and Smith J H 1997 Micromachined pressure sensors: review and recent developments *Smart Mater. Struct.* **6** 530
- [43] Han J, Yeom J, Lee J, Shannon M A and Masel R I 2007 Smooth Contact Mode Capacitive Pressure Sensor with Polyimide Diaphragm 2007 *IEEE Sensors 2007 IEEE Sensors* pp 1468–71
- [44] Zhang Y and Wise K D 1994 Performance of nonplanar silicon diaphragms under large deflections *Journal of Microelectromechanical Systems* **3** 59–68
- [45] Gómez-Martínez R, Hernández-Pinto A M, Duch M, Vázquez P, Zinoviev K, de la Rosa E J, Esteve J, Suárez T and Plaza J A 2013 Silicon chips detect intracellular pressure changes in living cells *Nat Nano* **8** 517–21
- [46] Radosavljevic G J, Zivanov L D, Smetana W, Maric A M, Unger M and Nad L F 2009 A Wireless Embedded Resonant Pressure Sensor Fabricated in the Standard LTCC Technology *IEEE Sensors Journal* **9** 1956–62
- [47] Schwarz P, Feili D, Engel R, Pagel N and Seidel H 2010 Vacuum pressure and gas detection with a silicon based micromechanical squeeze film sensor *Procedia Engineering* **5** 750–3
- [48] Huang C-H, Tsai M-H, Lee C-H, Hsieh T-M, Liou J-C, Chen L-C, Yip M-C and Fang W 2011 Design and implementation of a novel CMOS MEMS condenser microphone with corrugated diaphragm *Solid-State Sensors, Actuators and Microsystems Conference (TRANSDUCERS), 2011 16th International* pp 1026–9
- [49] Weigold J W, Brosnihan T J, Bergeron J and Zhang X 2006 A MEMS Condenser Microphone for Consumer Applications *19th IEEE International Conference on Micro Electro Mechanical Systems, 2006. MEMS 2006 Istanbul* pp 86–9
- [50] White R D, Cheng L and Grosh K 2005 Capacitively sensed micromachined hydrophone with viscous fluid-structure coupling *In Proceedings of the SPIE* pp 121–32
- [51] Sturtzer E, Shahosseini I, Pillonnet G, Lefeuvre E and Lemarquand G 2013 High fidelity microelectromechanical system electrodynamic micro-speaker characterization *Journal of Applied Physics* **113** 214905
- [52] Ergun A, Yaralioglu G and Khuri-Yakub B 2003 Capacitive Micromachined Ultrasonic Transducers: Theory and Technology *Journal of Aerospace Engineering* **16** 76–84

- [53] Erguri A S, Huang Y, Zhuang X, Oralkan O, Yarahoglu G G and Khuri-Yakub B T 2005 Capacitive micromachined ultrasonic transducers: fabrication technology *IEEE Transactions on Ultrasonics, Ferroelectrics, and Frequency Control* **52** 2242–58
- [54] Oralkan O, Ergun A S, Cheng C-H, Johnson J A, Karaman M, Lee T H and Khuri-Yakub B T 2003 Volumetric ultrasound imaging using 2-D CMUT arrays *IEEE Transactions on Ultrasonics, Ferroelectrics, and Frequency Control* **50** 1581–94
- [55] Jeong O C and Konishi S 2007 Fabrication and drive test of pneumatic PDMS micro pump *Sensors and Actuators A: Physical* **135** 849–56
- [56] Hsu Y-C, Lin S-J and Hou C-C 2007 Development of peristaltic antithrombogenic micropumps for in vitro and ex vivo blood transportation tests *Microsyst Technol* **14** 31–41
- [57] Yang X, Grosjean C, Tai Y-C and Ho C-M 1997 A MEMS thermopneumatic silicone membrane valve , *Tenth Annual International Workshop on Micro Electro Mechanical Systems, 1997. MEMS '97, Proceedings, IEEE* pp 114–8
- [58] Brodie I and Muray J J 1982 *The Physics of Microfabrication* (Springer)
- [59] Radjenović B, Radmilović-Radjenović M and Mitrić M 2010 Level Set Approach to Anisotropic Wet Etching of Silicon *Sensors* **10** 4950–67
- [60] Holmgren O, Kokkonen K, Veijola T, Mattila T, Kaajakari V, Oja A, Knuuttila J V and Kaivola M 2009 Analysis of vibration modes in a micromechanical square-plate resonator *J. Micromech. Microeng.* **19** 015028
- [61] Zaumseil J, Meitl M A, Hsu J W P, Acharya B R, Baldwin K W, Loo Y-L and Rogers J A 2003 Three-Dimensional and Multilayer Nanostructures Formed by Nanotransfer Printing *Nano Lett.* **3** 1223–7
- [62] Yeom J and Shannon M A 2010 Detachment Lithography of Photosensitive Polymers: A Route to Fabricating Three-Dimensional Structures *Adv. Funct. Mater.* **20** 289–95
- [63] Javey A, Nam, Friedman R S, Yan H and Lieber C M 2007 Layer-by-Layer Assembly of Nanowires for Three-Dimensional, Multifunctional Electronics *Nano Lett.* **7** 773–7
- [64] Carlson A, Bowen A M, Huang Y, Nuzzo R G and Rogers J A 2012 Transfer Printing Techniques for Materials Assembly and Micro/Nanodevice Fabrication *Adv. Mater.* **24** 5284–318
- [65] Kim S, Wu J, Carlson A, Jin S H, Kovalsky A, Glass P, Liu Z, Ahmed N, Elgan S L, Chen W, Ferreira P M, Sitti M, Huang Y and Rogers J A 2010 Microstructured elastomeric surfaces with reversible adhesion and examples of their use in deterministic assembly by transfer printing *Proc. Natl. Acad. Sci.* **107** 17095–100
- [66] Rogers J A, Lagally M G and Nuzzo R G 2011 Synthesis, assembly and applications of semiconductor nanomembranes *Nature* **477** 45–53
- [67] Keum H, Seong M, Sinha S and Kim S 2012 Electrostatically driven collapsible Au thin films assembled using transfer printing for thermal switching *Appl. Phys. Lett.* **100** 211904
- [68] Zhang Y, Keum H, Park K, Bashir R and Kim S 2014 Micro-Masonry of MEMS Sensors and Actuators *J. Microelectromechanical Syst.* **23** 308–14
- [69] Keum H, Carlson A, Ning H, Mihi A, Eisenhaure J D, Braun P V, Rogers J A and Kim S 2012 Silicon micro-masonry using elastomeric stamps for three-dimensional microfabrication *J. Micromechanics Microengineering* **22** 05501



## Chapter 2

# Theory, Design, and Fabrication Process

*In this chapter, we will first discuss some theoretical aspects that are relevant to the purpose of this study. This includes some basics regarding mechanical vibrations, resonant frequency of a circular plate, and molecular damping due to air surrounding the structure. Then, the design of passive structures and active devices will be presented. Finally, we will detail the fabrication process of the devices.*

## 2.1 Theoretical considerations

In this subchapter, we will present basic theories that are relevant to this study, which include basic theories of vibrations, damping, and fundamental frequency calculation for clamped circular plates.

### 2.1.1 Basic theory of vibrations

The most basic model of a resonator is that of a mass  $m$  attached to a spring with spring constant  $k$ , as shown in Figure 2.1.a. In this model, the mass can be considered as a reservoir of kinetic energy, while the spring can be considered as a reservoir of potential energy. When the structure vibrates, there is an exchange of kinetic and potential energy between the mass and the spring where the total energy is kept constant. Assuming  $F$  as the force acting on the mass and  $x$  as the displacement of the mass, the equation of motion of this model can be written as:

$$\begin{aligned} F &= m \ddot{x} \\ -kx &= m \ddot{x} \\ m\ddot{x} + kx &= 0 \end{aligned} \quad (2.1)$$

And the solution of this differential equation is

$$\begin{aligned} x &= x_0 \cos(\omega_0 t) \\ \omega_0 &= \sqrt{\frac{k}{m}} \end{aligned} \quad (2.2)$$

with  $\omega_0$  as the angular resonant frequency, or angular natural frequency, of the system.

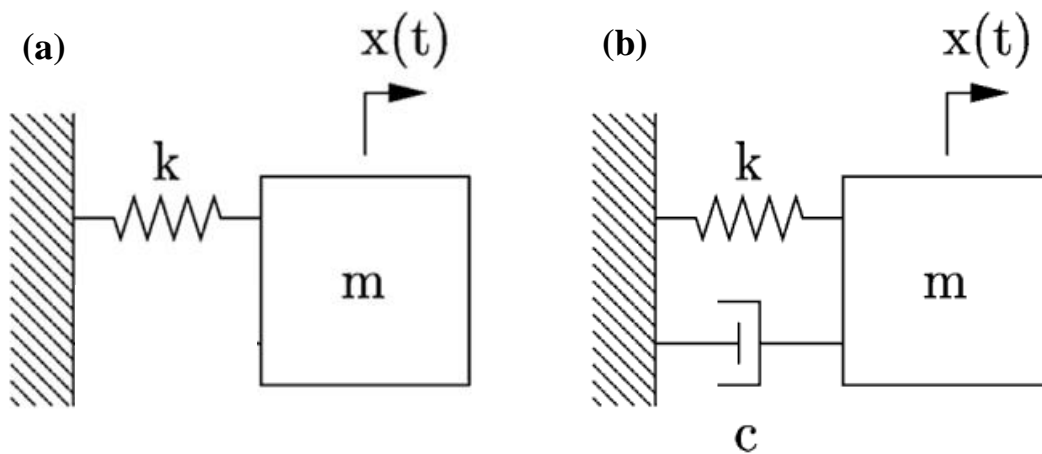


Figure 2.1. Common models used to describe a dynamic vibration: (a) a spring-mass system. (b) a spring-damper-mass system.

A more realistic resonator model is shown in Figure 2.1.b. This model takes into account a damper with a damping coefficient  $c$ . This damper reflects the fact that most mechanical resonators dissipate energy to their environment, which causes the vibrations to decay if there is no supply of a continuous driving force. For simplicity, the damping is assumed to be proportional to the velocity of the mass,  $\dot{x}$ , which is the case for viscous damping. For free vibrations (*i.e.* with no external driving force), the equation of motion can be written as:

$$\begin{aligned} F &= m \ddot{x} \\ -c\dot{x} - kx &= m \ddot{x} \\ m \ddot{x} + c\dot{x} + kx &= 0 \end{aligned} \quad (2.3)$$

The solution of this differential equation can be expressed as:

$$\begin{aligned} x &= x_0 e^{-\zeta\omega_0 t} \cos(\sqrt{1 - \zeta^2}\omega_0 t - \phi) \\ \omega_0 &= \sqrt{\frac{k}{m}} \\ \zeta &= \frac{c}{2\sqrt{km}} \end{aligned} \quad (2.4)$$

Where  $\phi$  is the phase shift and  $\zeta$  is defined as the damping ratio of the resonator. We can note that expression in Equation 2.2 and 2.4 are very similar: the differences include an exponential term in the solution of the vibration amplitude and  $\sqrt{1 - \zeta^2}$  in the periodic term. The exponential term shows that for damped resonators, the vibration amplitude decays with time due to energy dissipation. The  $\sqrt{1 - \zeta^2}$  term shows that for damped resonators, the resonant frequency is shifted downwards compared to the resonant frequency of undamped structures. It can be also noted that at  $c = 2\sqrt{km}$ ,  $\zeta=1$  and the frequency fall to 0; this corresponds to a condition where the damping of the system is large enough to prevent a vibration. Thus, the conditions where  $\zeta < 1$ ,  $\zeta = 1$ , and  $\zeta > 1$  are referred to as underdamped, critically damped, and overdamped resonators, respectively. In most MEMS resonators oscillating in vacuum or air  $\zeta \ll 1$  (*i.e.* the damping is very small), and the vibration frequency of these devices are practically the same as their natural frequency.

A more realistic condition that reflects the operation mode of MEMS resonators is the case of a forced vibration [1]. In this case, the mass is driven by a force  $F(t)$  at a given frequency  $\omega_d$  ( $F(t) = F_0 \sin(\omega_d t)$ ). Thus, equation (2.3) can be rewritten as:

$$m \ddot{x} + c\dot{x} + kx = F_0 \sin(\omega_d t) \quad (2.5)$$

Which steady state solution is:

$$x = \frac{F_0}{k} \frac{1}{\sqrt{\left(1 - \left(\frac{\omega_d}{\omega_0}\right)^2\right)^2 + (2\zeta \frac{\omega_d}{\omega_0})^2}} \sin(\omega_d t + \phi)$$

$$\phi = \tan^{-1} \left( \frac{2\zeta \frac{\omega_d}{\omega_0}}{1 - \left(\frac{\omega_d}{\omega_0}\right)^2} \right) \quad (2.6)$$

The plot of the normalized amplitude and phase of the system vs. normalized driving frequency (frequency response) according to this model is shown in Figure 2.2. For underdamped case, it can be observed that the vibration amplitude increases as the driving frequency approaches the natural frequency of the system, before decreasing as it becomes larger than the natural frequency. Besides, the phase difference in case of resonance is equal to  $\Phi = 180^\circ$ . This frequency response for underdamped structures is typical for mechanical resonators. Note that Equation (2.6) is a form of Cauchy-Lorentz distribution [2], and is treated as such when the experimental data are fitted to extract characteristic parameters.

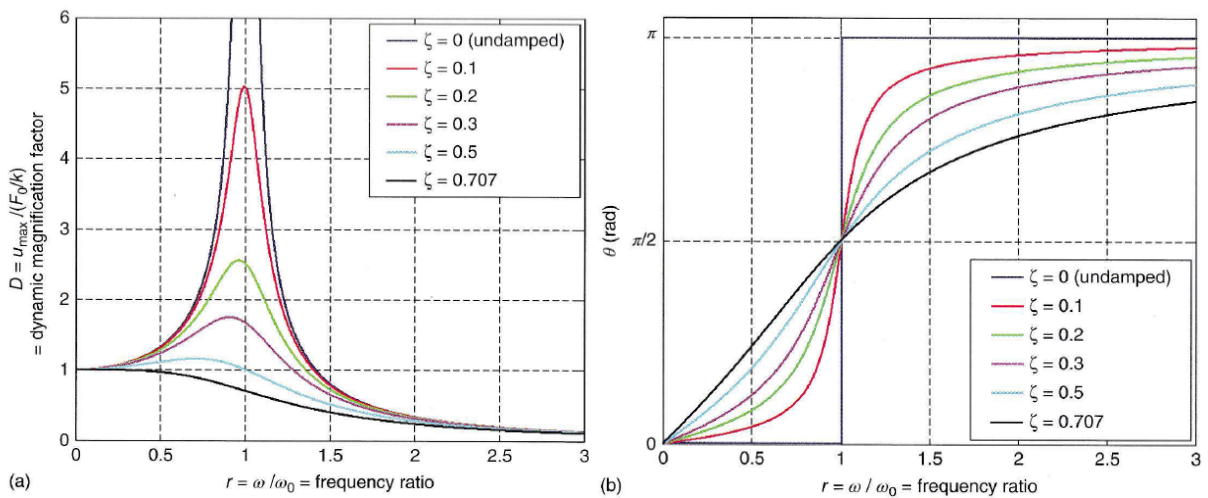


Figure 2.2. Normalized Amplitude and phase vs. frequency plot of a damped resonator in a force vibration with driving force of  $F(t)=F_0 \sin(\omega_d t)$ , plotted for different damping values. Note that the amplitude of the resonator reaches maximum as the frequency of the driving force approaches the resonant frequency, which results in a  $180^\circ$  phase shift in the phase diagram. Taken from [1].

### 2.1.2 Q factor as a measure of dissipation

While we have previously presented the resonator damping in terms of damping coefficient  $c$  and damping ratio  $\zeta$ , the most common way to quantify damping in the field of MEMS is through its quality factor ( $Q$  factor). Quality factor is defined as the ratio of the total resonator energy  $E_{total}$  to the energy dissipated per cycle  $E_{dissipated}$ , multiplied by  $2\pi$ :

$$Q \stackrel{\text{def}}{=} 2\pi \frac{E_{total}}{E_{dissipated}} \quad (2.7)$$

In fact, the  $Q$  factor can be determined by looking at the frequency response of a resonator, and more specifically by measuring the bandwidth  $\Delta\omega$  that is defined by the width of the frequency response curve at which point the energy of the resonator is half its maximum at resonant frequency  $f_0$ . This bandwidth corresponds to the frequency width at half the peak height in a  $x^2$  vs frequency plot, or at  $1/\sqrt{2}$  the peak height in a  $x$  vs.  $f$  plot:

$$Q \approx \frac{\omega_0}{\Delta\omega} = \frac{f_0}{\Delta f} \quad (2.8)$$

This method is used to experimentally determine the  $Q$  factor by data fitting of the frequency response curve of MEMS resonators. While the value by Equation 2.8 is slightly different than Equation 2.7, the difference is negligible for a typical MEMS resonator with  $Q$  factor value above 10.

Note that the  $Q$  factor is inversely proportional to the damping: a higher  $Q$  factor means lower dissipation per cycle. Thus, for  $n$  number of different damping mechanisms with corresponding  $Q$  factors  $Q_1, Q_2, \dots, Q_n$ , the total  $Q$  factor of a resonator  $Q_{total}$  is calculated as:

$$\frac{1}{Q_{total}} = \frac{1}{Q_1} + \frac{1}{Q_2} + \dots + \frac{1}{Q_n} \quad (2.9)$$

As can be seen above, the damping of a device is dominated by the mechanism associated to the lowest  $Q$  factor, and different resonators exhibit different dissipation mechanisms among which some are dominant over the others. Below we provide a short description of some damping mechanisms that are most commonly observed in MEMS devices.

In thermoelastic damping [3-5], the source of dissipation is the irreversible heat flow within the resonator caused by the compressive and tensile strains experienced by the different parts of the resonator as it vibrates. Due to the change in entropy, the compression and stretching of the material respectively reduces and increases its temperature. The thermal gradient built between the different parts of the resonator results in an irreversible heat flow, and thus, dissipation.

In anchor damping [6], the source of dissipation is the transmission of the mechanical vibration between the resonator and its static base structure. This type of damping can be especially dominant in nano-electro mechanical systems (NEMS) where it is described in

terms of phonon tunneling [7,8]. It has been shown that different types of clamping result in significantly different Q factors in NEMS systems.

In viscous damping [9-15], the source of dissipation is the transfer of energy between the resonator and the fluid surrounding it in the form of fluid movement. This description of damping treats the fluid around the resonator as a continuum, and uses fluid mechanics to derive the results. This damping mode is dominant in MEMS of relatively large size operating in liquid or gas, which is the common case for most practical applications.

In molecular damping [16-18], the source of dissipation is the transfer of energy and momentum between the resonator and the gas atoms colliding it. This dissipation mode is similar to the viscous damping in a sense that both can be used to describe damping due to the gas around the resonator. The difference lies in the fact that the molecular damping model assumes no interaction between the atoms of the gas itself, which is already inherent in the continuum mechanics used in the viscous damping model. As a result, the Q factor obtained from the molecular damping model is generally lower than the one obtained from the viscous damping model at high pressure. This damping mode is dominant in MEMS operating in low pressure gas or primary vacuum.

Squeeze film damping [18-25] is a special mode of damping exhibited by resonators with small gap (below 1  $\mu\text{m}$ ) between the resonating part and the substrate. In this damping mode, the restricted nature of the gap leads to both a higher level of damping and a spring effect due to the compressed air pushing back the resonator. Depending on the regime the resonator is operating in, both molecular and viscous descriptions of this damping mode can be used.

Slide film damping [26-27] is a special mode of damping found in MEMS where the resonator element moves parallel to the substrate, such as in accelerometers. This damping mode is a specific type of viscous damping, and the viscosity of the fluid acts as the main contributor to the energy dissipation.

In the broadest sense, the dissipation related to the device itself is classified as intrinsic damping, as opposed to the ones caused by the environment of the device, which are called extrinsic damping. The thermoelastic damping and the clamp damping in the description above are examples of intrinsic damping mechanisms, while the other modes are considered as extrinsic damping. Because extrinsic damping dominates at higher air pressure and is thus relevant for practical applications, the intrinsic damping modes will not be discussed in further details. We will focus our discussion on two extrinsic damping modes that are relevant to our study: the molecular damping and the squeeze film damping.

### 2.1.3 Theoretical description of molecular damping

There are two ways to derive the damping effects in the free molecular regime: by considering the momentum transfer between the resonator and the air [16], and by considering the energy transfer between the resonator and the air [18]. Both approaches are equivalent and results in the same estimation of Q factor. The description provided below derives the damping of a plate in a low-pressure (molecular) regime using the energy transfer method, as described by Bao [18]. Note that the derivation of molecular damping assumes a plate-shaped resonator, although the result can be used for cantilevers, bridges, or suspended plate structures.

Consider a plate resonator in a low vacuum environment. When the plate is static and does not vibrate, the number of gas molecules colliding with each surface  $\Delta n$  for a time span of  $\Delta t$  is proportional to the plate area  $A$ , the gas density  $n$ , the  $x$  component of average gas molecule velocity  $v_x$ , and the change in velocity after colliding  $dv_x$ , and it gives:

$$\Delta n = A n f(v_x) v_x dv_x \Delta t \quad (2.10)$$

With  $f(v_x)$  as the Boltzmann distribution of the gas molecules velocity:

$$f(v_x) = \sqrt{\frac{m_{air}}{2\pi k_b T}} e^{-\frac{m_{air} v_x^2}{2k_b T}} \quad (2.11)$$

With  $T$  as the absolute temperature of gas,  $m_{air}$  as the mass of each gas molecule, and  $k_b$  as the Boltzmann constant. When the plate vibrates, the number of molecules colliding with the plate surface is modified by the speed of the plate  $\dot{x}$ . When the plate is moving up relative to the front surface, the  $x$  component of the velocity of molecules hitting the front plate increases, and the  $x$  component of the velocity of molecules hitting the back surface decreases; vice versa when the plate is moving down relative to the front surface. Thus, the number of gas molecules hitting the front and back surface of the plate  $\Delta n_{front}$  and  $\Delta n_{back}$  is respectively:

$$\begin{aligned} \Delta n_{front} &= A n f(v_x) (v_x + \dot{x}) dv_x \Delta t \\ \Delta n_{back} &= A n f(v_x) (v_x - \dot{x}) dv_x \Delta t \end{aligned} \quad (2.12)$$

Assuming elastic collisions and a large plate mass compared to the molecule mass, the speed of the molecules before and after collision is then  $v_x$  and  $v_x \pm 2\dot{x}$ . The energy transfer between the plate and the gas molecules colliding with the front and back surfaces of the plate,  $\Delta E_{front}$  and  $\Delta E_{back}$ , can then be calculated by evaluating the change of kinetic energy of the gas molecules before and after collision:

$$\begin{aligned} \Delta E_{front} &= A \int \left[ \frac{1}{2} m_{air} (v_x + 2\dot{x})^2 - \frac{1}{2} m_{air} v_x^2 \right] n f(v_x) (v_x + \dot{x}) dv_x \Delta t \\ \Delta E_{back} &= A \int \left[ \frac{1}{2} m_{air} (v_x - 2\dot{x})^2 - \frac{1}{2} m_{air} v_x^2 \right] n f(v_x) (v_x - \dot{x}) dv_x \Delta t \end{aligned} \quad (2.13)$$

The total energy transfer  $\Delta E_{total}$  is then

$$\begin{aligned}\Delta E_{total} &= \Delta E_{front} + \Delta E_{back} \\ \Delta E_{total} &= \frac{1}{2} A m_{air} n \int (4\dot{x}^2 + 4\dot{x}v_x) f(v_x)(v_x + \dot{x}) dv_x \Delta t + \\ &\quad \int (4\dot{x}^2 - 4\dot{x}v_x) f(v_x)(v_x - \dot{x}) dv_x \Delta t\end{aligned}\tag{2.14}$$

Since in most cases the vibration speed of the plate is much slower than the molecule velocity ( $\dot{x} \ll v_x$ ), we can consider that  $(v_x + \dot{x})$  and  $(v_x - \dot{x}) \approx v_x$ , and thus the previous equation becomes

$$\begin{aligned}\Delta E_{total} &= A m_{air} n \int 8\dot{x}^2 f(v_x) v_x dv_x \Delta t \\ \Delta E_{total} &= 4 A m_{air} n \sqrt{\frac{2k_b T}{\pi m}} \dot{x}^2 \Delta t\end{aligned}\tag{2.15}$$

For the majority of cases, a MEMS resonator is driven by a sinusoidal signal, and thus the displacement of the resonator can be expressed as  $x = x_0 \sin(\omega t)$  and its velocity  $\dot{x} = x_0 \omega \cos(\omega t)$ . The energy dissipation of the resonator per cycle is then

$$\begin{aligned}\Delta E_{cycle} &= 4 A m_{air} n \sqrt{\frac{2k_b T}{\pi m_{air}}} \int_0^{2\pi} x_0^2 \omega^2 \cos^2 \omega t \frac{1}{\omega} d(\omega t) \\ &= 4 A m n \sqrt{\frac{2k_b T}{\pi m_{air}}} x_0^2 \omega \pi\end{aligned}\tag{2.16}$$

The quality factor of the plate due to molecular damping  $Q_{molecular}$  for a resonator with total mass  $m$ , thickness of plate  $h$ , and density  $\rho$  is then obtained by evaluating the potential energy  $E_{potential}$  of the resonator and Equation 2.16:

$$\begin{aligned}Q_{molecular} &= \frac{2\pi E_{potential}}{\Delta E_{cycle}} \\ &= 2\pi \frac{\frac{1}{2} k x_0^2}{4 A m n \sqrt{\frac{2k_b T}{\pi m}} x_0^2 \omega \pi}\end{aligned}$$

$$\begin{aligned}
&= 2\pi \frac{\frac{1}{2} (2\pi f_0)^2 m x_0^2}{4Amn \sqrt{\frac{2k_b T}{\pi m}} x_0^2 \omega \pi} \\
&= 2\pi \frac{\frac{1}{2} (2\pi f_0)^2 (Ah\rho) x_0^2}{4Amn \sqrt{\frac{2k_b T}{\pi m}} x_0^2 \omega \pi}
\end{aligned}$$

Using ideal gas law, we can substitute  $n = P/k_b T$ :

$$\begin{aligned}
Q_{molecular} &= 2\pi \frac{\frac{1}{2} (2\pi f_0)^2 (Ah\rho) x_0^2}{4Am \left(\frac{P}{k_b T}\right) \sqrt{\frac{2k_b T}{\pi m}} x_0^2 \omega \pi} \\
&= \left(\frac{\pi}{2}\right)^{1.5} \frac{\sqrt{k_b T/m}}{P} t \rho f
\end{aligned}$$

Or equivalently, in molar units for gas constant  $R$  and molar air mass  $M_{air}$ :

$$Q_{molecular} = \left(\frac{\pi}{2}\right)^{1.5} \frac{\sqrt{RT/M_{air}}}{P} t \rho f \quad (2.17)$$

Note that the derivation of the Q factor in the case of molecular damping presented above is very general, and applies to MEMS resonators of various shapes (cantilevers, bridges, and plates) as long as the vibration is normal to the plate surface.

#### 2.1.4 Theoretical description of squeeze film damping

The nonlinear Reynolds equation for a gas flow between two plates is [26]:

$$\frac{\partial}{\partial x} \left( \rho_{gas} \frac{h^3}{\mu} \frac{\partial P}{\partial x} \right) + \frac{\partial}{\partial y} \left( \rho \frac{h^3}{\mu} \frac{\partial P}{\partial y} \right) = 12 \frac{\partial (h \rho_{gas})}{\partial t} \quad (2.18)$$

With  $\rho_{gas}$  as the gas density,  $P$  as the gas pressure,  $h$  as the gap size, and  $\mu$  as the gas viscosity. This equation is the simplified form of the more general equation for compressible gas. In this equation, the inertial effect of the fluid and the lateral movement of the plate are neglected. The first assumption is valid in MEMS systems that have large surface to volume ratios, which result in the viscous term of the fluid dominating over the inertial term. The second assumption is valid in the special case of squeeze film damping, since the plate only moves normally relative to the rigid base. Since in MEMS devices, the thermal gradient across the film thickness is negligible, the density of gas is proportional to the pressure, and thus we can replace  $\rho_{gas}$  by  $P$ :

$$\frac{\partial}{\partial x} \left( P \frac{h^3}{\mu} \frac{\partial P}{\partial x} \right) + \frac{\partial}{\partial y} \left( P \frac{h^3}{\mu} \frac{\partial P}{\partial y} \right) = 12 \frac{\partial(hP)}{\partial t} \quad (2.19)$$

To simplify the equation even further, we can consider that the gap between the moving device and the static substrate consists of an equilibrium position  $h_0$  and a perturbation  $\Delta h$  ( $h = h_0 + \Delta h$ ); similarly, the pressure can be considered to consist of an equilibrium constant pressure  $P_0$  and a varying term  $\Delta P$  ( $P = P_0 + \Delta P$ ). For small perturbations in both plate movement and pressure ( $\Delta p \ll P_0$  and  $\Delta h \ll h_0$ ), the equation can be linearized into:

$$P_0 \left( \frac{\partial^2 \Delta P}{\partial x^2} + \frac{\partial^2 \Delta P}{\partial y^2} \right) - \frac{12\mu}{h_0^2} \frac{\partial P}{\partial t} = \frac{12\mu P_0}{h_0^3} \frac{\partial h}{\partial t} \quad (2.20)$$

This equation can be solved to obtain the damping force of a resonator, which solution can generally be written as:

$$F_{damping} = P_0 A \Delta h (-f_e(\sigma) \cos(\omega t) + f_d(\sigma) \sin(\omega t))$$

$$\sigma = \frac{12\mu\omega w^2}{P_0 h_0^2} \quad (2.21)$$

With  $A$  as the plate area,  $f_e$  and  $f_d$  as the elastic and viscous damping elements of the solution,  $h$  as the gap height,  $P$  as the air pressure,  $\mu$  as the viscosity of the medium surrounding the structure,  $w$  as the characteristic length of the structure (width for cantilevers or radius for circular plates) and the quantity  $\sigma$  is referred to as the squeeze number. It should be noted that the terms that contain the elastic and viscous damping element have opposite signs and phases. In terms of one-dimensional spring-damper model described before, this means that the air inside the gap acts both as a spring and a damper:

$$F_{damping} = -k_{squeeze} x - c_{squeeze} \dot{x}$$

$$k_{squeeze} = \frac{P_0 A f_e(\sigma)}{h_0}$$

$$c_{squeeze} = \frac{P_0 A f_d(\sigma)}{h_0 \omega} \quad (2.22)$$

It can be observed that while the damping force dominates at low squeeze number, the elastic force dominates at higher squeeze number, which corresponds to higher frequencies. It can also be noted that at a certain squeeze number (or frequency), the amount of elastic force is equal to the amount of viscous damping of the air inside the gap. This frequency is called the cutoff frequency  $\omega_c$ , which for a plate resonator can be calculated as:

$$\omega_c = \frac{\pi^2 h^2 P_0}{12\mu w^2} \quad (2.23)$$

The behavior of a resonator with different values of resonant frequency  $\omega$  in relation to cutoff frequency  $\omega_c$  is shown in Figure 2.3 (taken from [26]). In case of  $\omega \ll \omega_c$ , the viscous damping coefficient can be considered constant, and the elastic damping is negligible; the

frequency response curve is typical of the spring-damper resonator described before. In case of  $\omega \approx \omega_c$ , both the viscous and elastic damping terms are significant, and this results in a dip of amplitude just before resonance and a lower peak of resonance. In case of  $\omega \gg \omega_c$ , the viscous damping have only a slight effect on the resonance behavior because the air inside the gap does not have enough time to move in and out of the gap at such high resonator frequency. The influence of elastic damping is also slight because devices exhibiting high resonant frequencies have high spring constants relative to the elastic damping coefficient.

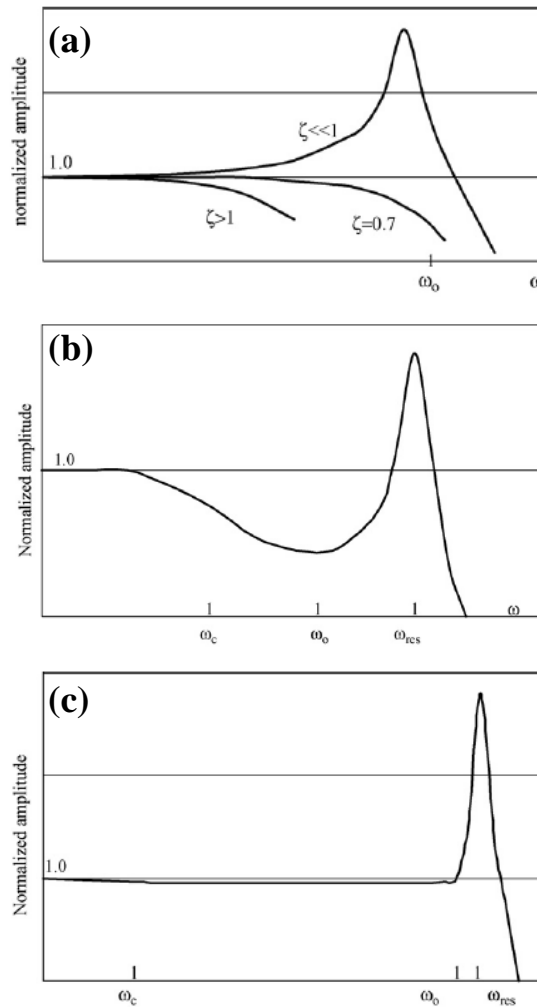


Figure 2.3. Behavior of a mechanical resonator under squeeze film damping according to the value of its resonant frequency relative to its cutoff frequency: (a)  $\omega \ll \omega_c$  (b)  $\omega \approx \omega_c$  (c)  $\omega \gg \omega_c$ . The squeeze film effect is particularly pronounced when  $\omega \approx \omega_c$ , and not so significant on two other cases. Taken from [25].

It is meaningful to calculate the cutoff frequency of our devices to determine under which conditions our device operates. Putting in values of  $h = 200$  nm (smallest gap used for active devices),  $P_0 = 10^5$  Pa (atmospheric pressure operation),  $\mu = 18.6$   $\mu$ Pa.s (air viscosity at  $RT$ ), and  $w = 34$   $\mu$ m (diameter of a plate with  $r = 14$   $\mu$ m) yields a cutoff frequency of 24.8 kHz. This cutoff frequency is much lower than the measured resonant frequency of the device ( $\omega = 4.7$  MHz), and thus the structures and devices in this study operates in the  $\omega \gg \omega_c$  regime, where the effect of squeeze film damping is negligible. This is also supported by the fact that unlike the assumptions used in the derivations above, the structures in this study are enclosed or display small air holes, which thus reduces the air flow to and from the gap underneath the plate, which in turn minimizes the viscous damping.

### 2.1.5 Fundamental frequency of a vibrating plate

In this subchapter, we derive the fundamental frequency for a circular plate using the Rayleigh method [28]. First, we express the kinetic and potential energies of a resonator. If the damping of the resonator is neglected, the maxima of kinetic and potential energies have the same value. By equating both the kinetic and potential energies, and assuming the resonator's mode shape is known, we can evaluate its resonant frequency.

We start by writing the general expression for kinetic energy  $E_{kinetic}$ :

$$E_{kinetic} = \frac{m\dot{x}^2}{2} \quad (2.24)$$

In the case of plates vibrating perpendicularly to the plate surface (the  $x$ - $y$  plane) in the  $z$  direction, each infinitesimal volume element  $dx dy dz$  of the plate with density  $\rho$  moves with different speed  $\dot{x}$ , which is equal to  $dz/dt$ . Thus, each element of the plate has a kinetic energy  $dE_{kinetic}$ :

$$dE_{kinetic} = \frac{\rho dx dy dz \dot{x}^2}{2} = \frac{\rho dx dy dz}{2} \left(\frac{dz}{dt}\right)^2 \quad (2.25)$$

The displacement of the membrane in the  $z$  direction is a function of time  $t$  and position on the membrane  $x$  and  $y$ . We will assume that  $z$  can be represented by a product of a term which is a function of only  $x$  and  $y$  and another term which is a function of only  $t$ :

$$z = z(x, y, t) = A u(x, y) \cos(\omega t + \phi)$$

$$\frac{dz}{dt} = -A\omega u(x, y) \sin(\omega t + \phi) \quad (2.26)$$

With  $u$ , the mode shape of the resonator,  $A$ , the amplitude of the resonator,  $\omega$ , the vibrating frequency, and  $\phi$ , the initial phase difference. Substituting Equation 2.26 into Equation 2.25 yields:

$$\begin{aligned}
dE_{kinetic} &= \frac{\rho \, dx \, dy \, dz}{2} (-A\omega u(x,y) \sin(\omega t + \phi))^2 \\
&= \frac{\rho \, dx \, dy \, dz}{2} A^2 \omega^2 u^2 \sin^2(\omega t + \phi)
\end{aligned} \tag{2.27}$$

The total kinetic energy of the plate is obtained by integrating (2.27):

$$\begin{aligned}
E_{kinetic} &= \int dE_{kinetic} = \int \frac{\rho \, dx \, dy \, dz}{2} A^2 \omega^2 u^2 \sin^2(\omega t + \phi) \\
&= \frac{\rho A^2 \omega^2}{2} \int u^2 \sin^2(\omega t + \phi) \, dx \, dy
\end{aligned} \tag{2.28}$$

It can be noted that the maximum value of kinetic energy  $E_{k \, max}$  is obtained when  $\sin(\omega t + \phi) = 1$ . This value is equal to the maximum value of potential energy  $E_{p \, max}$  due to conservation of energy (neglecting damping):

$$E_{k \, max} = E_{p \, max} = \int dE_{k \, max} = \frac{\rho \, dz}{2} A^2 \omega^2 \int u^2 \, dx \, dy \tag{2.29}$$

The resonance frequency is then obtained by rearranging Equation 2.29 above:

$$f = \frac{\omega}{2\pi} = \frac{1}{2\pi} \sqrt{\frac{2 E_{p \, max}}{\rho \, dz \, A^2 \int u^2 \, dx \, dy}} \tag{2.30}$$

Thus, the resonant frequency of the structure can be determined if the mode shape and the potential energy of the mode are known. In most applications, as in the case in our study, we are mostly interested in vibration at the fundamental frequency, which is the lowest resonant frequency of the structure. In this case, the shape of the plate when deformed by a static pressure serves as a good approximation for the plate's first vibration mode.

The maximum potential energy of the plate can be determined by the Ritz method [28], with the following results in polar coordinates:

$$\begin{aligned}
E_p &= \int_0^{2\pi} d\varphi \int_0^R r \, dr \left[ \frac{E_m \, t^3}{24(1-\nu_m^2)} \left( \frac{\partial^2 z}{\partial r^2} + \frac{1}{r} \frac{\partial z}{\partial r} + \frac{1}{r^2} \frac{\partial^2 z}{\partial \varphi^2} \right)^2 + \right. \\
&\quad \left. \frac{t}{2} \left( \sigma_r \left\{ \frac{\partial z}{\partial r} \right\}^2 + \frac{\sigma_\varphi}{r^2} \left\{ \frac{\partial z}{\partial \varphi} \right\}^2 \right) + \frac{t}{8} \frac{E_m}{(1-\nu_m^2)} \left( \frac{\partial z}{\partial r} \right)^4 - z \, \Delta p \right]
\end{aligned} \tag{2.31}$$

With  $E_m$  as the young modulus of the plate material,  $t$  as the plate thickness,  $\sigma$  as the internal stress within the plate material, and  $\nu_m$  as the poisson's ratio of plate material. The first term in Equation 2.31 corresponds to the bending moment of the plate. The second term corresponds to the internal stress of the plate, both in its radial and angular components. The third term corresponds to the stress caused by the straining of the plate. The fourth term corresponds to the external pressure applied to the plate. For thick plates, as in the case for structures and devices considered in this study, the third term is small enough and can be neglected.

The mode shape is simply obtained by normalizing the deflection of the plate due to a constant pressure. The solution is determined from the theory of plates [29] to be:

$$u_r = \left(1 - \frac{r^2}{R^2}\right) \quad (2.32)$$

With  $R$  as the radius of the circular plate. Putting Equation 2.31 and 2.32 into Equation 2.30, neglecting the stress caused by plate straining, yields the analytical fundamental frequency for a circular thick plate:

$$f_{analytical} = \sqrt{\frac{5}{3}} \frac{1}{\pi R \sqrt{\rho}} \sqrt{\frac{4}{3} \frac{E}{1-\nu^2} \frac{t^2}{R^2} + \sigma_0} \quad (2.33)$$

## 2.2 Design and fabrication of suspended structures using micro-masonry.

In this subchapter, the design and the fabrication process of the suspended plate devices will be presented, with separate discussions for the passive and active structures. First, we will provide the general concept of the devices, and then we will give further details regarding each of the components. Finally, the fabrication steps required to create the structures and devices will be presented. All of the fabrication process will be done in LAAS, with the exception of the micro-masonry step, which is done at Seok Kim's Lab at University of Illinois at Urbana, Champaign, USA.

### 2.2.1 Design and fabrication of the passive structures

The basic concept of a suspended plate passive structure is illustrated in Figure 2.4. The passive structure consists of two parts, the silicon nanoplate and the base structure. The silicon nanoplate (known as the ink) is fabricated out of a device layer of a silicon on insulator (SOI) wafer using lithography and etching. The base structure is fabricated out of silicon dioxide layer on top of a bulk silicon wafer. The base structures are etched with cavities that define the shape of the suspended plate resonator. Using microtip stamps, the silicon nanoplate is transferred from the SOI wafer (known as donor wafer) onto the base structures on the bulk silicon wafer (known as acceptor wafer). The bulk wafer containing the combined structure is then thermally annealed to create a rigid bond between the inks and the base structures, resulting in a passive resonating structure.

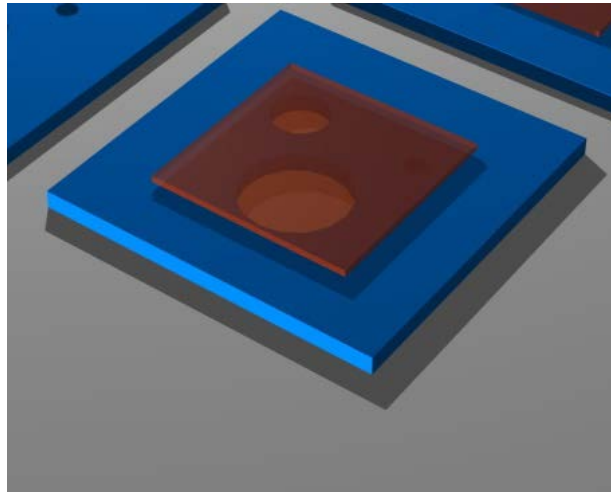


*Figure 2.4. Illustration of a suspended plate passive structure. The structure consists of the silicon nanoplate (brown) and the base structure (blue) which contains cavities. The silicon nanoplate is transferred using micro-masonry on top of the base structure; the combined structure is then thermally annealed to create a strong and rigid bond between the two components.*

The design details for the first batch of passive structure are as follows: The silicon nanoplate inks have a lateral dimension of  $100 \times 100 \mu\text{m}$  with a square shape and thickness of  $t = 0.34 \mu\text{m}$ . This ink size was chosen due to familiarity of the Illinois group regarding its process parameters.

The base structures have a lateral dimension of  $120 \mu\text{m}$  with a square shape, giving the silicon nanoplates  $10 \mu\text{m}$  margin of error on four cardinal directions. The thickness of the base structure (and the gap size) was designed to be  $h = 0.66 \mu\text{m}$ . To test the influence of the type of base on the result of the micro-masonry process, we have used both thermally grown and PECVD deposited  $\text{SiO}_2$ . Cavities are defined within the base structures and can be differentiated in terms of shape, size, number of cavities, and presence of an air vent. We have included both circular and square cavities to test the ability of the plate to conform to various shapes. We also varied the size of the circular-shaped cavities ( $r = 30 \mu\text{m}$  and  $r = 10 \mu\text{m}$ ), as well as the square-shaped cavities (with side length of  $r = 60 \mu\text{m}$ ,  $r = 20 \mu\text{m}$ , and  $r = 4 \mu\text{m}$ ). We have also included multiple (4) square-shaped cavities in a single base in order to test the possibility of fabricating several resonators using a single silicon plate. On some structures, an air vent connecting the cavity to the environment was added to check the influence of air inside the cavity on the Q factor of the passive structures.

The chips that contain the base structures have a lateral dimension of  $1 \times 1 \text{ cm}$  to conform with the sample holder of our Fabry-Perot setup. Each chip contains 16 base structures

arrayed in 4 x 4 layout, with letters A – D signifying the rows, and numbers 1 – 4 signifying the columns. The chip layout is shown in Figure 2.5.

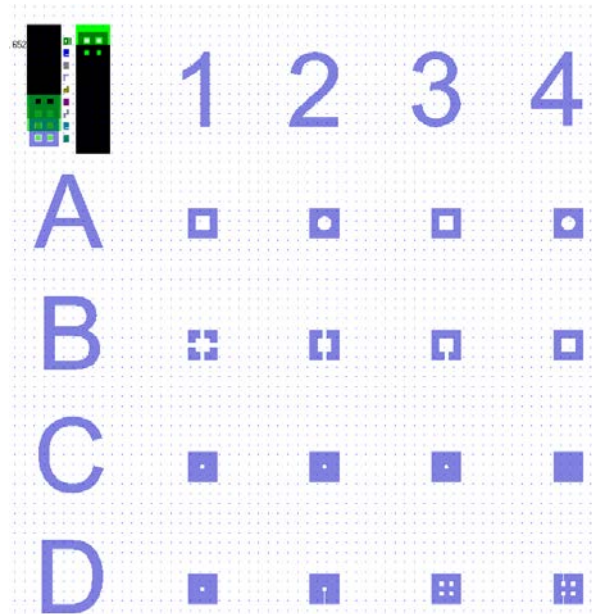


*Figure 2.5. The acceptor chip layout for the first fabrication batch. The base structures contain cavities of different sizes and shapes, and include cavities with air vents.*

The design details for the second batch of passive structure are as follows: The silicon nanoplate inks have a lateral dimension of  $100 \times 100 \mu\text{m}$  with a square shape, identical with the first batch. However, two values of thickness were used,  $t = 0.34 \mu\text{m}$  and  $1.2 \mu\text{m}$ . The ink with the  $1.2 \mu\text{m}$  thickness was used in response to buckling observed on some of the passive structures to see whether the increased stiffness has a significant impact on the device yield.

The base structures have a lateral dimension of  $120 \times 120 \mu\text{m}$  with a square shape, identical with the first batch. Three values of thickness of the base structure (and the gap size) were used to test the influence of gap size on air damping;  $h = 0.66, 1.25 \mu\text{m}$ , and  $2.5 \mu\text{m}$ . Only PECVD deposited  $\text{SiO}_2$  was used, since measurement on the first batch of passive structure did not show significant difference between PECVD and thermally grown  $\text{SiO}_2$ . Unlike the first fabrication batch, only circular cavities were used and no square-shaped cavities were present to simplify any theoretical analysis. The passive structures of the second fabrication batch were designed to investigate buckling, squeeze film damping, and crosstalk uncovered during the characterization of the previous batch (see chapter 4). The new samples were designed with cavities ranging from  $r = 8 - 30 \mu\text{m}$  to investigate the maximum membrane size at which the buckling becomes significant and problematic. It is also of practical interest to investigate crosstalk between cavities fabricated using a single plate for the possible production of devices with high membrane density. The multi-cavity devices fabricated during the first batch were suspected to exhibit some mechanical crosstalk (see Chapter 4), so

we have included devices with different cavity sizes in the second fabrication batch, thus displaying different resonant frequencies. This would ease the identification of crosstalk phenomena compared to devices including resonators with similar resonant peaks. To study the effect of cavity size on crosstalk, we designed two devices with different sets of cavity (Figure 2.5). Devices C2 & D2 include a smaller set of cavities ( $r = 8, 10, 12 \mu\text{m}$ ) while device C3 & D3 have a larger set of cavities ( $r = 15, 18, 20 \mu\text{m}$ ). In order to study the influence of the distance between the various cavities on possible crosstalk effects, we have included devices with inter-cavity distances of  $20 \mu\text{m}$  (devices C2 & D2) and  $40 \mu\text{m}$  (devices C1 & D1).

The chips which contained the base structures have identical size and layout as the first batch. The chip layout is shown in Figure 2.7.

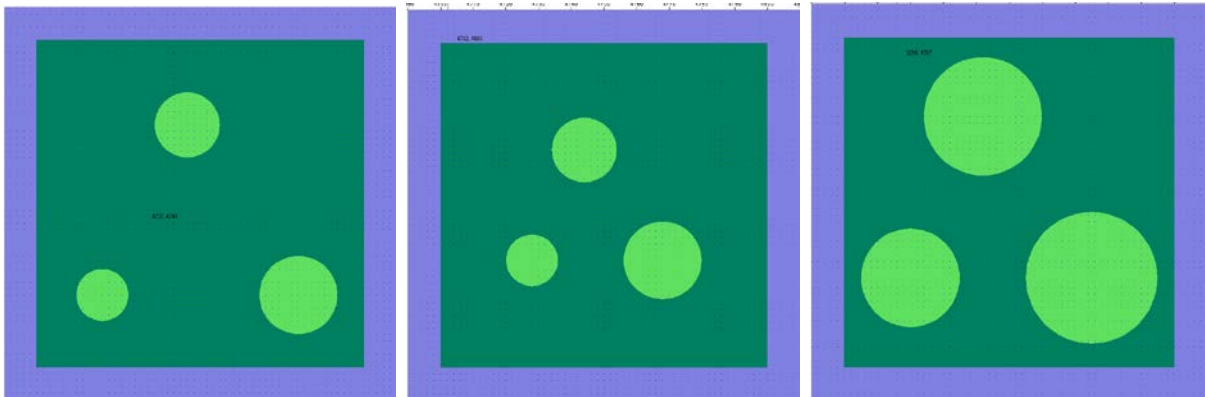


*Figure 2.6. Devices with multiple cavities for the fabrication of multiple resonators with a single plate. From left to right: devices C1 ( $r = 8, 10, 12 \mu\text{m}$ ;  $40 \mu\text{m}$  spacing), C2 ( $r = 8, 10, 12 \mu\text{m}$ ;  $20 \mu\text{m}$  spacing), and C3 ( $r = 15, 18, 20 \mu\text{m}$ ;  $20 \mu\text{m}$  spacing).*

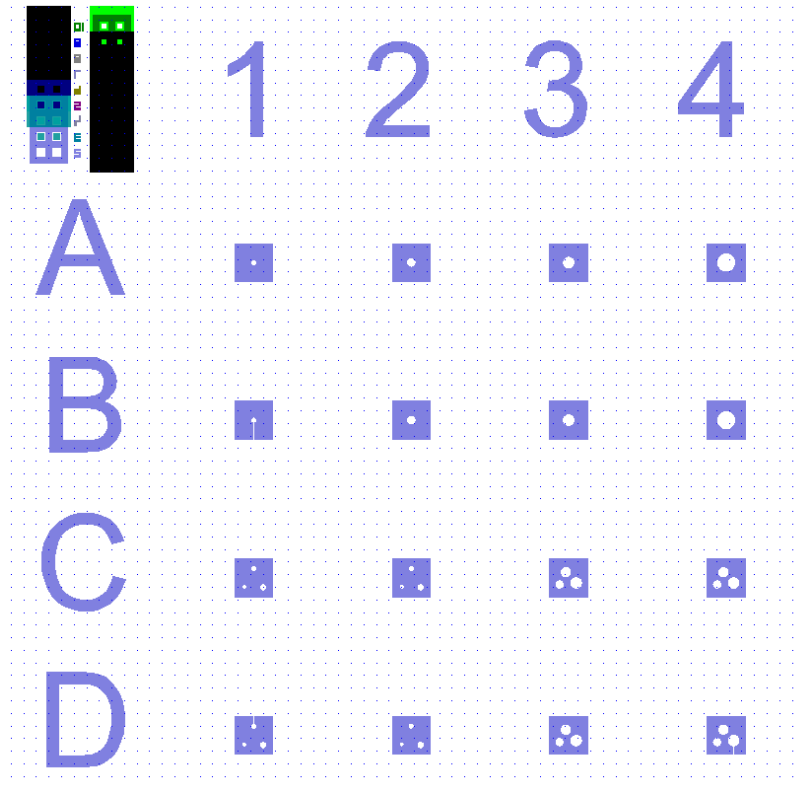


*Figure 2.7. The acceptor chip layout of the second fabrication batch. The varying sizes of the circular cavities were designed to evaluate the influence of cavity size on plate buckling. Devices containing multiple cavities of different sizes were used to test the presence of mechanical crosstalk between the resonators.*

The fabrication steps of the passive structures is illustrated in Figure 2.8. The nanoplate inks are fabricated starting from SOI wafers (BT electronics, 0.34/1/500  $\mu\text{m}$  thickness, 100 mm, boron doped, 14-22  $\Omega\cdot\text{cm}$  resistivity). First, 100  $\mu\text{m} \times 100 \mu\text{m}$  squares are patterned using photolithography to define the ink shapes in the silicon device layer. Then, dry reactive ion etching (RIE) is performed to form the nanoplates that remain attached to the buried oxide layer. Subsequently, HF solution is utilized to remove unnecessary box oxide layer as well as a small region beneath the silicon nanoplates. This undercut region is filled with photoresist (PR) followed by complete removal of oxide layer resulting in suspended nanoplates with PR anchors. The suspended nanoplates are then transfer printed through micro-masonry leaving PR anchors behind on the donor substrate. The thickness of the silicon nanoplate ink is defined by the thickness of the top silicon layer of the SOI wafers, which is 0.34  $\mu\text{m}$  in our case.

The receiver chips are fabricated by first depositing a PECVD (300  $^{\circ}\text{C}$ , 1 mbar) silicon oxide layer on top of a bulk silicon wafer, with thickness of  $t = 0.66, 1.25 \mu\text{m}$ , or  $2.5 \mu\text{m}$  depending

on the fabrication batch. For some receiver chips of the first batch, the silicon oxide was thermally grown on top of the silicon wafer until it has reached the thickness of  $t = 0.66 \mu\text{m}$ . Afterwards, the base structure is patterned using photolithography followed by RIE ( $17^\circ\text{C}$ ,  $7 \cdot 10^{-3}$  mbar). The base structures consist of square shapes ( $120 \mu\text{m}$  side lengths) with one or more cavities. Base structures with multiple cavities result in multiple nanoplate devices obtained in a single transfer printing step, thus enabling a parallel fabrication capability. Finally, and prior to the transfer-printing of the ink onto the base structure, the receiver wafer is diced into  $1 \text{ cm} \times 1 \text{ cm}$  chips.

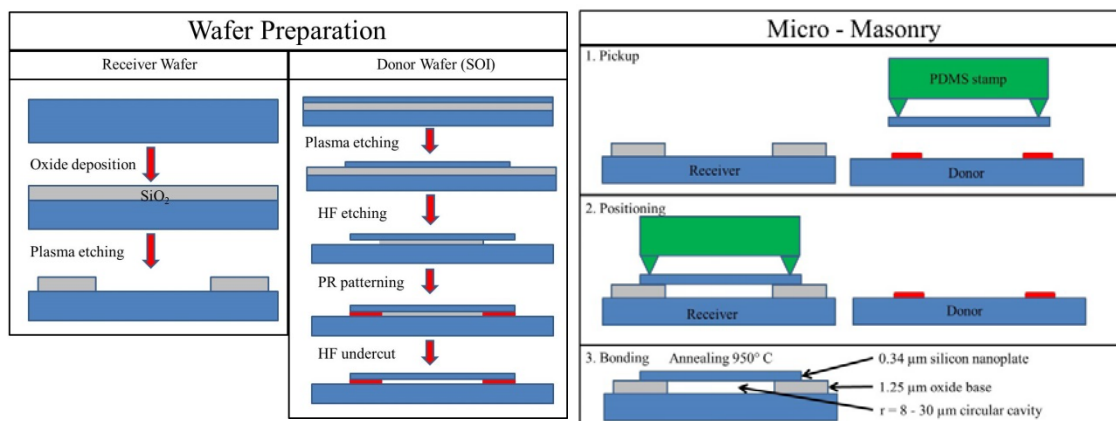
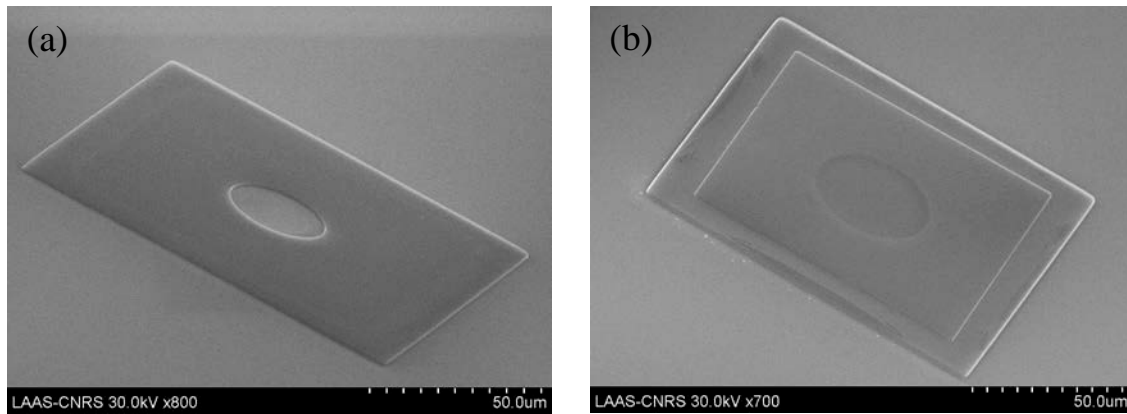


Figure 2.8. Illustration of the fabrication process of the passive structures. The silicon nanoplates were prepared from a donor SOI wafer, while the base structures were prepared on top of a bulk silicon acceptor wafer. Micro-masonry was used to transfer the nanoplates on top of the base structures, and thermal anneal was used to bond the two parts together.

Transfer printing of the silicon nanoplate inks is then achieved by means of PDMS microtip stamps. These stamps have pyramidal tips that provide appropriate adhesion force both during the pickup and the printing step. The stamp used for this study has a square layout, with four tips located at the edge of the square. The inks are aligned and transferred onto the base using appropriate speed and force profile. The chip is finally annealed at  $950^\circ\text{C}$  to permanently bond the base and the membrane. As stated previously, the micro-masonry step was done at Seok Kim's Lab at University of Illinois at Urbana, Champaign, USA. Figure 2.9 shows SEM pictures of a resulting typical structure before and after the transfer printing process.



*Figure 2.9. SEM image of the structure considered in this study: (a) 1.25  $\mu\text{m}$  thick  $\text{SiO}_2$  base structure hosting a 20  $\mu\text{m}$  radius cavity before the transfer printing process (b) the same structure after transfer printing the 0.34  $\mu\text{m}$  thick nanoplate ink and thermal annealing.*

### **2.2.2 Design and fabrication of the active devices**

The basic concept of the active devices is illustrated in Figure 2.10. As can be observed, the device shares many similarities with the passive structure, consisting of a silicon nanoplate on top of an oxide base structure. In addition, the active device has several different components to enable electrostatic actuation and sensing, including a silicon bottom electrode, gold electrical interconnects to the top and bottom electrodes, and pairing layout for compensated capacitive measurement. The silicon for the top and bottom electrodes is highly doped to increase their conductivity and reduce their  $RC$  time constant. After the micro-masonry process and the annealing of the silicon nanoplates and the base structures, the interconnects are formed using sputtering and liftoff technique. Finally, the device is attached to a PCB and wire bonded as the finishing step.

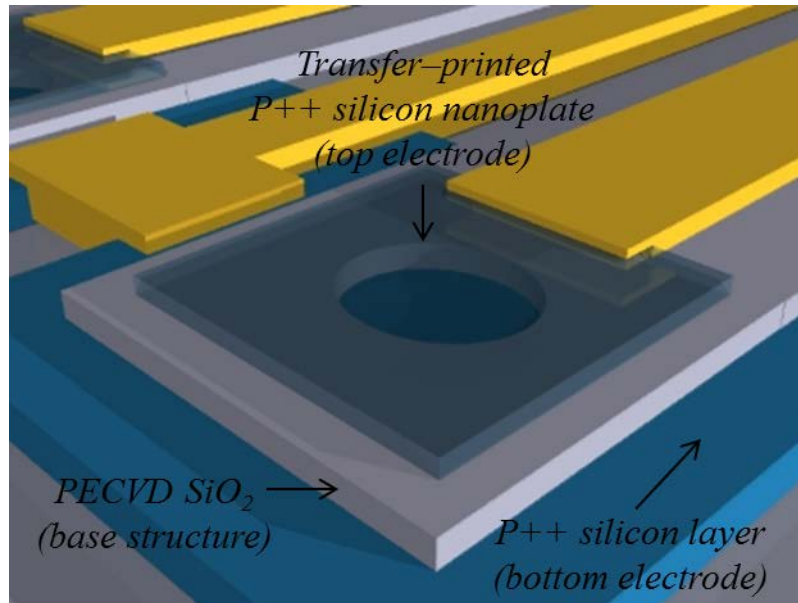


*Figure 2.10. Illustration of a suspended plate active device. The device has several features not found in the passive device, such as a silicon bottom electrode, gold electrical interconnects to the top and bottom electrodes, and pairing layout.*

The design details for the active structures is shown in Figure 2.11, where the blue layer indicates the bottom electrode, the green layer indicates the insulating base, the red layer indicates the metallization, and the crisscrossed layer indicates the position of silicon plate to be transfer-printed using micro-masonry. Detailed description of each component is as follows:

The nanoplate inks have lateral dimensions of  $100 \times 100 \mu\text{m}^2$  and a thickness of  $t = 0.34 \mu\text{m}$ , which is similar to those used in passive structures. Since in active device the nanoplates are used as a top electrode, it is desirable that it has low resistivity to lower the RC time constant. This is achieved by doping the SOI wafer used as the donor wafer with boron in a furnace.

The base structure itself was made out of PECVD deposited  $\text{SiO}_2$  with width of  $120 \mu\text{m}$  and thickness (gap value) of  $h = 0.2 \mu\text{m}$ . While very small gap was desirable for capacitive detection, smaller gap could lead to device collapse and sticking during the transfer-printed process. The base structure also extended beyond the bottom electrode to accommodate both the interconnect lines and the contact pads. The cavity size used in the active device is a compromise between prevention of device failures to buckling and ease of capacitive detection. While it is desirable to have a large device area above the cavity to increase the static capacitance and obtain higher signal to noise ratio, device with larger span also have

less rigidity and buckle more easily when exposed to compressive stress. As a compromise, cavity radius between  $r = 20$  and  $7 \mu\text{m}$  were chosen. To prevent mixing of detection signals, the paired devices had different cavity designs, with one containing a single cavity and the other containing two cavities. The cavities size was designed such that for each of the paired device the resonant frequency of both devices were different, and the total area under the cavity was approximately equal. In this study, three types of device pairing were included according to the cavity radius and quantity: 1 x  $r = 20 \mu\text{m}$  cavity paired with 2 x  $r = 14 \mu\text{m}$  cavity; 1 x  $r = 10 \mu\text{m}$  cavity paired with 2 x  $r = 7 \mu\text{m}$  cavity; and 1 x  $r = 15 \mu\text{m}$  cavity paired with 1 x  $r = 13 \mu\text{m}$  and 1 x  $r = 7 \mu\text{m}$  cavity.

The bottom electrode consisted of a  $250 \times 200 \mu\text{m}$  rectangle underneath the base structure, fabricated out of a heavily doped device layer of an SOI wafer. The electrode size was a compromise between the  $RC$  time constant requirements that favors small bottom electrode (to minimize parasitic effects) and fabrication requirements that favors large size tolerance to deal with process misalignments.

The metal interconnects has a width of  $80 \mu\text{m}$  and were fabricated by Cr and Au sputtering. Two separate connections were made to each of the top electrodes in order to drive the devices with separate electrical signals. One connection was made in parallel to the bottom electrode of both paired devices in order to measure the charge difference during mechanical resonance. In our device layout, the interconnect lines were not planar because of the thickness of the resonator plate and the silicon layer used as the bottom electrode, thus respectively inducing a vertical step of  $0.34 \mu\text{m}$  and  $2 \mu\text{m}$ . Sputtering was planned as a metallization method to ensure conformity as well as to avoid open circuit among the interconnecting lines. Aside from providing interconnects to the devices themselves, the metallization layer occupy a major part of the device, including the center and the circumference of the chip. Most of this metal layer that encompasses a large area of the chip is meant to ensure that the substrate is properly grounded. The arrangement of the devices is meant to provide symmetrical interconnect lines between each of the devices and the contact pads. The contact pads themselves are square-shaped with  $250 \mu\text{m} \times 250 \mu\text{m}$  size, to accommodate the gold wire bonding that requires a minimum area of  $200 \times 200 \mu\text{m}$  to ensure good electrical contact.

The active devices were configured in pairs to facilitate compensated capacitance measurement, the detail of which is explained in Chapter 3. In general, this measurement scheme combines 2 driving AC signals with opposite phases at 2 capacitors with identical capacitance value to eliminate the parasitic effect. This arrangement enables one of the devices in a pair to be used as a compensating capacitor, since they share the same geometry and capacitance value. The active devices are arranged within a  $1 \times 1 \text{ cm}^2$  chip, and 36 acceptor chips are created on a 100 mm silicon wafer.

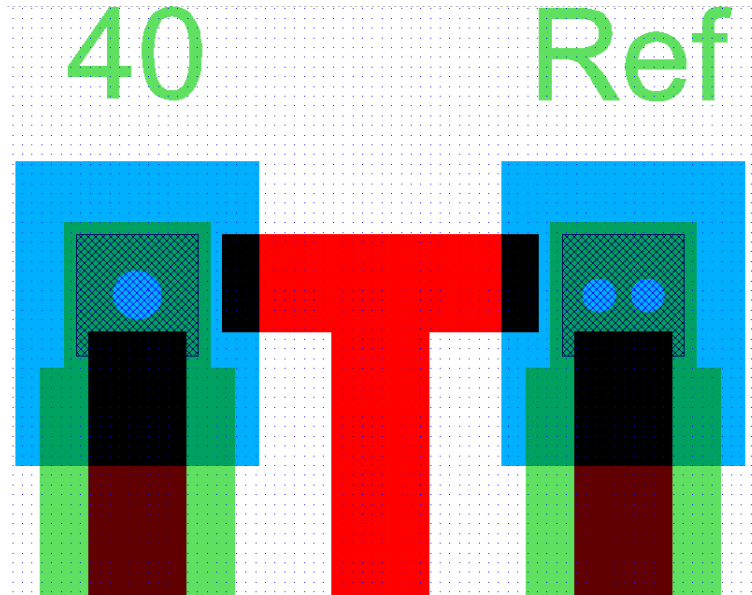


Figure 2.11. The schematics of the active device. Green indicates the PECVD SiO<sub>2</sub> layer (200 nm thick), which acts as the base structure. Blue indicates the Si device layer (2 μm thick, P<sup>++</sup>), which acts as the bottom electrode. Crisscrossed squares indicate the Si inks (0.34 μm thick, P<sup>++</sup>), which acts as the top electrode. White background indicates the buried SiO<sub>2</sub> layer (1 μm thick).

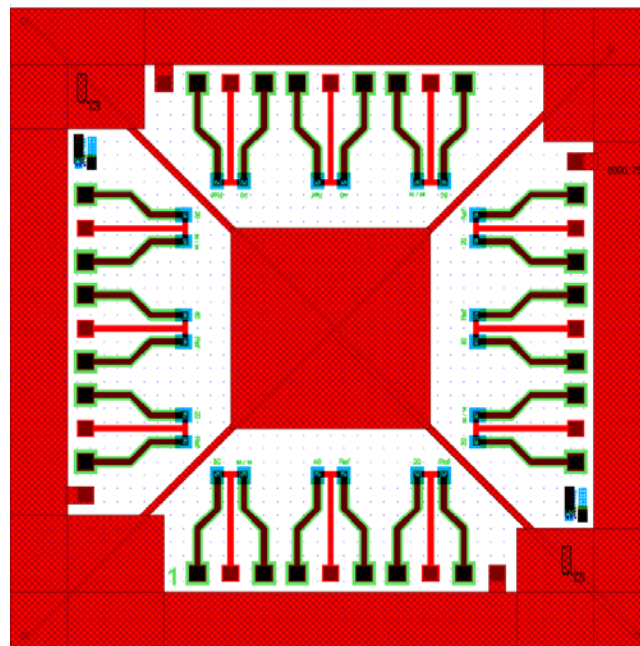


Figure 2.12. Chip layout for the fabrication of the active devices. Red color refers to the metallization layer, green color refers to the oxide layer, and the blue color refers to the highly-doped silicon layer, which acts as the devices' bottom electrode.

The fabrication process of the active device is illustrated in Figure 2.13. The process itself is very similar to the one used for the fabrication of passive structures, with an important difference regarding the substrates. Two silicon-on-insulator (SOI) wafers were used as starting substrates to fabricate our devices: a first one 0.34/1/500  $\mu\text{m}$  thick P-type (from BT electronics) was used as a donor wafer, while another 2/1/500  $\mu\text{m}$ , P++-type (from BT electronics) was used as an acceptor wafer. The donor SOI wafer was further doped with boron at a high dose of  $10^6$  atoms/ $\text{cm}^2$ , followed by thermal annealing at  $1000^\circ\text{C}$  during 20 minutes in order to reduce the electrical resistance of the top layer. Low resistance top layers for both donor and acceptor wafers were necessary to use the silicon layer directly as top and bottom electrodes of the device. The nanoplate inks were then fabricated from the donor wafer similar as for the passive device.

The acceptor chips were fabricated from the acceptor wafer as follows. First, a 200 nm thick PECVD oxide layer was deposited at  $300^\circ\text{C}$  and 1 mbar on top of the SOI acceptor wafer. Then, the base structure was patterned using photolithography followed by RIE (operated at room temperature and  $7 \cdot 10^{-3}$  mbar). The base structures consisted of square shapes (120  $\mu\text{m}$  side lengths) with one or more circular cavities. Another lithography step followed by RIE was done to separate the bottom electrodes below each base structure in order to electrically address them separately. Another lithography step followed by RIE is done to etch the buried oxide layer and make a via-hole to make a grounding contact with the bulk silicon layer. Finally, and prior to the transfer-printing of the ink onto the base structure, the receiver wafer was diced into  $1 \text{ cm} \times 1 \text{ cm}$  chips.

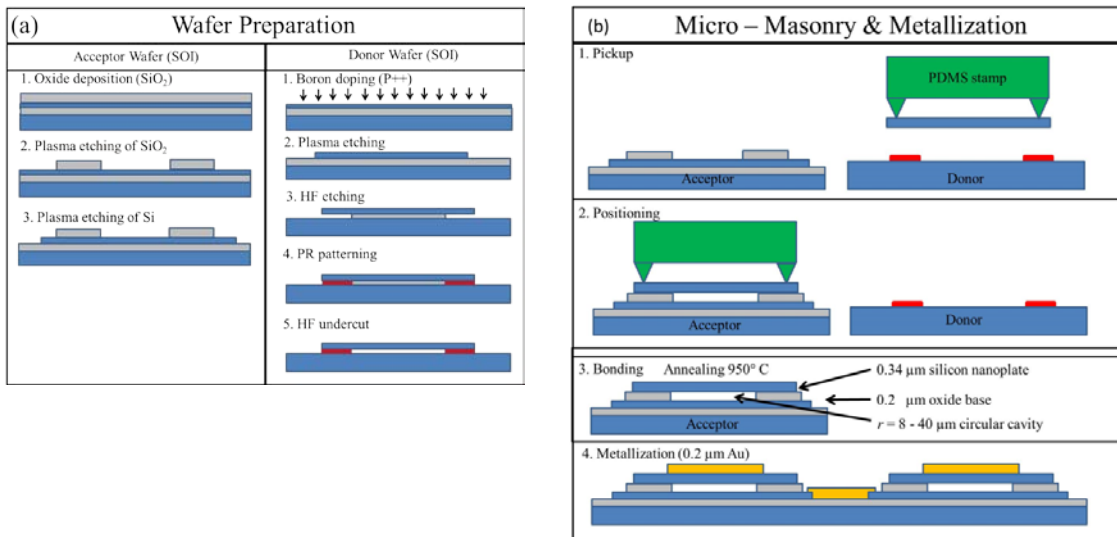


Figure 2.13. Fabrication process involving (a) the preparation of both donor and acceptor substrates and (b) the micro-masonry process to transfer and bond the nanoplates onto the base structures followed by metallization process to create interconnect lines.

Transfer-printing of the silicon nanoplate inks was done in a fashion similar to the one carried out for the passive structures, with some modifications in an attempt to increase the bonding quality and device yield. After the transfer printing process, the plate was pressed along the circumference of the cavity to ensure good contact using a single tip stamp. The chip was finally annealed at 600 °C to permanently bond the base and the membrane. As stated previously, the micro-masonry step was done at Seok Kim's Lab at University of Illinois at Urbana, Champaign, USA. Afterwards, the combined structures underwent metallization with Cr and Au (50 nm Cr + 200 nm Au) using sputtering technique. After the metallization step, both the gold patch and the interconnect lines were patterned by lift-off at the single chip level. For packaging purposes, each chip was wire bonded using Au wire and mounted onto a PCB. The PCB itself has 10 contact pads on each side, to connect the 3 pairs of devices plus the ground line of the chip.

### **2.3 Summary**

In this chapter, the theoretical basis of mechanical vibration has been presented, with a particular focus on forced vibration. Q factor was presented as the common measurement of dissipation on MEMS resonators, along with some damping mechanisms commonly encountered. Among all of the damping mechanisms, two of them, molecular damping and squeeze film damping, were explored further due to their relevance to this study. The design of the devices used in this study was presented along with the objectives of the design used. Finally, the fabrication method used to produce both passive structures and active devices was discussed.

## References

- [1] O Brand, I Dufour, S Heinrich, F Josse 2015 *Resonant MEMS: Fundamentals, Implementation, and Application* (Weinheim: Wiley-VCH)
- [2] M Spiegel and L Stephens 1998 *Schaum's Outline of Statistics* (New York: McGraw-Hill)
- [3] Lifshitz R and Roukes M L 2000 Thermoelastic damping in micro- and nanomechanical systems *Phys. Rev. B* **61** 5600–9
- [4] Nayfeh A H and Younis M I 2004 Modeling and simulations of thermoelastic damping in microplates *Journal of Micromechanics and Microengineering* **14** 1711–7
- [5] Duwel A, Gorman J, Weinstein M, Borenstein J and Ward P 2003 Experimental study of thermoelastic damping in MEMS gyros *Sensors and Actuators A: Physical* **103** 70–5
- [6] Park Y-H and Park K C 2004 High-fidelity modeling of MEMS resonators. Part I. Anchor loss mechanisms through substrate *Journal of Microelectromechanical Systems* **13** 238–47
- [7] Cole G D, Wilson-Rae I, Werbach K, Vanner M R and Aspelmeyer M 2011 Phonon-tunnelling dissipation in mechanical resonators *Nat Commun* **2** 231
- [8] Ekinici K L and Roukes M L 2005 Nanoelectromechanical systems *Review of Scientific Instruments* **76** 061101
- [9] Cho Y-H, Pisano A P and Howe R T 1994 Viscous damping model for laterally oscillating microstructures *Journal of Microelectromechanical Systems* **3** 81–7
- [10] Ergincan O, Palasantzas G and Kooi B J 2012 Viscous damping of microcantilevers with modified surfaces and geometries *Applied Physics Letters* **101** 061908
- [11] Homentcovschi D and Miles R N 2004 Modeling of viscous damping of perforated planar microstructures. Applications in acoustics *The Journal of the Acoustical Society of America* **116** 2939–47
- [12] Cho Y-H, Kwak B M, Pisano A P and Howe R T 1993 Viscous energy dissipation in laterally oscillating planar microstructures: a theoretical and experimental study *Micro Electro Mechanical Systems, 1993, MEMS '93, Proceedings An Investigation of Micro Structures, Sensors, Actuators, Machines and Systems. IEEE.* pp 93–8
- [13] Zhang X and Tang W C 1994 Viscous air damping in laterally driven microresonators *IEEE Workshop on Micro Electro Mechanical Systems, 1994*, pp 199–204
- [14] Berli C L A and Cardona A 2009 On the calculation of viscous damping of microbeam resonators in air *Journal of Sound and Vibration* **327** 249–53
- [15] Yang Y-J, Kamon M, Rabinovich V L, Ghaddar C, Deshpande M, Greiner K and Gilbert J R 2001 Modeling gas damping and spring phenomena in MEMS with frequency dependent macro-models *The 14th IEEE International Conference on Micro Electro Mechanical Systems, 2001. MEMS 2001* pp 365–8
- [16] Martin M J, Houston B H, Baldwin J W and Zalalutdinov M K 2008 Damping Models for Microcantilevers, Bridges, and Torsional Resonators in the Free-Molecular-Flow Regime *Journal of Microelectromechanical Systems* **17** 503–11

- [17] Frangi A, Ghisi A and Coronato L 2009 On a deterministic approach for the evaluation of gas damping in inertial MEMS in the free-molecule regime *Sensors and Actuators A: Physical* **149** 21–8
- [18] Bao M, Yang H, Yin H and Sun Y 2002 Energy transfer model for squeeze-film air damping in low vacuum *Journal of Micromechanics and Microengineering* **12** 341
- [19] Houlihan R and Kraft M 2005 Modelling squeeze film effects in a MEMS accelerometer with a levitated proof mass *Journal of Micromechanics and Microengineering* **15** 893–902
- [20] Zhang C, Xu G and Jiang Q 2004 Characterization of the squeeze film damping effect on the quality factor of a microbeam resonator *Journal of Micromechanics and Microengineering* **14** 1302–6
- [21] Kim E-S, Cho Y-H and Kim M-U 1999 Effect of holes and edges on the squeeze film damping of perforated micromechanical structures *Twelfth IEEE International Conference on Micro Electro Mechanical Systems, 1999. MEMS '99* pp 296–301
- [22] Starr J B 1990 Squeeze-film damping in solid-state accelerometers , *IEEE Solid-State Sensor and Actuator Workshop, 1990. 4th Technical Digest* , pp 44–7
- [23] Griffin W S, Richardson H H and Yamanami S 1966 A Study of Fluid Squeeze-Film Damping *J. Basic Eng* **88** 451–6
- [24] Pan F, Kubby J, Peeters E, Tran A T and Mukherjee S 1998 Squeeze film damping effect on the dynamic response of a MEMS torsion mirror *Journal of Micromechanics and Microengineering* **8** 200–8
- [25] Bao M and Yang H 2007 Squeeze film air damping in MEMS *Sensors and Actuators A: Physical* **136** 3–27
- [26] Wang W, Jia J and Li J 2013 Slide film damping in microelectromechanical system devices *Proceedings of the Institution of Mechanical Engineers, Part N: Journal of Nanoengineering and Nanosystems* **227** 162–70
- [27] Ongkodjojo A and Tay F E H 2003 Slide film damping and squeeze film damping models considering gas rarefaction effects for mems devices *Int. J. Comp. Eng. Sci.* **04** 401–4
- [28] Schomburg W K 2011 *Introduction to Microsystem Design* vol 1 (Berlin, Heidelberg: Springer Berlin Heidelberg)
- [29] Timoshenko S and Woinowsky-Krieger S 1959 *Theory of plates and shells* (McGraw-Hill)



## Chapter 3

# Characterization and Measurement Methods

*This chapter focuses on the two characterization methods used in this study that are based on optical and electrical measurements. A general overview of both measurement methods will first be presented. Then, we will provide details on the Fabry-Perot interferometry setup used for optical detection and on the compensating capacitance method used for electrical sensing. Theoretical principles behind these measurement methods, such as light interferometry and electrical charge cancellation will be presented. Finally, every component of the experimental setups used during the course of this study, such as the vacuum chamber, the laser source and the optical elements, and the acquisition and electrical measurement cards will be discussed along with the protocols used for characterizing the samples.*

### 3.1 Overview of dynamic optical measurement systems

Optical measurement methods have inherent advantages that make them suitable for characterization of MEMS devices. First of all, optical measurements are carried out without physical contact, thus avoiding physical loads and interactions such as mass addition or force application from a mechanical probe. In addition, the light beam used for measurements can be easily pointed and focused tightly on a small structure, which means that a single measurement setup can easily and quickly be used to measure different passive structures located on the same samples. Finally, the high measurement precision that results from the interferometric configuration also allows to probe small size structures, and morphologies, movements, displacements or deformations typical of MEMS devices.

On the other hand, the physical components required in optical setups limit the usage of optical sensing solely to an external probing approach since it is hardly suited to integration on the MEMS chip itself. Optical elements such as precision lenses, dielectric mirrors, prisms, and laser sources, are large and fragile. These components are also expensive and require macroscopic associated elements, such as alignment stages, power supplies and optical tables. The operator using optical setups needs extensive training and experience in order to obtain the correct focus and to optimize the interference patterns. Thus, optical measurement techniques are perfectly suited for the high-precision characterization of MEMS samples but cannot be considered as integrated sensing schemes embedded in MEMS devices.

In the context of MEMS studies, optical measurement systems can be divided into those that measure static and dynamic properties of MEMS. Static measurement systems measure size and displacement of MEMS devices, and are primarily used for process control and characterization of quasi-static MEMS devices such as valves. Optical microscopy, ellipsometry [1], and white-light interferometry [2,3] techniques are some examples of static optical measurement systems. Dynamic measurement systems, on the other hand, measure dynamic characteristics of the device in the frequency domain such as mode shape, resonant frequency, and Q factor. Since our MEMS device operates in dynamic mode (mechanical resonator), dynamic optical measurement systems are of primary interest for our work. Here, we thus give a brief overview of some commonly used dynamic measurement systems and then focus on the one thoroughly used in this study.

#### 3.1.1 Strobe video microscopy

The principle of strobe video microscopy [4,5] is illustrated in Figure 3.1.a. A charge – coupled device CCD camera is used to image the MEMS sample, which is driven by an AC signal at a certain frequency. The driving signal is synchronized with a light emitting diode LED (the strobe), which illuminates the sample at a period that is a multiple of the period of the driving frequency. As a result, the CCD camera receives multiple images of the sample

during the entire time the camera shutter is open. These exposures contain the images of the device in the same position (and phase) during vibration, since the LED flashes when the device is driven at the same phase. This procedure is repeated for a second acquisition shot, with some phase difference / lag between the driving signal period and LED flash + camera exposure period. Alone, this method enables visualization of a resonator's mode. When combined with interferometry techniques, this approach results in moving fringes that contains information about the displacement of the resonator, which can be obtained both quantitatively and visually observed. Although the ability to visually observe the resonator's mode shape is very powerful, this technique is limited by the response time of the LED strobe, which limits the measurement bandwidth of this technique to few MHz.

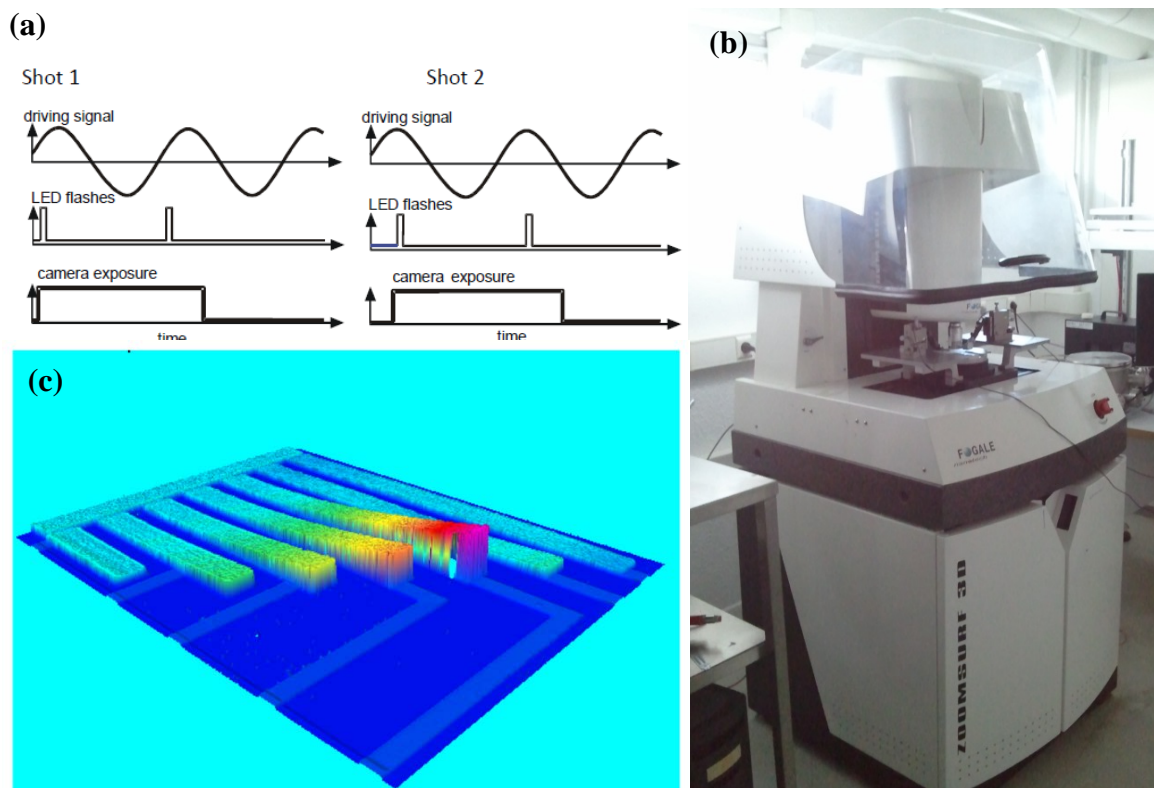


Figure 3.1. (a) Timing diagram for the strobe video microscopy. The LED is synchronized to flash at a multiple of the driving signal period next per shot, which contains information of the resonator displacement at a certain phase. Taken from [6]. (b) An example of a strobe video microscopy setup : ZoomSurf 3D from Fogale nanotech at LAAS. (c) An example of strobe video microscopy results for cantilevers. The different vibration amplitude at a certain frequency can be observed [7].

A typical commercial example of this setup is the ZoomSurf 3D from Fogale nanotech (Figure 3.1.b), which is available at LAAS. The system consist of an optical microscope with a field of view ranging from 7.2 to 80  $\mu\text{m}$ , a sample stage with piezo motor that can induce vertical displacements between 0.1 nm and 500  $\mu\text{m}$ , and measurement bandwidth between 100 Hz and 3 MHz using both white light and red light interferometry. Despite the interest of this technique to obtain valuable information on *e.g.* the mode shapes, this machine was not used in this study due to its limitation in measurement bandwidth.

### 3.1.2 Laser doppler vibrometry

The principle of laser doppler vibrometry [8] is illustrated in Figure 3.2.a. As can be observed, the setup for this measurement method is that of a Mach-Zender interferometer with some modifications. The light from the laser is split into two arms, one is directed to the MEMS device under test as a measurement beam, and the other one passes through a Bragg cell as a reference beam. The measurement beam that is reflected from the sample surface is modulated by the frequency of the resonator, while the reference beam experiences a Doppler shift defined by the Bragg cell frequency. When both beams combine at the photodiode, this optical heterodyne produces a beat frequency proportional to the actuation velocity of the surface of the MEMS device at the spot where the measurement beam is shined. Likewise, the modulation in phase is proportional to the MEMS displacement at the position of the measurement beam. The measurement bandwidth of this technique is higher than those of Strobe light microscopy, since the information is carried on by the frequency and does not depends on the illumination LED with relatively limited response time.

An example of a commercial laser doppler vibrometry setup for MEMS characterization is the MSA-500 by Politec (Figure 3.2.b). This equipment combines static white light interferometry, strobe-light interferometry, and laser Doppler vibrometry up to 24 MHz measurement bandwidth in one package. A unique feature of this equipment is its ability to do a raster scan of the sample, and thus obtain a 3D velocity and displacement profile of the device (Figure 3.2.c). Although ideal for MEMS characterization, we were not able to benefit from the advantages offer by this setup since it was unavailable at LAAS during the course of this study.

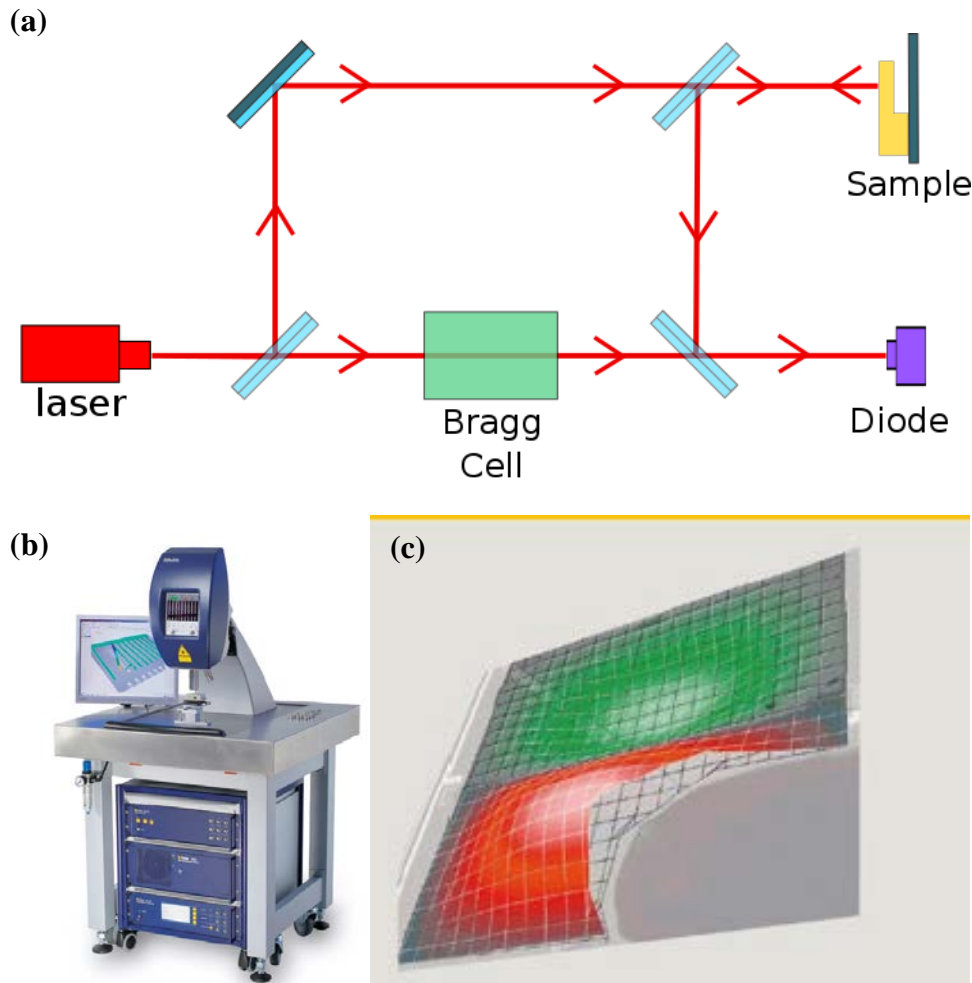


Figure 3.2. (a) Schematics of the laser doppler vibrometry setup. It has the configuration of a Mach-Zehnder interferometer, with the addition of a Bragg cell in the reference beam path. (b) An example of a commercial laser doppler vibrometry setup: MSA-500 by politec [9]. (c) An example of a laser doppler velocimetry results for the second mode of a rectangular plate. [9].

### 3.1.3 Fabry-Perot interferometry

The principle of Fabry-Perot interferometry [10] is illustrated in Figure 3.3.a. Unlike the setup used in laser Doppler vibrometry (Figure 3.2.a), the reference and measurement beam of the Fabry-Perot interferometer shares the same optical path with the exception of the gap between the sample and the base plate. Such interferometer is called a common-path interferometer [11], and has an advantage of simplicity and better stability compared to the double path interferometer used for laser Doppler velocimetry. The disadvantage of this setup is the

common path used for both reference and measurement beam prevents the use of Bragg cells to shift the frequency of the reference beam, and the information about the displacement of the resonator is not straightforward to obtain. This Fabry-Perot interferometry setup is the one used in this study, and its theoretical basis will be discussed in more detail hereafter.

Let us consider a laser beam with wavelength  $\lambda$ , speed of light  $c$  and angular frequency  $\omega_v = 2\pi c/\lambda$  that hits a vibrating resonator as shown in Figure 3.3.b. Part of the laser beam ( $A$ ) will be reflected by the resonator surface, and part of the beam ( $B$ ) will be transmitted through the resonating surface and reflected by the underlying substrate surface. The intensities  $I_A$  and  $I_B$  of  $A$  and  $B$  are not known as they depend strongly on the optical properties, thicknesses and surface quality of the resonator and substrate materials. The total intensity  $I_T$  detected on the photodiode used to collect the signals and caused by interference of  $A$  and  $B$  is:

$$I_T = I_A + I_B + 2\sqrt{I_A I_B} \cos(\beta \cos(\omega_{mems} t) + \varphi) \quad (3.1)$$

The phase shift between  $A$  and  $B$  is modulated by the mechanical vibration  $x$  of the resonator. The static part  $\varphi$  is caused by the gap between the resonator surface and underlying substrate. The dynamic part is caused by the mechanical vibration of the resonator, and has an amplitude of  $\beta = 4\pi x_{pk}/\lambda$ , with  $x_{pk}$  the mechanical vibration amplitude and  $\omega_{mems}$  the mechanical angular frequency.

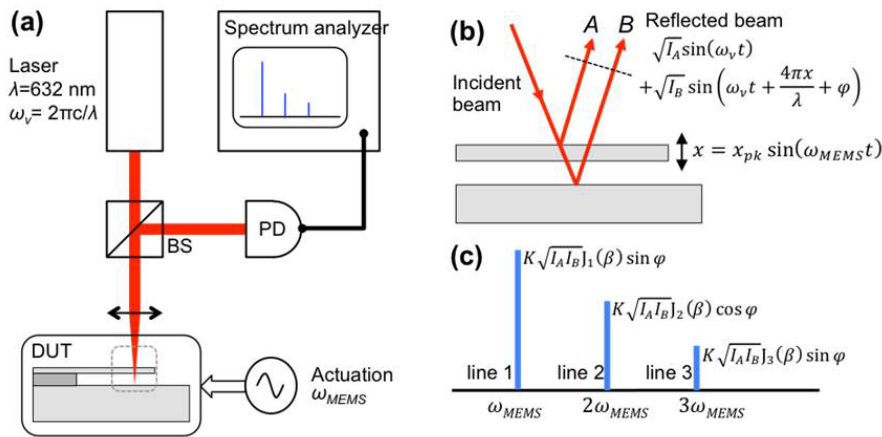


Figure 3.3. (a) Simplified view of the Fabry-Perot set-up. BS: beam splitter, PD: photodiode, DUT: device under test. (b) Detail of the signal reflected from the DUT. The optical signal is frequency modulated by the forced vibration of the MEMS resonator. (c) Spectral analysis of the PD signal. Magnitude of the harmonics is ruled by the Jacobi-Anger expansion of the PD signal.  $J_n$  denotes the  $n^{\text{th}}$  1<sup>st</sup> kind Bessel function.

It can be noted that the first two terms of Equation 3.1 represent the DC component of the photodiode current, while the third term represents the AC (mechanical frequency) modulated component of the photodiode current. Using trigonometric identity and Jacobi–Anger expansion, the time-varying component of the third term can be written as:

$$\begin{aligned}
 & \cos(\beta \cos(\omega_{mems}t)) \cos(\varphi) - \sin(\beta \cos(\omega_{mems}t)) \sin(\varphi) \\
 &= \cos(\varphi) \left[ J_0(\beta) + 2 \sum_{n=1}^{n=\infty} (-1)^n J_{2n}(\beta) \cos(2n \omega_{mems}t) \right] \\
 & \quad - \sin(\varphi) \left[ -2 \sum_{n=1}^{n=\infty} (-1)^n J_{2n-1}(\beta) \cos((2n-1) \omega_{mems}t) \right] \\
 &= \cos(\varphi) J_0(\beta) - 2 \sin(\varphi) J_1(\beta) \cos(\omega_{mems}t) - 2 \cos(\varphi) J_2(\beta) \cos(2\omega_{mems}t) + \\
 & \quad 2 \sin(\varphi) J_3(\beta) \cos(3\omega_{mems}t) + \dots \tag{3.2}
 \end{aligned}$$

with  $J_n$  as the  $n^{\text{th}}$  Bessel function [12] of the first kind. It can be observed that in the frequency domain, peaks appear at  $n$  times  $\omega_{mems}$ , with amplitude proportional to  $J_n$  and  $\sin(\varphi)$  for odd values of  $n$  or  $\cos(\varphi)$  for even values of  $n$  (Figure 3.3.c). Assuming the displacement is small compared to the light wavelength ( $\beta \ll 1$ ), as typical of MEMS devices, the following approximation for the Bessel function can be used:

$$J_1(\beta) \approx \frac{\beta}{2} \tag{3.3}$$

Substituting Equation 3.3 into Equation 3.2 and Equation 3.1 along with the definition of  $\beta$ , the first term of AC component of the light intensity  $I_{AC1}$  can be written as:

$$I_{AC1} = \frac{8\pi x_{pk}}{\lambda} \sqrt{I_A I_B} \sin(\varphi) \cos(\omega_{mems}t) \tag{3.4}$$

In other words, when a Fourier transform is done on the diode signal, such as using a spectrum / network analyzer, a peak at the mechanical resonant frequency  $\omega_{mems}$  which is proportional to the mechanical displacement amplitude  $x_{pk}$  can be observed. Note that although the reference light (B) is assumed to come from the reflection at the bottom of the device, this does not have to be the case. The light (B) could also come from reflection within the measurement setup or on the optical elements in the path to the diode, as long as it is stationary relative to the movement of the MEMS device.

### 3.2 Calibration of Fabry-Perot interferometer using thermal noise

A common way to calibrate a Fabry-Perot interferometer is by measuring the response of a device under thermal noise [13], which principle is discussed in this subchapter. The one-dimensional equation of motion for damped vibration can be expressed by:

$$\ddot{x} + \omega_n^2 x + \frac{\omega_n}{Q_n} \dot{x} = \frac{F(t)}{m_{eff}} \quad (3.5)$$

With  $x$  as the displacement of the resonator,  $\omega_n$  as the natural frequency of the resonator,  $Q_n$  as the quality factor of the resonator,  $F(t)$  as the driving force of the resonator, and  $m_{eff}$  as the effective mass of the resonator. This equation of motion can be taken into the frequency domain by doing a Fourier transform:

$$\frac{F\{x\}}{F\{F(t)\}} = \frac{1}{m_{eff}(\omega_n^2 - \omega^2 - \frac{i\omega\omega_n}{Q})} \quad (3.6)$$

The next step is to determine the relationship of average square amplitude  $\langle x(t)^2 \rangle$  with resonator power spectral density  $S_{device}$ . The average square amplitude is defined as:

$$\langle x(t)^2 \rangle = \frac{1}{T_0} \int_0^{T_0} x(t)^2 dt \quad (3.7)$$

with  $T_0$  as time which is large relative to the period of the vibration  $2\pi/\omega_n$ . Since potential energy of the resonator is proportional to  $x(t)^2$ , Equation 3.7 can be rewritten in terms of  $S_{device}$  in frequency domain as:

$$\langle x(t)^2 \rangle = \frac{1}{2\pi} \int_0^\infty S_{device} d\omega \quad (3.8)$$

The relation between resonator power spectral density  $S_{device}$  and driving force power spectral density  $S_{drive}$  is:

$$S_{device} = \left| \frac{F\{x\}}{F\{F(t)\}} \right|^2 S_{drive} \quad (3.9)$$

The ratio is squared for the same reason in Equation 3.8, due to the relation between displacement and power. In our case, the driving force is the thermal force, which power spectral density can be considered flat at the measurement range of interest ( $\omega_n \ll 1$  GHz). Thus, the  $S_{drive}$  in equation 9 can be considered constant. Substituting Equation 3.6 and Equation 3.9 into Equation 3.8 yields:

$$\langle x(t)^2 \rangle = \frac{S_{drive}}{2\pi m_{eff}^2} \int_0^\infty \frac{d\omega}{(\omega^2 - \omega_n^2)^2 + \left(\frac{\omega\omega_n}{Q}\right)^2} = \frac{S_{drive} Q}{4\omega_n^3 m_{eff}^2} \quad (3.10)$$

The next step is to find the connection between the average square amplitude and the absolute temperature. This can be found using the equipartition theorem, which for the one-dimensional resonator considered here can be written as:

$$\langle U \rangle = \frac{1}{2} m_{eff} \omega_n^2 \langle x(t)^2 \rangle = \frac{1}{2} K_b T \quad (3.11)$$

with  $K_b$  as the Boltmann's constant and  $T$  as the absolute temperature. Substituting Equation 3.11 into Equation 3.10 yields the expression of  $S_{drive}$  in terms of the resonator's effective parameters:

$$S_{drive} = \frac{4K_b T \omega_n m_{eff}}{Q} \quad (3.12)$$

and the resonator power spectral density  $S_{device}$  can be obtained by combining Equation 3.12 with Equation 3.9:

$$S_{device} = \frac{4K_b T \omega_n}{m_{eff} Q} \frac{1}{m_{eff} (\omega_n^2 - \omega^2 - \frac{i\omega\omega_n}{Q})} \quad (3.13)$$

which can be used to calibrate the measurement setup by comparison with the experimental power spectral density  $S_{exp}$  :

$$\alpha = \frac{S_{exp}}{S_{device}} \quad (3.14)$$

where  $\alpha$  is the transduction efficiency of the measurement setup. Note that measurement setup here refers to the specific combination of measurement point, sample, and equipment settings. Any change in the measurement conditions will change the value of  $\alpha$ .

### 3.3 Calibration of Fabry-Perot cavity using harmonics

During the course of this study, it was shown that the Fabry-Perot optical characterization method can be developed further to gain additional parameters regarding the device under test [14]. This is done by utilizing the extra AC terms in equation (2) ( $n = 2,3,4,\dots$ ), which were commonly neglected for normal Fabry-Perot characterization. It can be observed that in frequency domain, peaks appear at  $n$  times  $\omega_{mems}$ , with amplitude proportional to  $J_n$  and  $\sin(\varphi)$  for odd values of  $n$  or  $\cos(\varphi)$  for even values of  $n$  (Figure 3.3.c). Thus, the ratio between peak amplitudes  $L_n$  for  $n+2$  and  $n$  is independent of static phase shift  $\varphi$ , beam intensity, and optical losses. The peak amplitude ratio for  $n=3$  and  $n=1$  detected at the photodiode output, assuming that its gain  $K$  is constant over the frequency band, is:

$$\frac{L_3}{L_1} = \frac{2 \sin(\varphi) J_3(\beta)}{2 \sin(\varphi) J_1(\beta)} = \frac{J_3(\beta)}{J_1(\beta)} \quad (3.15)$$

Similar to Equation 3.3, the following approximations can be used for  $J_3$  in case of small  $\beta$ :

$$J_3(\beta) \approx \frac{\beta^3}{48} \quad (3.16)$$

Substituting Equation 3.3 and Equation 3.16 into Equation 3.15 yields:

$$\frac{L_3}{L_1} = \frac{J_3(\beta)}{J_1(\beta)} \approx \frac{2 \pi^2}{3 \lambda^2} x_{pk}^2 \quad (3.17)$$

which shows that the resonator displacement  $x_{pk}$  can be deduced from the measurement of the amplitude ratio between  $L_3$  and  $L_1$ . Since the value of  $L_1$  is proportional to  $x_{pk}$  (Figure 3.1.c and Equation 3.4), the calibration factor between the mechanical vibration amplitude of the micro-resonator and the signal magnitude at the spectrum analyzer is obtained. This calibration factor can be used to obtain the thermomechanical displacement noise spectral density  $x_{noise}$  at resonance from the signal noise spectral density  $L_{noise}$  at resonance:

$$\frac{L_1 \sqrt{2}}{x_{pk}} = \frac{L_{noise}}{x_{noise}} \quad (3.18)$$

The  $\sqrt{2}$  factor arises from the fact that  $x_{noise}$  is an RMS value while  $x_{pk}$  is a peak value. Effective mass  $M_{eff}$  and effective spring constant  $K_{eff}$  of the resonator are then obtained from  $x_{noise}$  by:

$$K_{eff} = \frac{4k_B T Q}{\omega_0 x_{noise}^2} \quad (3.19)$$

$$M_{eff} = \frac{4k_B T Q}{\omega_0^3 x_{noise}^2} \quad (3.20)$$

with  $k_B$  the Boltzmann's constant,  $T$  the absolute temperature,  $\omega_0$  the angular resonance frequency, and  $Q$  the quality factor. Note that these effective parameters correspond to the lumped description of the MEMS resonator at the location of the laser spot.

### 3.4 Overview of electrical measurement

The electrical measurement method displays almost opposite advantages and weaknesses compared to the optical measurement approach. As opposed to the bulky apparatuses associated to optical detection, the electrical measurement schemes can be implemented in a compact format and thus can be inherently integrated within the MEMS device itself. The

output signal is directly terms of current or voltage, which can be easily and economically processed.

On the other hand, the electrical measurement method in general has lower transduction efficiency than optical measurement techniques [15, 16], especially the ones based on interferometry. The noise [17] and parasitic effects [18] affecting electrical signals are also larger. These combined facts suggest that electrical measurement techniques are more suitable for integration within practical MEMS devices for sensing purposes instead of being used for structure characterization. Among the most dominant electrical sensing techniques implemented on MEMS devices are the piezoresistive [19], piezoelectric [20] and capacitive sensing techniques [21]. Since numerous reviews present all these techniques in details, we will solely focus here on the electrical sensing technique used in our device, namely the parallel-plate capacitive measurement.

### 3.4.1. Fundamentals of parallel-plate capacitive resonator

Assuming no fringe electric fields, the capacitance of a parallel-plate capacitor  $C$  depends on the gap between the two plates  $d_0$ , the capacitor area  $A$ , and the dielectric permittivity of the material  $\varepsilon$  between the two plates:

$$C = \frac{\varepsilon A}{d_0} \quad (3.21)$$

When a voltage bias  $V$  is applied between the two plates, the parallel-plate capacitor is then charged with the amount of charge  $Q$ :

$$Q = C V \quad (3.22)$$

The electrostatic force introduced between the plates is then:

$$F = \frac{\varepsilon A V^2}{2d_0^2} = \frac{V^2}{2} \frac{dc}{dx} \quad (3.23)$$

with  $x$  measured in the direction perpendicular to the plates, and parallel to gap length  $d_0$ . When a mechanical resonator consists of parallel-plate capacitor, it can be modelled as a one-dimensional harmonic damped oscillator with damping constant  $\gamma$  with electrostatic forces used as the driving force. Thus, assuming no other external forces, its equation of motion can be written as:

$$\begin{aligned} m_{eff} \ddot{x} + \gamma \dot{x} + k_{eff} x &= F \\ m_{eff} \ddot{x} + \gamma \dot{x} + k_{eff} x &= \frac{V^2}{2} \frac{dc}{dx} \end{aligned} \quad (3.24)$$

In practice, the capacitor device is biased with combined AC and DC voltages [22]. The DC voltage bias,  $V_{DC}$ , charges the device and brings it to its operating point. On top of  $V_{DC}$ , a time-varying small signal component,  $V_{AC}$ , is added. This causes the device to vibrate with the same frequency as the  $V_{AC}$ . Since this causes the gap between the two plates to change, it results in a variation of the capacitance and charge values. These variations are maximized at resonance, which happens at the natural frequency of the device and at which the amplitude of vibration of the structure is maximum. The time-varying induced charges are measured as an AC current that can be detected using *e.g.* a spectrum/network analyzer. A small signal model can be used by assuming that the plate displacement  $x$ , applied voltage  $V$ , induced charge  $Q$ , and applied force  $F$  consist of an equilibrium value plus a small varying (delta) component:

$$\begin{aligned} x &= dx + x_0 \\ V &= dV + V_0 \\ Q &= dQ + Q_0 \\ F &= dF + F_0 \end{aligned} \quad (3.25)$$

Linearizing Equation 3.22 around the operating point using Taylor expansion and substituting Equation 3.25, the incremental change of charge  $dQ$  becomes

$$dQ = V_0 \frac{dc}{dx} dx + CdV \quad (3.26)$$

and the incremental change of force  $dF$  becomes

$$dF = \frac{1}{2} V_0^2 \frac{d^2c}{dx^2} dx + V_0 \frac{dc}{dx} dV \quad (3.27)$$

The equation of motion for small signal is obtained by substituting Equation 3.27 into Equation 3.24:

$$m_{eff} d\ddot{x} + \gamma d\dot{x} + (k_{eff} - \frac{1}{2} V_0^2 \frac{d^2c}{dx^2}) dx = V_0 \frac{dc}{dx} dV \quad (3.28)$$

the Laplace transform of which is:

$$dX(S) = \frac{V_0 \frac{dc}{dx} dV(s)}{m_{eff} s^2 + b_x s + (k_{eff} - \frac{1}{2} V_0^2 \frac{d^2c}{dx^2})} \quad (3.29)$$

Two things can be noticed from Equation 3.29 : the first one is that the amplitude response of the resonator is proportional both to  $V_0$  and  $dV$ , which are the AC and DC voltage bias  $V_{AC}$  and  $V_{DC}$  applied to the device. The second one is that the  $dx$  term, which only contains the spring constant on unbiased device, becomes modified by an electrostatic term. This means that the apparent spring constant of the device is lowered, and, as a result, the resonant

frequency is lowered in a biased device. Intuitively, this can be understood as the electrostatic force opposing the restoring elastic force of the device, which becomes larger as  $V_{DC}$  is increased. Several work exist which treat this subject with more details, either incorporating tilting of the device [23] or taking into account the curvature of the surface on plate devices [24].

### 3.4.2 Compensated capacitive measurement technique

From a practical point of view, in order to carry out the capacitive measurement of a parallel-plate resonator, we can implement a compensated measurement scheme by using two devices. Figure 3.4 shows the equivalent circuit of a paired device (active and reference resonators), as well as the configuration of voltage bias at each port. The current flowing through device 1 (active device), represented by the parasitic capacitance  $C_p$  and the resonator capacitance  $C_1(t)$ , and driven by a combination of AC bias  $V_{ac1}$  and DC bias  $V_{dc1}$  is expressed by [23]

$$i_1(t) = \frac{d}{dt} [V_{ac1}(t) C_p + (V_{ac1}(t) + V_{dc1}) C_1(t)] \quad (3.30)$$

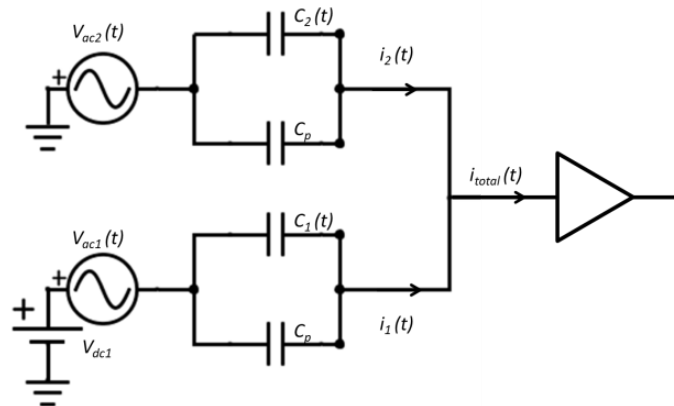


Figure 3.4. Schematics of the measurement scheme used for a paired device.

The second term of the equation with  $C_1(t)$  contains the information about the resonator movement, while the first term of the equation represents the parasitic effects of the oxide layer between the electrodes, the parasitic capacitance of the silicon and the metal interconnects. This parasitic term is orders of magnitude larger than the measurement signal (actually about 2 orders of magnitude for our fabricated device, presented in the previous Chapter), and must be properly removed before amplification. In this measurement scheme, compensation is achieved by driving device 2 using an AC voltage bias  $V_{ac2}$  of same magnitude of  $V_{ac1}$  but with an opposite phase:

$$V_{ac1}(t) = -V_{ac2}(t) \quad (3.31)$$

Devices 1 and 2 are geometrically symmetrical except for the number and size of the cavities, thus they have identical parasitic capacitance value  $C_p$ . Since devices 1 and 2 are designed with different resonant frequencies,  $C_2(t)$  can be considered constant with respect to time when  $C_1(t)$  is varying with time due to resonance, and vice versa (since the amplitude at resonance is much larger). Thus for compensating purpose, we can neglect the effect of  $C_2(t)$  which is much smaller than  $C_p$ , and the current flowing out of device 2 is:

$$i_2(t) = \frac{d}{dt} [-V_{ac1}(t) C_p - V_{ac1}(t) C_2(t)] \approx \frac{d}{dt} (-V_{ac1}(t) C_p) \quad (3.32)$$

And the total current,  $I_{total}$ , is:

$$I_{total}(t) = i_1 + i_2 = \frac{d}{dt} [V_{ac1} + V_{ac1}(t)] C_1(t) \quad (3.33)$$

This current can then be amplified using a charge amplifier and fed into a network analyzer.

### 3.5 Experimental setup and equipment

Detailed explanation on experimental setup and equipment can be found in the Annex A and B for optical and capacitive measurement respectively.

### 3.6 Summary

This chapter explores several aspects of the characterizations methods used in this study, which include theoretical background, equipment setup, and experimental protocols. Theoretical treatment was given regarding the Fabry-Perot interferometry, thermal noise of the MEMS resonator, determination of effective parameters, and capacitive actuation and sensing. Equipment setup descriptions include the vacuum measurement chamber, the optical measurement system, and the capacitive measurement card. Finally, experimental protocols regarding the operation of the vacuum chamber, startup of the measurement electronics and optical and capacitive characterization are described.

## References

- [1] Allen T H 1978 A Review Of Optical Property Measurements Using Ellipsometry *Proc. SPIE 0140, Optical Coatings: Applications and Utilization II* vol 0140 pp 42–51
- [2] O’Mahony C, Hill M, Brunet M, Duane R and Mathewson A 2003 Characterization of micromechanical structures using white-light interferometry *Meas. Sci. Technol.* **14** 1807
- [3] Jiang Y and Ding W 2010 Recent developments in fiber optic spectral white-light interferometry *Photonic Sens* **1** 62–71
- [4] Freeman D M and Davis C Q 1998 Using video microscopy to characterize micromechanical systems *Broadband Optical Networks and Technologies: An Emerging Reality/Optical MEMS/Smart Pixels/Organic Optics and Optoelectronics. 1998 IEEE/LEOS Summer Topical Meetings.* pp II/9–II10
- [5] Hemmert W, Mermelstein M S and Freeman D M 1999 Nanometer resolution of three-dimensional motions using video interference microscopy *Twelfth IEEE International Conference on Micro Electro Mechanical Systems, 1999. MEMS '99* pp 302–8
- [6] Lawrence L 2012 Optical Measurement Techniques for Dynamic Characterization of MEMS Devices *Politec MEMS Whitepaper Series*
- [7] Ballestra A, Somà A and Pavanello R 2008 Experimental-Numerical Comparison of the Cantilever MEMS Frequency Shift in presence of a Residual Stress Gradient *Sensors* **8** 767–83
- [8] Castellini P, Martarelli M and Tomasini E P 2006 Laser Doppler Vibrometry: Development of advanced solutions answering to technology’s needs *Mechanical Systems and Signal Processing* **20** 1265–85
- [9] Politec 2014 MSA – 500 Micro System Analyzer *Politec Product Information Brochure*
- [10] Vaughan M 1989 *The Fabry-Perot Interferometer: History, Theory, Practice and Applications* (CRC Press)
- [11] Vakhtin A B, Kane D J, Wood W R and Peterson K A 2003 Common-Path Interferometer for Frequency-Domain Optical Coherence Tomography *Applied Optics* **42** 6953
- [12] Korenev B G 2003 *Bessel Functions and Their Applications* (CRC Press)
- [13] Hauer B D, Doolin C, Beach K S D and Davis J P 2013 A general procedure for thermomechanical calibration of nano/micro-mechanical resonators *Annals of Physics* **339** 181–207
- [14] Bhaswara A, Dezest D, Nicu L, Leichle T, and Legrand B 2015 Determination of The Effective Mass and Stiffness of a Micro Resonator From a Single Optical Characterization *2015 Transducers Alaska The 18th International Conference on Solid-State Sensors, Actuators and Microsystems*) W2P.096
- [15] Jacobs-Cook A J 1996 MEMS versus MOMS from a systems point of view *J. Micromech. Microeng.* **6** 148
- [16] Bell D J, Lu T J, Fleck N A and Spearing S M 2005 MEMS actuators and sensors: observations on their performance and selection for purpose *J. Micromech. Microeng.* **15** S153

- [17] Mohd-Yasin F, Nagel D J and Korman C E 2010 Noise in MEMS *Meas. Sci. Technol.* **21** 012001
- [18] Yao J J 2000 RF MEMS from a device perspective *J. Micromech. Microeng.* **10** R9
- [19] Barlian A A, Park W-T, Mallon J R, Rastegar A J and Pruitt B L 2009 Review: Semiconductor Piezoresistance for Microsystems *Proc IEEE Inst Electr Electron Eng* **97** 513–52
- [20] Tadigadapa S and Mateti K 2009 Piezoelectric MEMS sensors: state-of-the-art and perspectives *Meas. Sci. Technol.* **20** 092001
- [21] Baxter L K 1996 *Capacitive Sensors: Design and Applications* (John Wiley & Sons)
- [22] J. Cao and C. T.-C. Nguyen 1999 Drive Amplitude Dependence of Micromechanical Resonator Series Motional Resistance Digest of Technical Papers, *10<sup>th</sup> International Conference on Solid-State Sensors and Actuators, Sendai, Japan* pp. 1826-1829.
- [23] Trusov A A and Shkel A M 2007 Capacitive detection in resonant MEMS with arbitrary amplitude of motion *J. Micromech. Microeng.* **17** 1583
- [24] Ahmad B and Pratap R 2010 Elasto-Electrostatic Analysis of Circular Microplates Used in Capacitive Micromachined Ultrasonic Transducers *IEEE Sensors Journal* **10** 1767–73

## Chapter 4

### Results and Discussion

*This chapter describes and discusses the measurement results that have been collected for our fabricated nanoplate resonators. The content of this chapter is organized into four subchapters. The first subchapter will discuss the various failure modes that have been observed in the course of the device fabrication process. The second subchapter will present the characterization results of passive structures using the Fabry-Perot setup, which include analysis on  $Q$  factors and resonant frequencies variation in vacuum and atmospheric pressure. The third subchapter will provide characterization results of active devices using both the optical and the electrical measurement methods. The fourth subchapter contains other results that do not fit directly into the first three subchapters, but nevertheless deemed relevant for the purpose of this study.*

#### **4.1. Failure modes in devices fabricated using the micro-masonry technique**

It is mandatory to know and understand the advantages, the weaknesses, and most importantly, the limitations of the various micro-fabrication methods in order to select the most appropriate ones when considering the realization of a MEMS device for a given application. In that regard, it is of primary interest to provide here an insight of the issues that we have encountered during the fabrication of our nanoplate resonators using micro-masonry. This discussion will point out the limitations of the micro-masonry technique for our specific application, i.e. the realization of suspended silicon structures. We will thus present the two failure modes that were identified for plate vibrating devices fabricated using micro-masonry, namely buckling and delamination of the plates. Importance of these failure modes will be illustrated by the fabrication yield of the various batches.

##### **4.1.1 Buckling of the nanoplate structures**

During the characterization of the first and second sample batches using the Fabry-Perot setup, it was observed that some of the devices did not exhibit any resonance peaks. Specifically, this happened to 16 out of 82 devices that had large cavity radius ( $r \geq 20 \mu\text{m}$ ). The first hypothesis to explain this experimental behavior was the possible stiction of the device to the substrate, as it is commonly observed in other MEMS devices [1]. However, imaging of the structures with a scanning electron microscope (SEM), as shown in Figure 4.1, revealed something different. Indeed, while some devices exhibited downward buckling (as shown in Figure 4.1.b), others were buckled upwards (as shown in Figure 4.1.a), which obviously could not be attributed to stiction. Still, no vibrations could be detected from both structures shown in Figure 4.1.a and 4.1.b. Working devices, on the other hand, always showed a smooth profile with no sign of deformation (Figure 4.1.c).

Our second hypothesis to explain the presence of buckling and lack of resonance was the thermal stress induced during the annealing process [2,3]. Since the base and the plate are made of different materials ( $\text{SiO}_2$  and Si respectively), they have different thermal expansion coefficients. During the plate/base thermal bonding step, this difference in thermal expansion causes stress to be introduced both into the plate and the base as the device cools down. In case of compressive stress, this results in buckling of the plate (in case of stress exceeding the critical stress value of the plate) or reduction of the plate resonant frequency (in case of stress not exceeding that critical stress value). We have tested our hypothesis by imaging a sample with a large circular opening ( $r = 30 \mu\text{m}$ ) before and after the thermal step at  $600 \text{ }^\circ\text{C}$  (see Figure 4.2.a and Figure 4.2.b, respectively). We have observed that after that step, the plate got buckled and stuck to the base in a circular form and we have thus concluded that the thermal anneal process caused the buckling in devices with large openings.

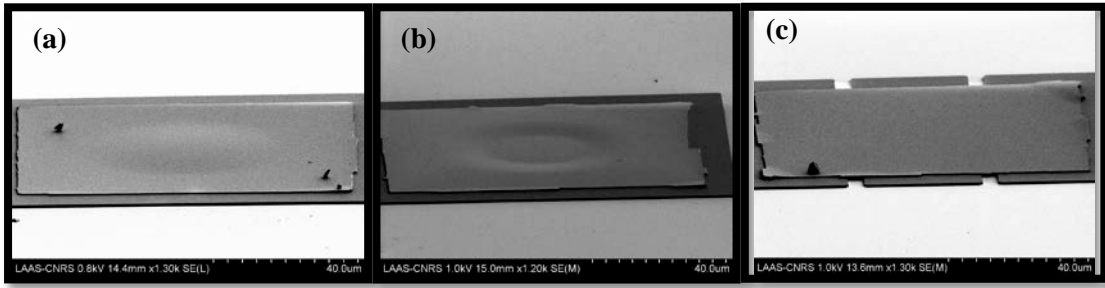


Figure 4.1. SEM images of passive structures that are (a) buckled up, (b) buckled down, (c) flat. The devices that buckle up and down do not exhibit any resonance peaks, unlike the devices with a flat profile.

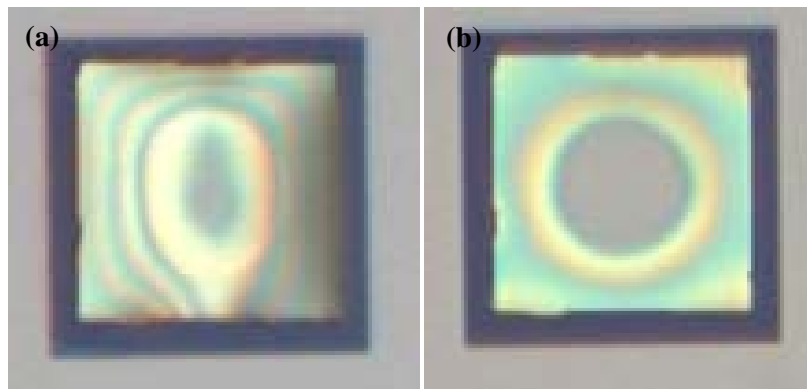


Figure 4.2. Optical microscopy images of a structure with circular cavity ( $r = 30 \mu\text{m}$ ) (a) before the thermal anneal process, and (b) after the thermal anneal process. The buckling is caused by the thermal compressive stress in the plates, which originates from the difference of thermal expansion coefficient between the Silicon plate and Silicon oxide base structure.

#### 4.1.2 Delamination of the nanoplate structures

Aside from buckling, another failure source was affecting the samples more severely. Starting with the second fabrication batch, we observed some samples with multiple unexpected peaks at frequencies that were very different from the ones analytically calculated (Figure 4.3.a). Since this was observed in vacuum conditions, this phenomenon could not be attributed to the spurious response of the piezo (described in the previous chapter). Also, we could detect vibration peaks even when the laser beam was shooting an area outside the cavities where the plate and base are supposed to be perfectly bonded (Figure 4.3.b), a behavior that was not observed on the first fabrication batch.

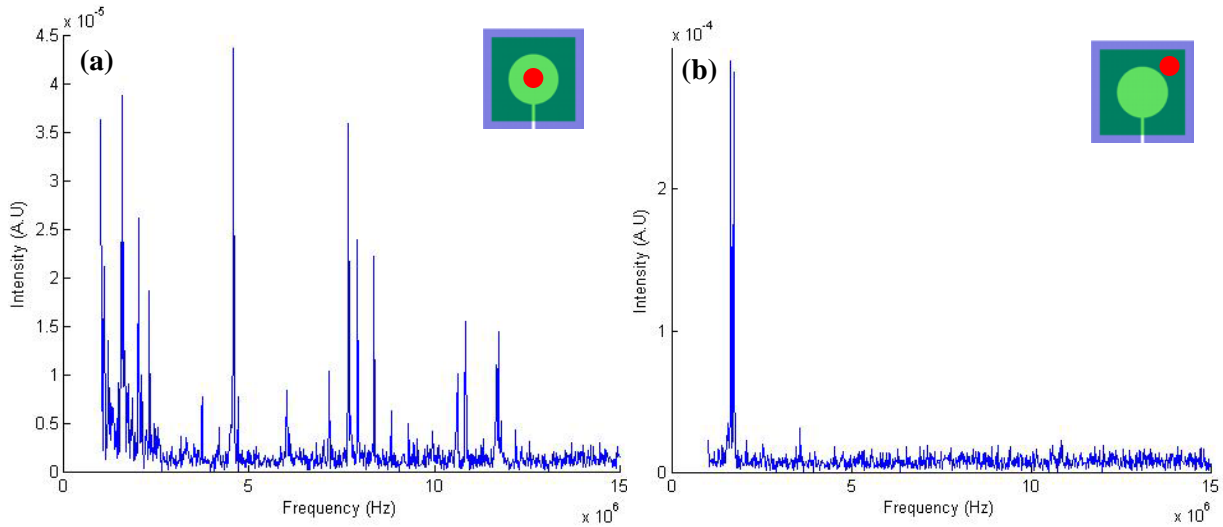
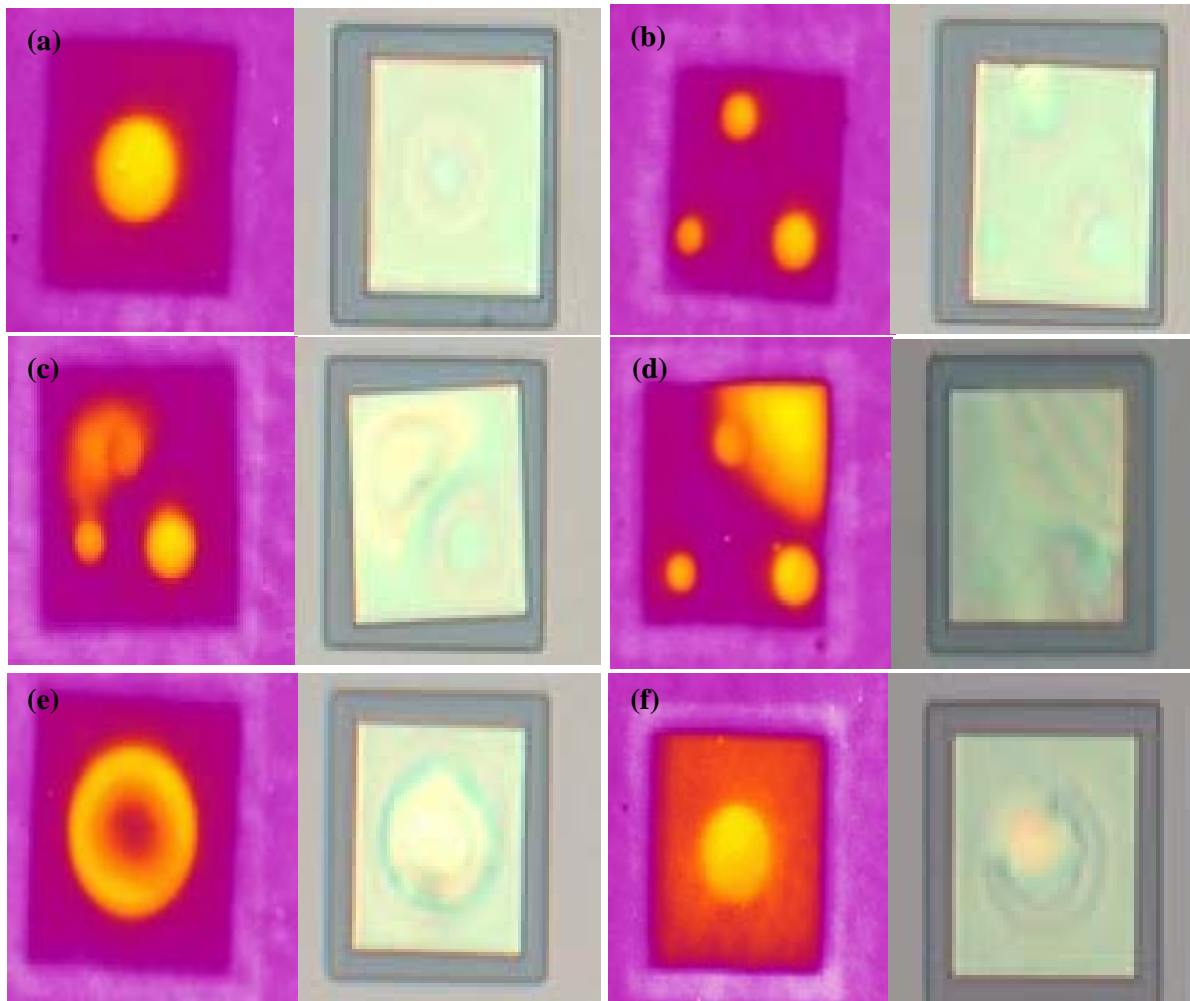


Figure 4.3. Measurement of a passive device (circular cavity,  $r = 30 \mu\text{m}$ ) in vacuum ( $P = 10^{-2}$  mbar) which showed (a) multiple vibration peaks at frequencies not predicted by the analytical calculations ( $f_{\text{analytical}} = 1.52 \text{ MHz}$ ) and (b) vibration peaks outside of the cavity, where none are normally expected. Inset is the illustration of the device, with the red circle marking the position of the laser spot during measurement.

To uncover the reason behind this problem, the samples were characterized using infrared imaging after completing the thermal annealing step. Since silicon is transparent to the infrared light, this technique enables the detection of bonding defects between the silicon plate and the silicon oxide base, which is difficult to do with visible light microscopy techniques. Figure 4.4.a and 4.4.b show infrared and optical images of passive structures with a single and multiple circular cavities that were working properly (*i.e.* showing lorentzian peak near the expected analytical resonant frequency  $f_{\text{analytical}}$ ). The dark purple rectangle represents an area where the silicon plate is bonded with the silicon oxide base, while the bright orange area represents the well-defined area of the cavity filled with air.



*Figure 4.4. Infrared (left) and optical (right) microscopy images of different defects that might affect the devices fabricated using the micro-masonry process. (a) Functional device with a single cavity. (b) Functional device with multiple cavities. (c) A defective multiple cavities device, with voids in between the cavities. (d) A defective multiple cavities device, with delamination on the edge of the plate. (e) A defective single cavity device that buckled. (f) A defective single cavity device with imperfect bonding between the plate and the base.*

On the other hand, Figure 4.4.c shows a device with air pockets or voids outside of the circular cavities. These voids are caused by the partial delamination between the plate and the base, similar to one observed during wafer bonding process [4], and is responsible for the unexpected frequency responses shown in Figure 4.3. This delamination can happen in the center of the plate, as shown in Figure 4.4.c, or on the edge of the plate, as shown in Figure 4.4.d. Aside from showing delamination spots between the plate and the base structure, the infrared microscopy technique can also be used to detect buckling of the plate, as shown in

Figure 4.4.e. The buckling of the structure is indicated by a purple area in the middle of the cavity (where the plate touches the base structure below it) that is surrounded by bright orange areas. Figure 4.4.f shows a flaw that is not apparent with other measurement methods: in this structure, light orange is present everywhere below the silicon plate, while the main device cavity is still visible. This indicates that the contact between the plate and the base is not perfect, resulting in weak bonding strength between the two. When measured with the Fabry-Perot interferometer, this device has a similar frequency response as properly bonded devices (such as those shown in Figure 4.4.a). However, it was recognized that this weak bonding strength might complicate post-processing and lead to device failure.

Subsequent testing of the bond strength by carrying out lithography processes and deposition of various materials on the samples proved this hypothesis. Figure 4.5.a shows an optical microscopy image of a sample with  $t = 1.3 \mu\text{m}$  plate thickness after the deposition of  $1.3 \mu\text{m}$  thick ECI resist and the subsequent resist removing with an acetone rinse. The detachment of the plate from the base for two of the structures can be clearly observed. Figure 4.5.b shows an optical microscopy image of a sample with  $0.34 \mu\text{m}$  plate thickness after the deposition of  $400 \text{ nm}$  silicon oxide using PECVD. Similar to Figure 4.5.a, the stress induced from the oxide layer deposited above the membrane has led to the full delamination of two devices. Note that on both Figures 4.5.a and 4.5.b we can clearly see structures that do not experience delamination on the same chip, underlining the large variation of bond strengths between fabricated devices. This issue, which was not observed in the first fabrication batch, has led to a drastic reduction of the fabrication yield. This issue was thus to be solved before starting the fabrication of the active device, which required several fabrication steps to be complete after the micro-masonry process.

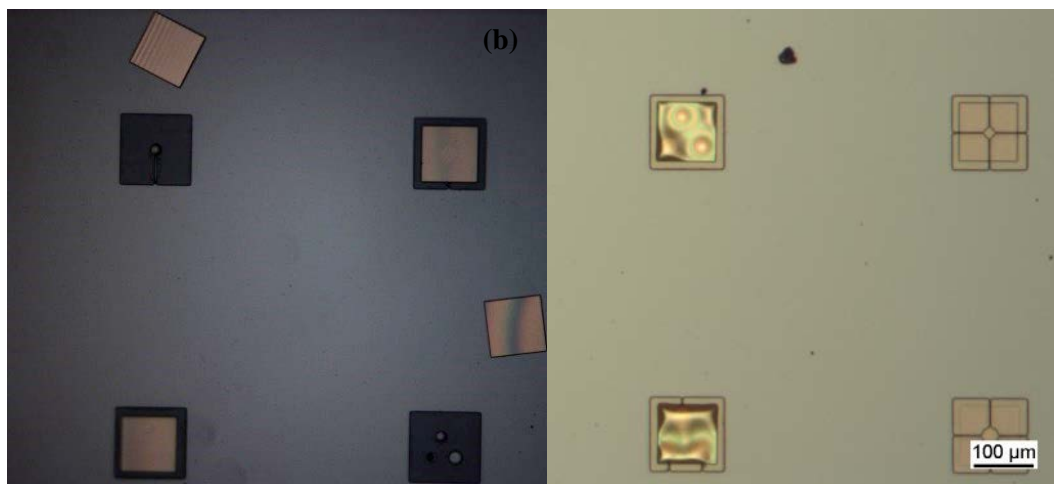
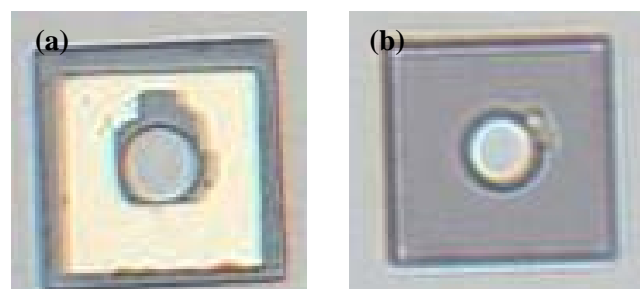


Figure 4.5. Optical microscopy images of delaminated plates after different post-processing steps. (a) Devices with  $1.3 \mu\text{m}$  thick membranes delaminating after  $1.3 \mu\text{m}$  ECI resist deposition and washing with acetone. (b) Devices with  $0.34 \mu\text{m}$  thick membranes delaminating after deposition of a  $400 \text{ nm}$  thick PECVD  $\text{SiO}_2$  layer.

We have tried various modifications in the micro-masonry process in order to improve the bonding strength such that the device would withstand the post-processing steps involved in the active device fabrication. To do this, samples containing passive structures were fabricated using modified micro-masonry techniques, and were exposed to treatments simulating a typical post-processing environment, as follows. After fabrication, the sample was rinsed in isopropyl alcohol (IPA), acetone, DI water, and IPA before drying it with N<sub>2</sub> gas to simulate specific tasks involved in photolithography. The samples were then put inside a vacuum chamber at  $P = 4 \times 10^{-6}$  mbar to simulate the conditions of metallization. Finally the sample was placed in an acetone bath with ultrasounds for 1 minute to simulate any mechanical disturbance that may occur during sample handling and lift-off processes. While it was found that the ultrasonic step breaks the plate above the cavity, the aim of this experiment was mainly to see whether the bond between the plate and the base structure could withstand the process. The results of each of the modification applied to the standard micro-masonry method are discussed further below.

Previous work has shown that bonding strength between silicon and silicon oxide can be increased by plasma treatment [5]. This approach was then tested by exposing the acceptor substrates to O<sub>2</sub> plasma for varying periods of time. Figure 4.6.a and 4.6.b show optical microscopy images of two samples that were respectively treated with O<sub>2</sub> plasma for 2 and 10 minutes. It can be observed that the structures that were treated for 10 minutes mostly did not delaminate, unlike the ones that were exposed to oxygen plasma for only 2 minutes. Thus, we can conclude that O<sub>2</sub> plasma treatment for 10 minutes before micro-masonry process improves the bonding strength between the plate and the base structure.



*Figure 4.6. Optical Microscopy image of two samples that have been exposed to plasma O<sub>2</sub> treatment before the micro-masonry process for a period of (a) 2 minutes and (b) 10 minutes. Delamination was minimal for the sample that received plasma treatment for 10 minutes.*

Another approach that was investigated was the reduction of the temperature and length of the thermal annealing step. The hypothesis behind this modification is that the thermal stress between the plate and the base is proportional to the temperature change experienced by the sample. Lowering the anneal temperature would reduce this stress and result in a better bond between the two. Figure 4.7.a and 4.7.b show both optical and infrared microscopy images of a sample annealed at 600 °C for 30 minutes and one at 900 °C for 60 minutes, respectively. The optical images were taken after the ultrasonic bath, while the infrared images were taken before this treatment. The optical images show little difference for both temperatures: the majority of the plate remains bonded to the base and some delamination can be seen on the sample sides. On the other hand, the infrared images demonstrate a significant difference in bonding quality between the two samples, indicating that the sample annealed at 600 °C for 30 minutes exhibits a better bond quality compared to the one annealed at 900 °C for 60 minutes. Although the cause is unclear, it is possible that this is related to the smaller temperature difference experienced by the structure as it cools down to room temperature. Thus, we can conclude that the quality of bond between the silicon plate and silicon oxide base can be improved by lowering the thermal anneal temperature and the process duration. Still, in both cases, the bond is strong enough to withstand post-processing.

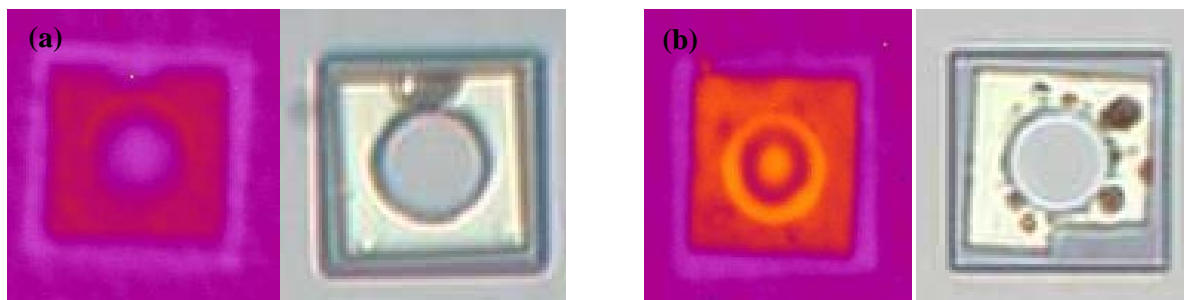


*Figure 4.7. Infrared (left) and optical (right) microscopy image of two samples which were annealed at (a) 600 °C for 30 min, and (b) 900 °C for 60 min. Both annealing temperatures and times produce samples with enough bond strength to withstand post-processing. However, the sample that was annealed at 600 °C for 30 minutes indicates a better bond quality in the infrared microscopy image.*

Some other modifications were attempted with somewhat mixed results. One approach was to keep the photoresist anchor on the top-side of the plate as a support in order to keep it flat and create better contact between the plate and the base; however, no notable bonding strength improvement was observed. Another approach was to press around the circumference of the structure with a single-tip stamp right after the transfer process and before the thermal annealing step, in an effort to ensure good contact between the plate and the membrane (Figure 4.8). Comparison between samples that underwent this process (3<sup>rd</sup> fabrication batch)

and the ones that did not (4<sup>th</sup> fabrication batch) showed an increase in delamination rate from 5.5% to 58.7%. However, a subsequent sample batch made using the same method (5<sup>th</sup> fabrication batch) yielded to a higher delamination rate (44.4%). Since this process was done manually, it is possible it could be operator dependent.



*Figure 4.8. Illustration of a method used to increase the contact quality between the plate and the base. After the micro-masonry process, the plate was pressed along the circumference of the cavity with a single-tip PDMS stamp. It was shown that although this method might reduce plate delamination, it is still dependent on the operator's skill.*

#### **4.1.3 Yield of the micro-masonry process**

The summary of the failure mechanisms and yields for all fabrication batches is summarized in Table 4.1. A structure or device is considered to be buckled if the plate is determined to be intact using optical microscopy and if no resonant peak is detected using the Fabry-Perot setup. A structure or device is determined to be delaminated if the plate is torn or peeled off during processing, or if multiple spurious peaks are detected on the plate. For devices or structures with multiple plates, the device is classified as delaminated if multiple spurious peaks are detected on one or more of the cavities. As such, the total number of cavities that showed good characteristics is higher than the yield shown in the Table 4.1. The data presented do not include samples with thick plates ( $t = 1.3 \mu\text{m}$ ), samples that were used for optimization of the process parameters (4 chips) along with samples that were damaged during delivery (1 chip).

*Table 4.1: Summary of yield information for all fabrication batches of this study, including passive structures and active devices*

<b>Batch no.</b>	<b>chips</b>	<b>plates/ chip</b>	<b>plates, total</b>	<b>delamination</b>	<b>buckling</b>	<b>total failures</b>	<b>yield</b>
1	4	16	64	0 (0%)	6 (9.3%)	6 (9.3 %)	58 (90.7 %)
2	5	16	80	55 (68.7%)	10 (12.5%)	65 (81.2 %)	15 (18.8 %)
3	5	6	30	17 (58.7%)	4 (13.3%)	21 (72 %)	9 (28 %)
4	3	6	18	1 (5.5 %)	3 (16.7%)	4 (22.2 %)	18 (77.8 %)
5	3	6	18	8 (44.4 %)	0 (0%)	8 (44.4 %)	10 (55.6 %)
<b>Total</b>	20		210	81 (38.6%)	23 (9.13 %)	104 (49.5 %)	106 (50.5 %)

The overall yield of the micro-masonry process involving the bonding of 210 plate-base structures is determined to be 50.5%. This figure is low compared to typical yield figure above 90% for MEMS [6] and wafer bonding techniques [7], although not unusual for newly developed processing techniques. Observation of the yield per processing batch showed that the first and fourth processing batch hold the highest yield (90.7% and 77.8% respectively), while the second and the third processing batch hold the lowest yield (18.8% and 28.8% respectively). It is notable that this difference of yield corresponds to a change in tool operator doing the micro-masonry procedure, with a first operator carrying out the 1<sup>st</sup>, 4<sup>th</sup>, and 5<sup>th</sup> batches and a second one taking care of the 2<sup>nd</sup> and 3<sup>rd</sup> batches. This strongly emphasizes the influence of tacit skills that an operator has on the yield. It shows that a skilled operator can possibly achieve a yield value comparable to other MEMS fabrication techniques. Closer look into the failure mode of the devices showed that delamination is more dominant compared to buckling. On average, device failure by delamination (38.6 %) is more than 4 times likely to happen than failure by buckling (9.13%). Thus, future work should focus on eliminating delamination, i.e. improving the plate/base bonding strength in the micro-masonry technique.

## 4.2 Measurement results for passive structures

In this subchapter, we present and discuss the measurement results of the passive structures issued from the first and second fabrication batches. We first focus on the measurement results of single cavities under vacuum, which provide information about the intrinsic Q factor of the device and, indirectly, about the plate internal stress from measurement of the resonant frequency  $f_0$ . We will first describe the measurement results and analysis for a representative device before presenting the results and analysis for a batch of devices. Next, we focus our discussion on the measurement results of single cavities under varying air pressures, including atmospheric pressure that is of interest for practical applications. Finally, we present the measurement results of passive structures with multiple cavities, both in air and in vacuum, with a specific focus on Q factor and stress variation and mechanical crosstalk between the cavities.

### 4.2.1 Characterization of single cavities in vacuum

The Fabry-Perot optical characterization of the first fabricated batch was done in vacuum conditions using piezo actuation. An example of the frequency response of a device ( $r = 10 \mu\text{m}$ , no air vents) at primary ( $P = 0.1 \text{ mbar}$ ) and secondary ( $P = 10^{-6} \text{ mbar}$ ) vacuum is shown in Figure 4.9.a and 4.9.b, respectively. A Lorentzian peak can be clearly observed around  $f_0 = 9.31 \text{ MHz}$ , which corresponds to the resonance of the device. The Q factor of the device was determined by curve fitting to be 13 793 and 14 062 in primary and secondary vacuums, respectively, which is not significantly different. This suggests that at both vacuum levels, the device operates in an intrinsic damping regime.

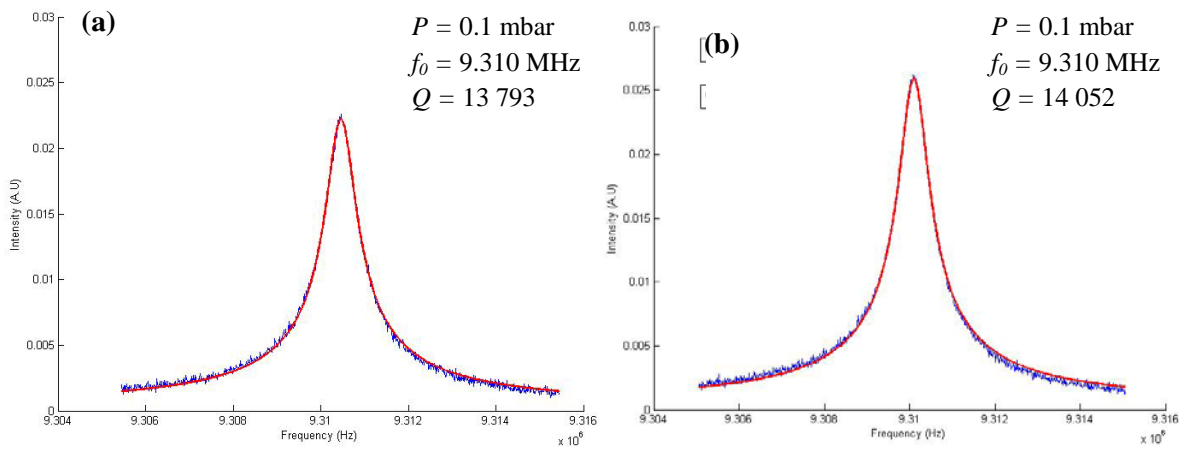


Figure 4.9. Frequency response optical measurement of a device with a single circular cavity of  $r = 10 \mu\text{m}$  in both (a) primary ( $P = 0.1 \text{ mbar}$ ) and (b) secondary ( $P = 10^{-6} \text{ mbar}$ ) vacuum. The Q factor exhibited in both pressure (around 14 000) is similar, which suggest that the device is operating in intrinsic damping regime at this vacuum level.

It was found that this high Q factor value, typically found in the first fabrication batch (Figure 4.9), was difficult to reproduce during subsequent fabrication batches. The frequency response that are more representative for a structure fabricated after the first batch ( $r = 20 \mu\text{m}$  radius,  $t = 0.34 \mu\text{m}$  plate thickness and  $h = 1.25 \mu\text{m}$  gap height) is shown in Figure 4.10. Thermomechanical actuation method was used to obtain this measurement data, due to the nonflat response of the piezo disc as described in chapter 3. Typical Q factor is here in the order of 3 000.

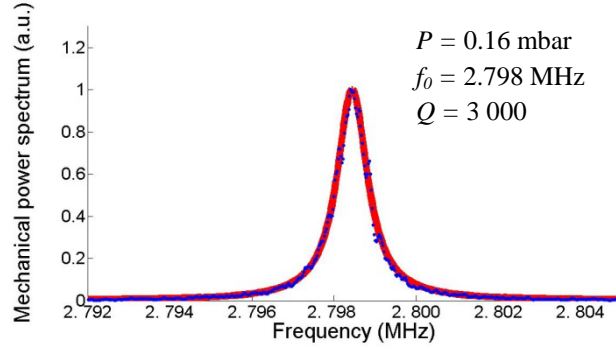


Figure 4.10. Vibrational noise spectra for a device with plate radius  $r = 20 \mu\text{m}$ , plate thickness  $t = 0.34 \mu\text{m}$ , and gap height  $h = 1.25 \mu\text{m}$ . in primary vacuum ( $P = 10^{-2}$  mbar), measured using only thermal noise.

The experimental resonant frequency  $f_0$  in vacuum is 2.798 MHz, which can be compared with the analytical resonant frequency  $f_{analytical}$  for a circular plate ideally clamped on the edges as derived in chapter 2, Equation 2.33 [8]:

$$f_{analytical} = \sqrt{\frac{5}{3}} \frac{1}{\pi r \sqrt{\rho}} \sqrt{\frac{4}{3} \frac{E}{1-\nu^2} \frac{t^2}{r^2} + \sigma_0} \quad (4.1)$$

with  $r$  = plate radius,  $t$  = plate thickness,  $\rho$  = density of material,  $\nu$  = Poisson's ratio,  $E$  = Young's modulus, and  $\sigma_0$  = in-plane stress in the plate. Substituting silicon mechanical properties for plate bending ( $E = 170$  GPa;  $\nu = 0.064$ ) and  $r = 20 \mu\text{m}$ ,  $t = 0.34 \mu\text{m}$  into Equation (4.1) yields  $f_{analytical}$  value of 3.455 MHz. It should be noted that equation (4.1) is valid for isotropic materials, while single-crystal silicon has different mechanical properties depending on its crystal orientation.

More accurate values of resonant frequencies were obtained by using anisotropic and orthotropic models in a finite element method (FEM) program. Implementation was done using COMSOL 3D modeling, using extra fine meshing for both models while the mechanical properties were taken from literature [9]. The resonant frequency obtained using these FEM models  $f_{FEM}$  is 3.261 MHz for the structure under consideration. Identical  $f_{FEM}$  value is obtained using both anisotropic and orthotropic model, assuming zero internal stress ( $\sigma_0 = 0$ ).

This discrepancy between experimental ( $f_0$ ) and theoretical ( $f_{analytical}$ ,  $f_{FEM}$ ) resonant frequency values led to the conclusion that the fabricated nanoplate displays some internal stress. The in-plane stress changes the resonant frequency, which is shifted to a higher frequency for tensile stress (+ sign) and lower frequency for compressive stress (- sign). Assuming the geometry and the material properties are known, the in-plane stress  $\sigma_0$  can be determined by the difference between  $f_0$  and  $f_{FEM}$ :

$$\sigma_0 = \frac{3\pi^2 r^2 \rho}{5} (f_{FEM}^2 - f_0^2) \quad (4.2)$$

Substituting  $f_0 = 2.798$  MHz (see Figure 4.9) and plate geometry in Equation (4.2) yields an in-plane stress of  $\sigma_0 = -15$  MPa.

The Fabry-Perot measurement results conducted in vacuum for the passive structures of the 2<sup>nd</sup> fabrication batch, along with the  $f_{analytical}$  assuming zero stress and perfect geometry, is presented in Table 4.2. The measured Q factor (which can be assumed as the intrinsic Q factor of the structure) is observed to vary widely between the devices, with the average value of 4 510, highest value of 9 080 and the lowest value of 1 433. No correlation was found between the measured Q factor and the radius of the cavity, the presence of air vents connecting the cavity and the environment, and the size of the gap below the plate. This fact indirectly implies that the seal between the plate and the base structure for this batch is not airtight, since the closed structure is thermally annealed under atmospheric pressure, and would result in lower Q factor when measured under vacuum environment due to air damping on one side of the plates; no such characteristic was observed. It can also be observed that for all passive structures, the measured resonant frequency is lower than the analytical value obtained by assuming perfect geometry and zero stress. While this implies the presence of compressive stress within the plates as shown in the example above, assuming the difference in all resonant frequencies is caused by stress leads to unlikely stress values. As an example, using Equation 4.2 for structure with  $r = 8 \mu\text{m}$  as shown in Table 4.2 yields a compressive stress value of  $\sigma_0 = -156$  MPa, which is about one order higher than the values observed for  $r = 20 \mu\text{m}$  ( $\sigma_0 = -15$  MPa). This is unlikely, and a more realistic assumption is to assume that difference in radius  $\Delta r$  between the ideal and fabricated structures plays also a significant role in the discrepancy between the theoretical and measured resonant frequency. As an assumption, it is reasonable to expect a positive value of  $\Delta r$  due to the imperfect clamping among the edge of the cavity.

Calculations of analytical resonant frequency using Equation 4.1 with different values of stress  $\sigma_0$  and variation in radius  $\Delta r$  is shown in Table 4.2. As can be observed, the analytical resonant frequency value assuming zero stress and no differences in radius is always larger than the experimental value. The effect of compressive stress and difference in radius depend on the radius of the cavity. For example, by adding a compressive stress of  $\sigma = -40$  MPa, the  $f_{analytical}$  of devices with  $r = 20 \mu\text{m}$  drops from 3.45 MHz to 2.16 MHz (37% decrease); in comparison, devices with  $r = 8 \mu\text{m}$  sees its  $f_{analytical}$  changing from 21.58 MHz to 20.50 MHz (5% decrease). Conversely, by adding a positive variation in radius of  $\Delta r = 1 \mu\text{m}$ , the  $f_{analytical}$  of devices with  $r = 20 \mu\text{m}$  changes from 3.45 MHz to 3.35 MHz (3% decrease); in comparison, devices with  $r = 8 \mu\text{m}$  changes its  $f_{analytical}$  from 21.58 MHz to 20.04 MHz (7% decrease). Thus, the increase of compressive stress mainly reduces the resonant frequency of devices with less structural rigidity (i.e. with larger cavity radius), while the variation in radius mainly affects the resonant frequency of devices with small radius.

Table 4.2.  $Q$  factor and resonant frequency measured in vacuum for functional passive structures of the 2<sup>nd</sup> fabrication batch, sorted by cavity size, the presence of air vents, and gap size.

$r$ ( $\mu\text{m}$ )	air vent	gap size ( $\mu\text{m}$ )	$Q_{\text{vacuum}}$	$f_{\text{experimental}}$ (MHz)	$f_{\text{analytical}}$ (MHz)
8	open	1.2	3031	17,048	21,52
10	closed	2.5	4805	11,11	13,77
	closed	2.5	2250	11,24	
	closed	1.2	3629	10,20	
	open	1.2	7279	10,91	
	closed	1.2	7199	11,24	
	open	1.2	5303	10,93	
	closed	2.5	1463	11,06	
	open	1.2	6259	10,95	
	open	1.2	3500	10,06	
	open	1.2	2961	10,73	
	open	0.66	1742	8,49	
	open	0.66	7199	11,69	
12	closed	1.2	6027	7,91	9,56
	open	0.66	3361	7,77	
	open	0.66	6227	7,78	
15	closed	2.5	6147	4,99	6,12
	open	2.5	9080	4,82	
	closed	2.5	6147	4,99	
	open	2.5	9080	4,82	
	open	1.2	6752	4,43	
	closed	1.2	2110	4,22	
	open	1.2	5464	4,44	
	open	1.2	2507	3,44	
	open	0.66	5592	4,19	
	closed	0.66	4818	4,81	
18	closed	0.66	3741	3,04	4,25
	open	0.66	1433	2,41	
20	closed	1.2	1672	2,29	3,44
	closed	2.5	2610	1,63	
	closed	0.66	3194	2,19	
	open	0.66	1746	2,01	

By trial and error, the  $f_{analytical}$  given by stress value of  $\sigma = 36.7$  MPa and  $\Delta r = 0.73$   $\mu\text{m}$  fits the average  $f_{experimental}$  value relatively well, and can be taken as the average stress and increase in radius for this fabrication batch. As stated before, this might result from imperfection of clamping among the edge of the cavity, or imperfection of etching process, creating a slightly larger diameter cavity than designed. However, it should be noted that this is an averaged value and individual structures have different stress and differences of radius due to process variation.

Table 4.3. Analytical resonant frequency calculated for different stress values and variation of radius.

$r$ ( $\mu\text{m}$ )	$f_{analytical}$ (MHz)					$f_{experimental}$ (MHz) (mean value)
	$\sigma = 0$ $\Delta r = 0$	$\sigma = 0$ $\Delta r = +1$ $\mu\text{m}$	$\sigma = -40$ MPa $\Delta r = 0$ $\mu\text{m}$	$\sigma = -40$ MPa $\Delta r = +1$ $\mu\text{m}$	$\sigma = -36.7$ MPa $\Delta r = +0.73$ $\mu\text{m}$	
8	21,58	20,04	20,50	15,96	17,05	17,048
10	13,81	13,02	12,72	10,31	10,94	10,723
12	9,59	9,13	8,48	7,04	7,47	7,822
15	6,14	5,90	4,98	4,22	4,50	4,5184
18	4,26	4,12	3,04	2,57	2,80	2,7295
20	3,45	3,35	2,16	1,80	2,03	2,03625

Equation 4.1 also shows that at a given critical compressive stress  $\sigma_{crit}$ , the plate buckles and its resonant frequency drops to zero. Rearranging the terms gives us the maximum radius  $r_{max}$  for a given plate thickness which can be fabricated without experiencing buckling:

$$r_{max} = \sqrt{\left(\frac{4}{3} \frac{E}{1-\nu^2} \frac{t^2}{(-\sigma_{crit})}\right)} \quad (4.3)$$

Putting in  $t = 0.34$   $\mu\text{m}$  and  $\sigma_{crit} = -36.7$  MPa into Equation (4.3) leads to a value of  $r = 26.8$   $\mu\text{m}$ . While this limits our fabrication technique in fabricating large and thin plate resonators, strain control techniques [10,11] might be explored in future studies to counterbalance the stress induced by micro-masonry. It should also be noted that the stress value used for  $\sigma_{crit}$  is the average value, and thus devices fabricated with  $r = 26.8$   $\mu\text{m}$  will have a yield of around 50% assuming only buckling as the failure mode.

A review of works related to mechanical resonators revealed that it is common to refer to resonators that are clamped all around their vibrating element as a “membranes” [12-18].

Other works, however, make a distinction between “plate” and “membrane” type structures, or between “thick plates” and “thin plates” [8,19]. The distinction between plates and membranes lies on the dominant origin of the restoring force of the resonator. In a plate, the bending moment of the resonator is the dominant origin of the restoring force; while in a membrane, the internal tensile stress of the resonator is the dominant origin of the restoring force.

In terms of resonant frequency, the difference between the two can be observed by evaluating equation 4.1, which has two terms inside the square root. The first term corresponds to the bending moment of the resonator, while the second term corresponds to the stress within the resonator. The resonator can be considered as a plate when the first term dominates over the second one and as a membrane when the second term dominates over the first one. This implies that for a circular structure, the resonant frequency of a membrane is proportional to  $1/r$  while the resonant frequency of a circular plate is proportional to  $1/r^2$ . The devices fabricated during the course of this study can be considered to be a plate and not a membrane for several reasons. Firstly, it has been observed that the device can still operate while experiencing compressive stress, which is only possible with plates and not membranes. Secondly, the variation of resonant frequency with cavity radius corresponds closely to the plate model rather than the membrane model. The measured resonant frequencies of the devices given in Table 4.1 as a function of  $1/r$  and  $1/r^2$  are respectively plotted in Figure 4.11 .a and 4.11.b, with the lines indicating the linear regression fit using the least-square method. It can be observed that the linear fitting line intercepts the origin for the  $1/r^2$  plot, unlike the one from the  $1/r$  plot. Thus, it is more appropriate to consider resonators fabricated in this study as a “plate” or “thick plates” instead of “thin plates” or “membranes”.

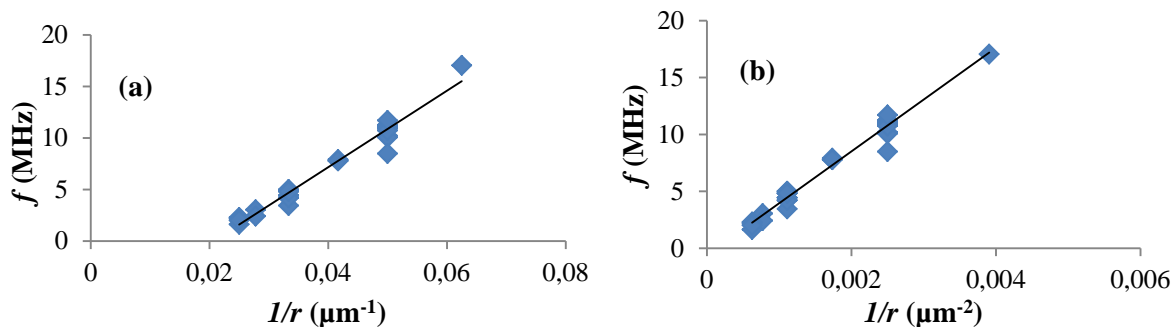


Figure 4.11. Plot of measured resonant frequency of devices with  $t = 0.34 \mu\text{m}$  from the second fabrication batch vs. (a)  $1/r$  and (b)  $1/r^2$ . The black line represents a least-square linear fit of the data points. It can be observed that the linear fit of resonant frequency vs  $1/r^2$  plot intersects at the origin, and the devices are better modeled as a plate compared to a membrane.

### 4.2.2 Characterization of single cavities in varying air pressure

Estimated values of the quality factor of the fabricated nanoplates were then used to study the damping mechanisms related to energy losses in the resonator. Air damping has a large impact on device performances such as mass sensitivity, and is an important consideration for designing mass sensors. This is more so considering practical applications of plate resonators often requiring them to operate under atmospheric pressure, or even liquid. While frequency response measurement in vacuum is straightforward, the measurement using piezo disc actuation in atmospheric pressure proves to be more difficult to interpret. Figure 4.12 shows a typical measurement result of a device ( $r = 15 \mu\text{m}$ , open cavity) in both primary vacuum (Figure 4.12.a,  $P = 0.1 \text{ mbar}$ ) and atmospheric pressure (Figure 4.12.b,  $P = 1 \text{ 012 mbar}$ ). While the measurement in primary vacuum produces the typical result as previously presented, the one in atmospheric pressure consists of multiple peaks, which are indistinct and in general do not exhibit a lorentzian behavior. The presence of these multiple peaks was observed in general when the devices were actuated using the piezo disc in atmospheric pressure, and renders the determination of Q factor difficult. Fitting of some of the peaks was attempted, but it was then difficult to determine which peak was representative of the device's own resonance (or if even there was any).

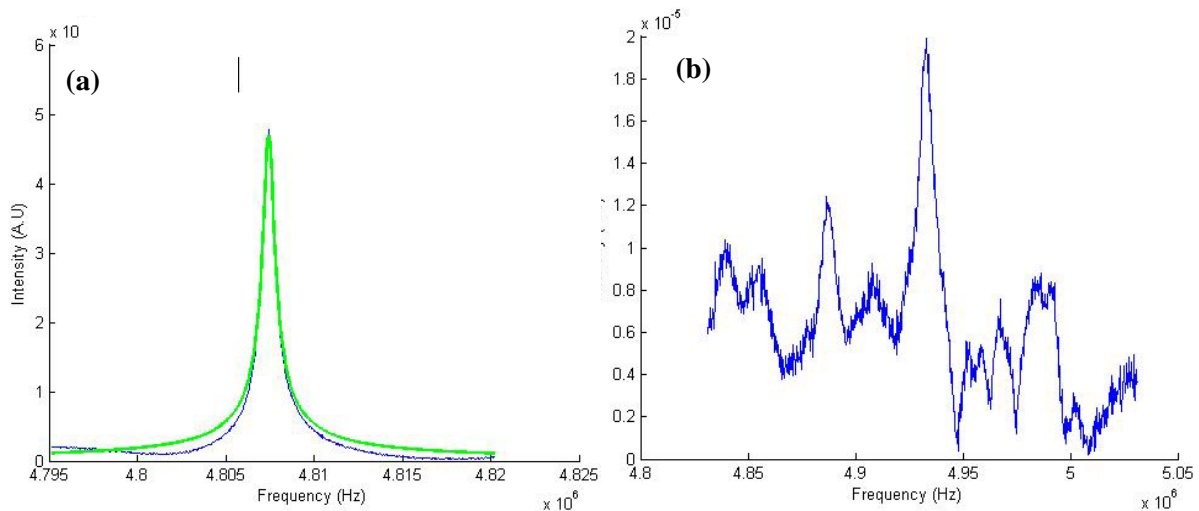
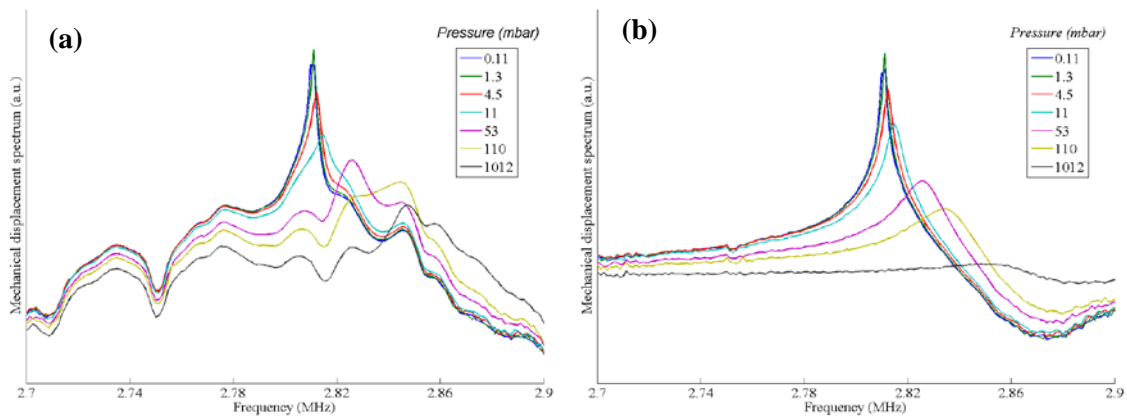


Figure 4.12. Frequency response optical measurement of a circular device with a single cavity of  $r = 15 \mu\text{m}$  in both (a) primary vacuum ( $P = 0.1 \text{ mbar}$ ) and (b) atmospheric pressure ( $P = 1 \text{ 012 mbar}$ ). The unclear peak shape causes difficulties in the determination of the Q factor in atmospheric pressure.

The reason behind the multiple peaks observed during the measurement in air became clear when the frequency response of the device with circular cavity ( $r = 20 \mu\text{m}$ ) was observed under varying air pressure (from 0.01 mbar to 1 012 mbar) on a large frequency spectrum. This response is plotted in Figure 4.13.a with a logarithmic scale. The most important fact uncovered by this measurement is that the baseline signal of the device is not flat, but varies with frequency. This behavior was not observed during measurements conducted on the devices with integrated actuation schemes, and it can thus be inferred to the piezo disc used for actuation (it does not have a flat response with respect to the frequency). This explains what really happened during previous measurements using piezo disc in air as shown in Figure 4.12.b: as the air pressure increased, the resonance peak of the device became wider and wide enough that when combined with the nonflat actuation of the piezo, it produced multiple peaks with different heights (depending on the position of the resonant peak). Devices measured in vacuum had a relatively high Q factor, which means that the resonant peak of the device was sufficiently high and narrow so that the non-flat actuation response of the piezo disc was not noticeable.



*Figure 4.13. (a) Frequency response of a device ( $r = 20 \mu\text{m}$ ) under varying pressure ( $P = 0.01 \text{ mbar} - 1\,012 \text{ mbar}$ ), plotted with a logarithmic scale. The resonant peak, along with the non-flat frequency response of the piezo, can be observed. (b) The data set of (a), subtracted with the data at  $P = 1\,012 \text{ mbar}$ . The decrease of vibration amplitude and the increase of resonant frequency with increasing air pressure can clearly be observed.*

To obtain a clearer picture of the device's frequency response under varying air pressure with piezo actuation, the following method was used. The frequency response of the device at atmospheric pressure ( $P = 1\,012 \text{ mbar}$ ) was used as a reference. At this pressure, we assume that the vibration amplitude of the device is small compared to the one at higher vacuum levels and that the response curve consists almost entirely of the contribution of the varying piezo actuation at the range of frequencies of interest. As a result, the data showing the

response of the device in the case of a flat piezo actuation was obtained by dividing the original data set with the reference set (or subtracted if logarithmic scale was used, as shown in Figure 4.13.a). The result of this process for the data set used in Figure 4.13.a is shown in Figure 4.13.b.

It was observed that as the air pressure  $P$  increased from 0.01 mbar to 1 012 mbar, the resonance frequency increased by 20 kHz and the vibration amplitude decreased. The increase in resonant frequency was opposite to what would be normally expected in such resonators, which typically experience a decrease in the resonant frequency due to an increase in effective mass from the air surrounding the device. It is likely that this unexpected result was caused by the presence of an air pocket within the cavity under the resonator: due to its confined nature, this air pocket can be considered to be a spring as well as a damper [20]. This also suggests that the passive devices do not exhibit an airtight cavity, since this result indicates that the air pressure inside the cavity increases with the surrounding air pressure. While this data subtraction method can be useful to evaluate the device frequency response at low pressure, it can be seen from Figure 4.13 (b) that it cannot be used to evaluate the device behavior at atmospheric pressure. This is unfortunate because the nanoplate resonator was initially designed to operate as a mass sensor in liquid and air.

We have thus fully characterized the resonator in atmospheric pressure by using the thermomechanical noise as an actuation force, which is constant for the frequency range under interest. Since the displacement due to the thermomechanical noise is very small, the Fabry-Perot setup was upgraded as discussed in the previous chapter. This enabled us to measure the response of the devices with large cavity radius ( $r = 20 \mu\text{m}$ ). Unfortunately the displacements of the devices with small cavity radius were too small in that case, and no resonance curve could be detected in atmospheric pressure.

Under varying air pressure, the frequency response of the device can be divided into intrinsic, molecular, and viscous regime, depending on the Knudsen number  $Kn$  [21]:

$$Kn = \frac{k_B T}{\sqrt{2}\pi d_{air}^2 P l_{res}} \quad (4.4)$$

with  $k_B$  as the Boltzmann's constant,  $T$  as the temperature,  $d_{air}$  as air collision diameter,  $P$  as the air pressure, and  $l_{res}$  as the resonator's characteristic length (diameter in the present case). Even in perfect vacuum, energy dissipation occurs by intrinsic mechanisms such as phonon-phonon scattering, phonon-electron scattering, thermoelastic damping, support dissipation, and surface defect dissipation [22].

When the surrounding gas pressure increases, the increased dissipation causes a decrease of the total measured  $Q$  factor,  $Q_{total}$ :

$$Q_{total}^{-1} = \sum Q_i^{-1} \quad (4.5)$$

where  $Q_i$  is the  $Q$  factor corresponding to distinct dissipation mechanisms (intrinsic, air, fluid, etc). Measurement in the intrinsic regime (for  $Kn > 100$ ) is directly influenced by the material property and process variations. Measurement in the molecular and viscous regime is useful to identify the damping model which applies to our resonator, and can be used when designing devices operating in practical conditions.

$Q$  vs  $P$  measurement results for the devices characterized in Figure 4.10 ( $r = 20 \mu\text{m}$ ) are shown in Figure 4.14. In the intrinsic regime, the device exhibits a  $Q$  factor of around 3 000, which is typical for most of the devices we fabricated. As the pressure increases, the device enters the molecular regime ( $100 > Kn > 0.01$ ), where the momentum transfer between the air molecules and the resonator becomes dominant.

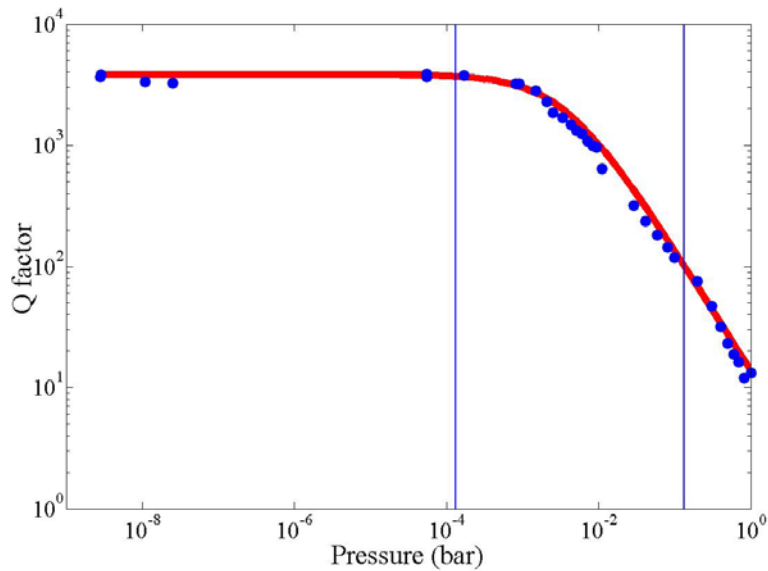


Figure 4.14.  $Q$  vs.  $P$  profile for structure with radius  $r = 20 \mu\text{m}$ , plate thickness  $t = 0.34 \mu\text{m}$ , and gap height  $h = 1.25 \mu\text{m}$ . Blue markers indicate measurement data, while the red line corresponds to  $Q$  factor obtained by substituting  $Q_{intrinsic} = 3000$  and  $Q_{mol}$  from Equation 4.6 into Equation 4.5. The vertical blue lines indicate boundaries between different damping regimes ( $Kn = 100$  for intrinsic to molecular and  $Kn = 0.01$  for molecular to viscous).  $Q$  factor values are extracted from the vibrational noise spectra of the device.

Here, it was observed that similar to other MEMS devices, the  $Q$  factor is inversely proportional to the air pressure [21]:

$$Q_{mol} = \left(\frac{\pi}{2}\right)^{1.5} \frac{\sqrt{RT/M_{air}}}{P} t \rho f \quad (4.6)$$

with  $R$  the gas constant ( $R = 8.317 \text{ J.mol}^{-1}.\text{K}^{-1}$ ),  $T$  the absolute temperature (K),  $M_{air}$  the molar mass of air ( $29 \text{ g.mol}^{-1}$ ),  $P$  the air pressure (Pa),  $t$  the resonator plate thickness,  $\rho$  the density of the resonator material (for Si  $\rho = 2329 \text{ kg.m}^{-3}$ ), and  $f$  the vibration frequency of the resonator. While a narrow gap between a resonator and the substrate commonly produces additional damping due to squeeze film effect [23] for cantilevers, this is not the case for enclosed plate structures (as in our case), since there is no air flowing between the gap and the environment.

The red line in Figure 4.14 corresponds to  $Q$  factor obtained by substituting  $Q_{intrinsic} = 3000$  (which was obtained experimentally at high vacuum) and  $Q_{mol}$  from equation 4.6 into Equation 4.5. It can be seen that this model adequately describes the experimental results, even in viscous regime up to atmospheric pressure, where a quality factor of  $Q = 13$  was observed for devices with  $r = 20 \text{ }\mu\text{m}$  (Figure 4.15). It has to be noted that the low quality factor observed at atmospheric pressure was related to the geometry of the device, and it was not due to the nature of the transfer printing process. In fact, it should be possible to get devices with higher  $Q$  factor in air by increasing the plate thickness and the device resonance frequency.

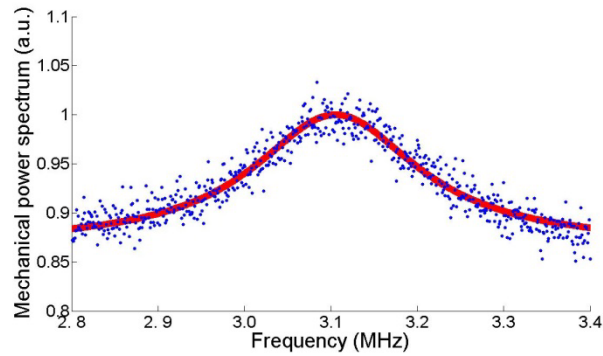


Figure 4.15. Vibrational noise spectra for a device with plate radius  $r = 20 \text{ }\mu\text{m}$ , plate thickness  $t = 0.34 \text{ }\mu\text{m}$ , and gap height  $h = 1.25 \text{ }\mu\text{m}$ . in atmospheric pressure ( $P = 10^{-2} \text{ mbar}$ ), measured using only thermal noise.

The shift of resonance frequency relative to the resonance frequency in vacuum  $(f_0 - f_v)/f_v$ , with  $f_v = 2.798 \text{ MHz}$  the resonant frequency measured in vacuum using thermomechanical actuation is shown in Figure 4.16. Analogously to the results shown in Figure 4.13, negligible shift of  $f_0$  was observed until the device entered the molecular regime, where the frequency of the device increased with pressure. At  $1012 \text{ mbar}$ , i.e. at atmospheric pressure, the resonant

frequency of the device is 3.106 MHz, compared to 2.798 MHz in the intrinsic regime. Most of the  $f_0$  increase can be attributed to the air below the closed gap, which acts as an added stiffness and increases the effective spring constant  $k_{eff}$  of the device. The influence of possible temperature variations on  $f_0$  is negligible, with typical value for frequency drift of the order of -30 ppm / °C [24]. This is to be compared to the 10% shift observed here.

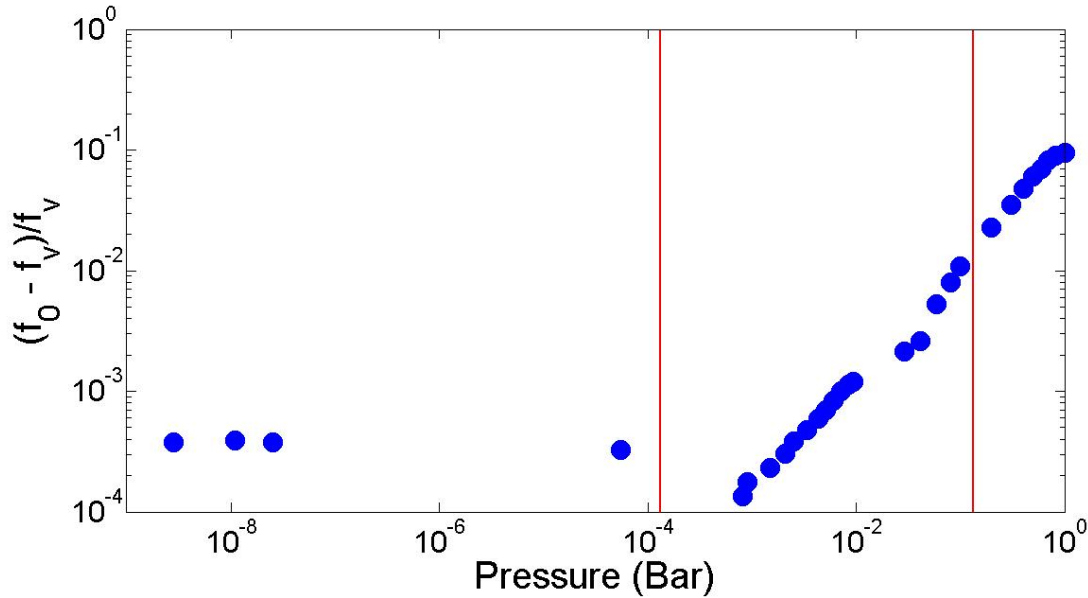


Figure 4.16. Relative shift of the resonance frequency  $(f_0 - f_v)/f_v$  vs. pressure for structure with diameter  $r = 20 \mu\text{m}$ , plate thickness  $t = 0.34 \mu\text{m}$  and gap height  $h = 1.25 \mu\text{m}$ . Resonance frequency values are extracted from the vibrational noise spectra of the device.

### 4.2.3 Characterization of multiple cavities in vacuum

Figure 4.17 shows measurement results conducted in primary vacuum for a structure with four identical square cavities ( $20 \mu\text{m}$  side length). Lorentzian peaks corresponding to mechanical resonances were observed on plates above the cavities, with no observable sign of mechanical crosstalk between the plates. It was observed that while a single plate was shared by the four cavities, they produced different resonant frequencies (7.77, 8.82, 8.17, and 7.51 MHz) and intrinsic Q factor (11 508, 2 467, 4 246, and 5 090). This variation suggests a non-uniform internal plate stress and a difference of clamping quality between the base and the plate. On the other hand, this proves that the micro-masonry technique is flexible enough to be used on varying cavity sizes and shapes.

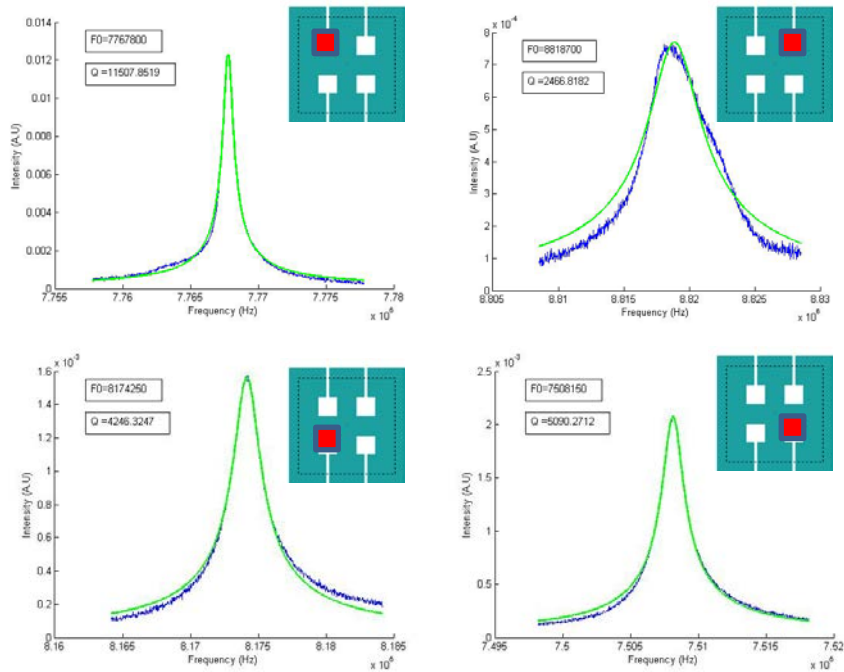


Figure 4.17. Optically measured frequency responses of a device with four identical square cavities, each with side length of  $20\ \mu\text{m}$ . The variation of  $Q$  factor and resonant frequencies suggest a non-uniform internal plate stress and a variation of clamping quality between the base and the plate.

#### 4.2.4 Characterization of multiple cavities in atmospheric pressure

Figure 4.18 shows the frequency response of a passive structure with multiple cavities in atmospheric pressure excited with the external piezo actuator. In this case, the passive structure contains 4 square-shaped cavities with side length  $r = 20\ \mu\text{m}$ . As in the case of single cavity devices excited the same way (see subsection 4.2.2), the response of the piezo creates multiple non-lorentzian peaks. Moreover, since all cavities are of identical size, we did not know if we could resolve each cavity response and if the response shown in Figure 4.18 was not due to cross talk. Unfortunately, because of the small size of the cavities, we could not apply the thermomechanical displacement approach used to observe the frequency response of single cavity devices, which would have answered the previous question.

As a result, a second multiple cavities device was designed and fabricated, as shown in Figure 4.19. These devices consisted of three circular cavities with different radius, which produced different resonant frequencies. To study the effect of cavity size on crosstalk, we designed two devices with different sets of cavity. To study the effect of distance between the cavities on crosstalk, we also included devices with various separation distances between the cavities.

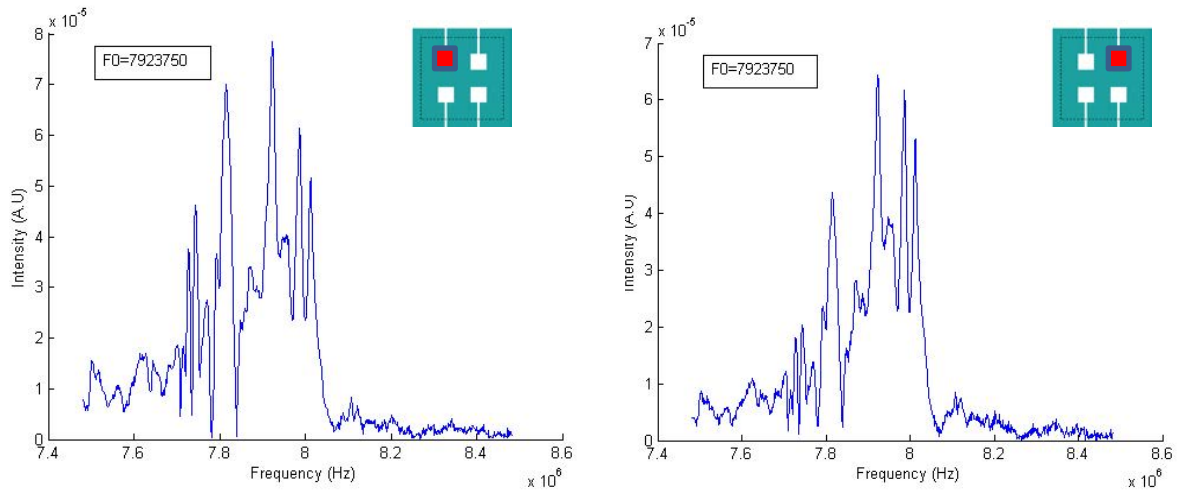


Figure 4.18. Frequency response of devices with 4 square cavities of side length  $r = 20 \mu\text{m}$  for two cavities in atmospheric pressure ( $P = 1.012 \text{ mbar}$ ). The unclear peak shape causes difficulty in determination of the  $Q$  factor in atmospheric pressure. The inset shows the cavity which frequency response is shown.

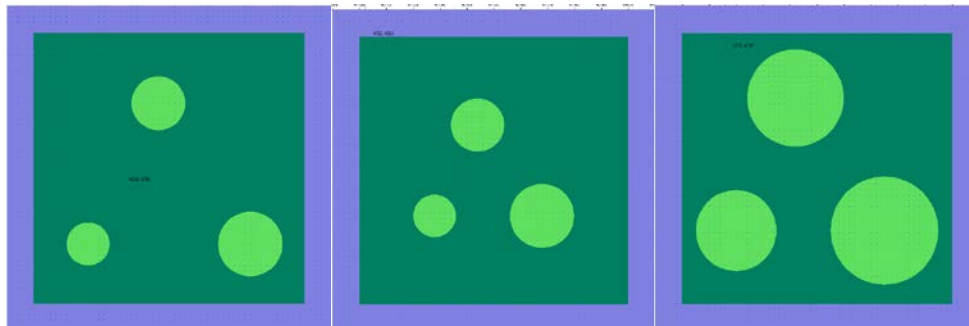
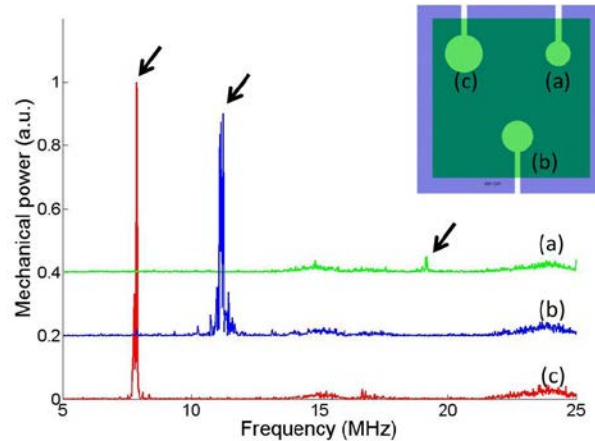


Figure 4.19. The second multiple cavity device design. Dimensions of each device from left to right: First device ( $r = 8, 10, 12 \mu\text{m}$ ;  $40 \mu\text{m}$  spacing between the cavities), second device ( $r = 8, 10, 12 \mu\text{m}$ ;  $20 \mu\text{m}$  spacing between the cavities), and third device ( $r = 15, 18, 20 \mu\text{m}$ ;  $20 \mu\text{m}$  spacing between the cavities).

A typical measurement result for the second multiple cavities device is shown in Figure 4.20. Here, the piezo disc actuation was used to induce high vibration amplitudes and the measurement was done in atmospheric pressure. No resonance peak from neighboring plates was observed when one of the plates was measured, which suggest minimal, if any,

mechanical crosstalk between the suspended structures. This means that device anchoring strength is rigid enough to diminish acoustic radiation between adjacent suspended structures, and micro-masonry thus allows the fabrication of devices with separate responses within a single base structure in a single step.



*Figure 4.20. Frequency response obtained in air of a multiple cavity device with plate thickness  $t = 0.34 \mu\text{m}$  and radius (a)  $r = 8 \mu\text{m}$  (green, 18.8 MHz peak) (b)  $r = 10 \mu\text{m}$  (blue, 10.9 MHz peak), and (c)  $r = 12 \mu\text{m}$  (red, 7.7 MHz peak). Arrows indicate the location of resonance peaks. The curves for (a) and (b) are vertically shifted by 0.4 and 0.2 respectively for clarity. It can be seen that no crosstalk between cavities is observed. Inset: schematic top view of the device.*

### 4.3 Characterization of active devices

In this subchapter, we discuss the characterization results of active devices. The focus of this discussion is an active device with two identical cavities ( $r = 14 \mu\text{m}$ ), as shown in Figure 4.20. First, results obtained using the Fabry-Perot interferometer (optical sensing) and capacitive actuation are presented. Afterwards, we focus on the results obtained with electrostatic actuation and capacitive sensing. Discussions concerning the displacement of the device and shift of the resonant frequency with respect to DC bias then follow. Finally, comparison of device performances at atmospheric pressure and primary vacuum are detailed.

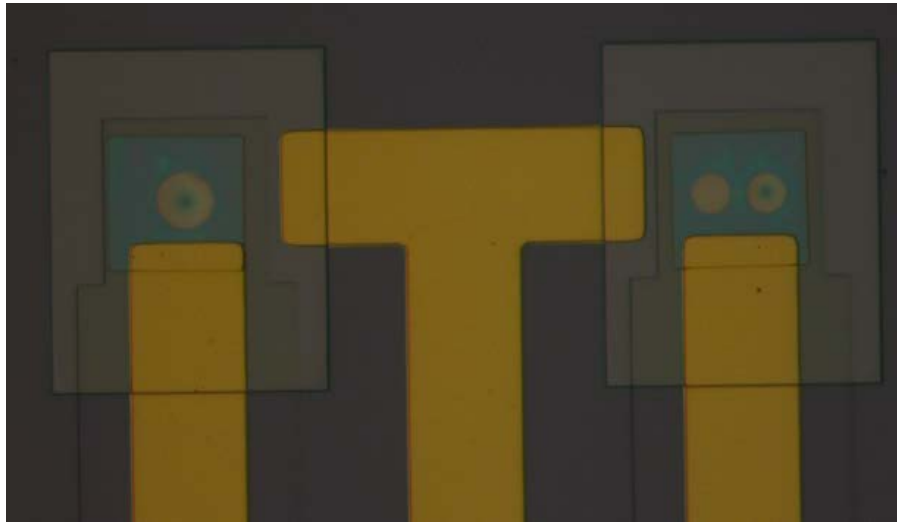


*Figure 4.21. Optical microscope image of fabricated nanoplate resonators. The device of interest is the one on the right hand side, with double cavities of  $r = 14 \mu\text{m}$ . The device on the left hand side functioned as a reference capacitor.*

### 4.3.1 Optical characterization of active devices

The optical characterization of the active devices was carried out using the integrated electrostatic actuation in order to avoid the influence of the erratic response of the external piezo actuator (subsection 4.2.2) and because actuation by thermomechanical noise was too small for adequate optical detection. The optical measurement was carried out separately on both resonators of the same plate while varying the  $V_{DC}$ , and the resulting frequency response was normalized with respect to the highest peak. Figure 4.22 shows the frequency response of the two resonators of the active device shown in Figure 4.21 under  $V_{DC}$  ranging from 0 to 3.5 V at atmospheric pressure ( $P = 1\,012 \text{ mbar}$ ). It can be observed that although both cavities share the same design (circular with  $r = 14 \mu\text{m}$ ), they produce resonant peaks at slightly different frequencies. This is consistent with the variations observed in passive structures with multiple cavities (subsection 4.2.3). Both peak heights, which are proportional to the plate displacement in the case of optical characterizations, appear to vary linearly with  $V_{DC}$  (Figure 4.24). It was observed that resonant peaks are detected even at  $V_{DC} = 0 \text{ V}$ , which should not happen in idealized device, as described in chapter 3. This behavior is due to the DC offset inside the device that is made of highly-doped silicon. The value of this DC offset is  $V_{offset} = 0.32 \text{ V}$ : this value was determined by adjusting the DC bias until the peak value fell down under the noise level of the measurement device.

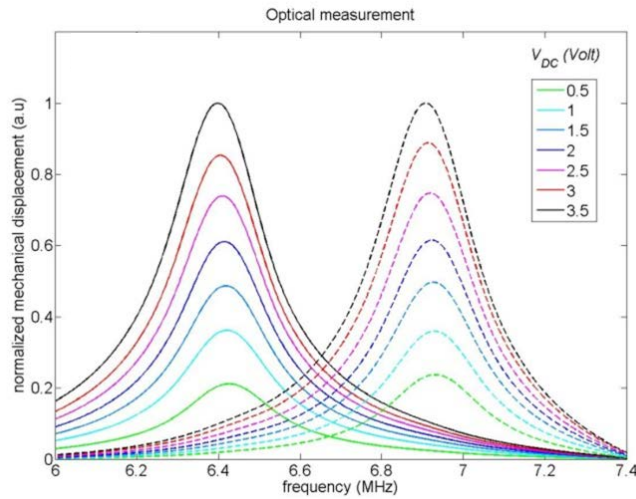


Figure 4.22: Frequency response of the device obtained using optical Fabry-Perot sensing and electrostatic actuation method, for  $V_{DC} = 0.5$  to  $3.5$  V. The figure was created by combining optical measurement results obtained for each resonator of the same plate at different  $V_{DC}$  levels.

### 4.3.2 Capacitive characterization of active devices

Figure 4.23 shows frequency response of the active device shown in Figure 4.21 under  $V_{DC}$  ranging from 0 to  $3.5$  V, obtained using capacitive detection and actuation in atmospheric pressure ( $P = 1012$  mbar). Similar to optical characterization results described previously, two resonant peaks corresponding to the two resonators can be observed. Since the plate above the two cavities are electrically connected, both peaks can be observed simultaneously in the same measurement acquisition. The peak height (corresponding to the measured current) does not appear to vary linearly with  $V_{DC}$  (Figure 4.24). In contrast to optical sensing, distinct peaks can only be distinguished starting at  $V_{DC} = 1.5$  V; below this dc voltage bias, no clear resonant peaks can be observed.

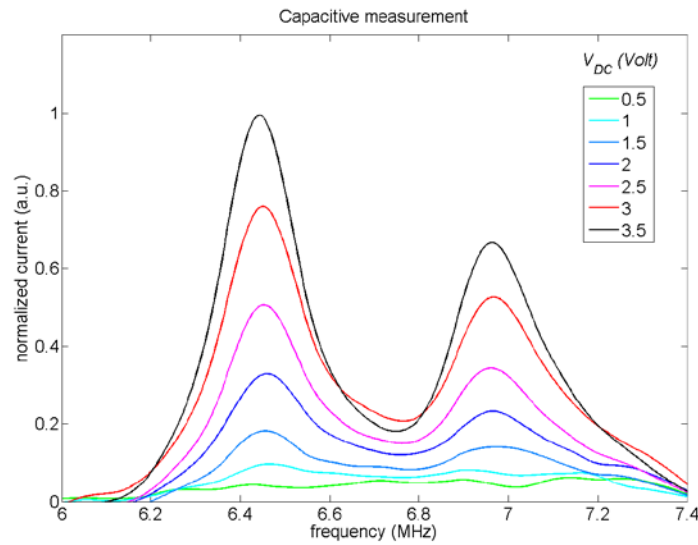


Figure 4.23. Frequency response of the device obtained using capacitive actuation and sensing method, for  $V_{DC} = 0.5$  to  $3.5$  V. The frequency response of both cavities can be observed simultaneously using capacitive sensing.

#### 4.3.3 Variation of peak height and resonant frequency with respect to $V_{DC}$

The normalized mechanical displacement and the normalized output current for one of the resonators are plotted in Figure 4.24 as a function of  $V_{DC}$ . While in general the amplitude of the circular plate capacitor is a nonlinear function of  $V_{DC}$  [25], the displacement of the device is small enough so that the experimentally measured amplitude is observed to be linear up to DC bias value of  $3.5$  V. However, the output current is observed to vary with the square of  $V_{DC}$ . Looking back into equation 3.4, it can be observed that  $I_{total}(t)$  is proportional to  $V_{DC}^2$  only if  $\Delta C$  is proportional to  $V_{DC}$ , which, similarly to the case of the amplitude vibration, is true only for small displacements. Thus, both optical and capacitive measurements show that the device behavior is consistent with what is expected for parallel plate capacitors in the linear regime for  $V_{DC}$  values between  $0.5$  to  $3.5$  Volts.

The variation of resonant frequency with  $V_{DC}$  for the first resonator is shown in Figure 4.21 for both optical (empty blue circle) and capacitive (filled blue circle) sensing. Comparison between the two sensing methods shows that optical sensing results in lower resonant frequency values (around  $45$  kHz lower) compared to the ones measured with capacitive sensing. This can be attributed to heating of the device by the sensing laser beam, which causes compressive thermal stress that reduces the resonant frequency (see next subsection for more details). For both sensing methods, it can be observed that the resonant frequency linearly decreases as the  $V_{DC}$  increases. The optical sensing method shows that between  $V_{DC} = 0.5$  V and  $V_{DC} = 3.5$  V the resonant frequency is reduced by  $27.5$  kHz while the capacitive

sensing method shows that the resonant frequency is reduced by 12.5 kHz when  $V_{DC}$  increases from 1.5 V to 3.5 V. These results are consistent with spring softening effect observed in capacitive devices [26].

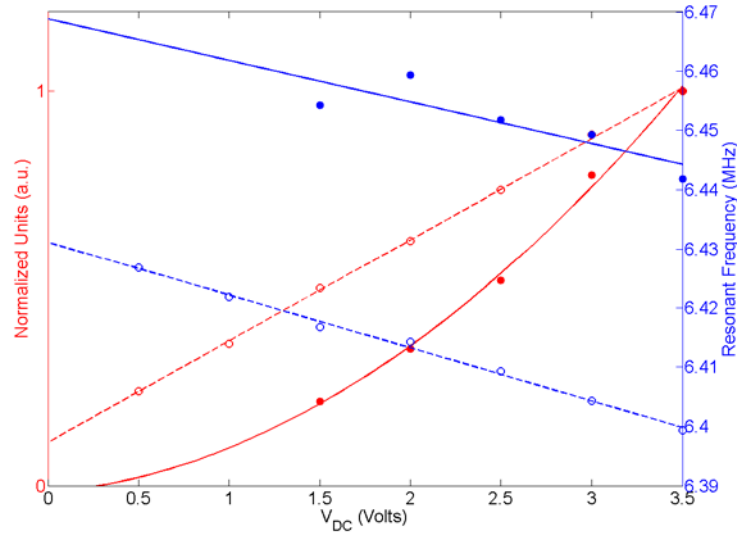


Figure 4.24. Graph describing the variation of peak height (red) and resonant frequency (blue) with  $V_{DC}$  using both optical (empty circles) and capacitive (filled circle) sensing methods. The guiding lines are plotted using a linear curve fit, with the exception of the solid red line which uses a quadratic curve fit. The graph corresponds to the response given by the first resonator of the device, with  $f_0$  value of around 6.44 MHz.

#### 4.3.4 Stress in active devices

Similar to the case for passive structures, assuming no stress and substituting  $r = 14 \mu\text{m}$  and  $t = 0.34 \mu\text{m}$  into Equation 4.1 yields an analytical resonant frequency value of  $f_{analytical} = 7.05$  MHz, which is consistent with the value obtained from the optical and capacitive measurements. The lower experimental resonant frequency values still indicate the presence of tensile stress within the plate, just as in the case of passive structures. Substituting  $f_{experimental} = 6.44$  MHz and 6.96 MHz for the first and second devices into Equation 4.2 yields the in-plane stress values of  $\sigma_0 = -22.2$  MPa and  $-3.4$  MPa, respectively. These values are slightly lower than the average values obtained for passive structures, although it is not clear whether the altered fabrication process is responsible for these lower stress values.

#### 4.3.5 Q factor of active devices in atmospheric pressure and in vacuum

Figure 4.25 shows the frequency response of one of the devices both in atmospheric pressure ( $P = 1012$  mbar) and in vacuum ( $P = 1.2$  mbar) obtained using optical sensing. The Q factor

of the device at atmospheric pressure is determined to be  $Q_{air} = 33$ . Using  $f = f_{analytical}$  into Equation 4.6 yields  $Q_{mol} = 29$ , which is consistent with the experimental results. In vacuum, the Q factor is measured to be only  $Q_{vacuum} = 77$ , which is much lower compared to the values obtained for similar passive structures in vacuum (Table 4.2). This result indicates that a pocket of air exists in the gap between the plate and the substrate even when the measurement chamber is under vacuum, and the seal between the plate and the base structure thus is hermetic. For information, our previous structures exhibited vents within the base structure, thus allowing pressure under the plate to equilibrate the working pressure. While this results in lower  $Q_{vacuum}$ , this does not significantly affect operation in air, and the tight seal can prove advantageous in liquid environment. This also means that our presented process that relies on micro-masonry for the fabrication of nanoplate structures could also be used for obtaining devices with vacuum pockets, which might find applications for pressure sensors.

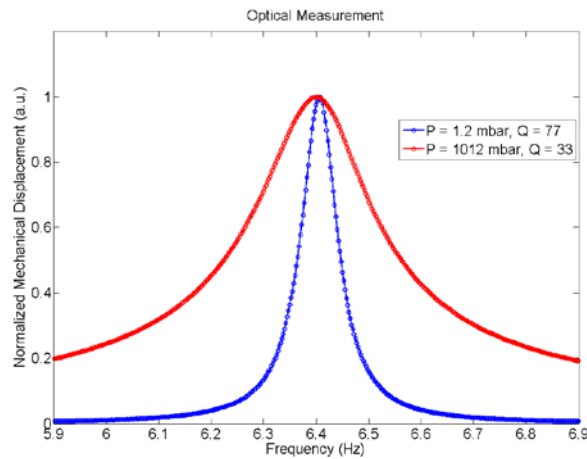


Figure 4.25. Frequency response of the first cavity in vacuum (blue line,  $P = 1.2$  mbar,  $Q_{vacuum} = 77$ ) and in atmospheric pressure (red,  $P = 1012$  mbar,  $Q_{air} = 33$ ). The amplitude of both curves has been normalized due to differences in optical measurement setup.

## 4.4 Other Results

The following subchapter contains some experimental results that do not directly relate to the results presented in the previous subchapters, but that are discussed here since they are considered relevant for future works. Three of the following subsections discuss the fabrication of devices with alternative materials, while two subsections are concerned with some aspects of the measurement method.

### 4.4.1 Base structure fabrication using PECVD and thermal oxide

Samples of the 1<sup>st</sup> fabrication batch were fabricated using both PECVD and thermal  $\text{SiO}_2$  for the base in order to study the difference of vibration behavior between the two materials.

Figure 4.26.a and 4.26.b show typical measurement results in vacuum for a passive structures with bases made out of PECVD and thermal oxide respectively. In both cases, a peak corresponding to the structure resonance can be observed. While some slight differences of Q factor (9 932 vs 11 507) and resonant frequency (7.45 MHz vs 7.77 MHz) exist, these discrepancies are within typical ranges of process variation observed in other structures. Thus no significant difference was observed between base structures made out of PECVD SiO<sub>2</sub> and thermal SiO<sub>2</sub>. For this reason, structures from the 2<sup>nd</sup> batch onwards utilized a PECVD structure due to its better compatibility with the process flow and the use of highly doped substrates.

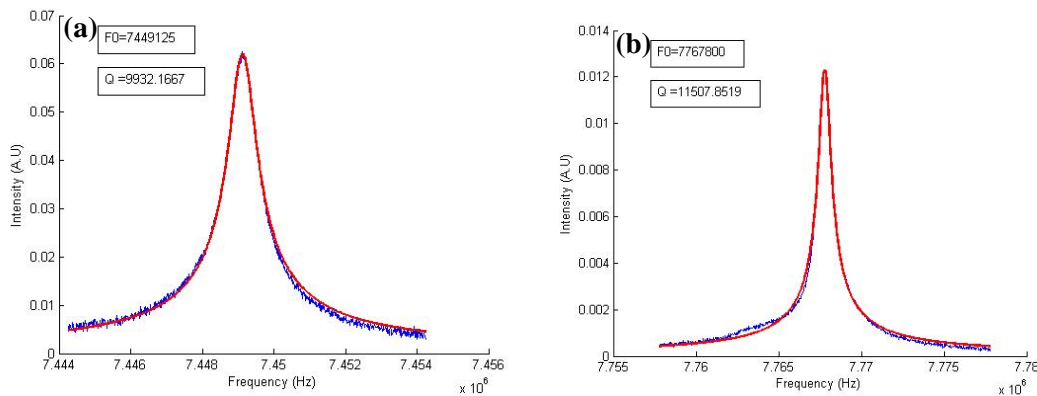


Figure 4.26. frequency response in vacuum ( $P = 10^{-6}$  mbar) for devices with circular cavities ( $r = 12 \mu\text{m}$ ) and base structures fabricated using (a) PECVD SiO<sub>2</sub> and (b) Thermal SiO<sub>2</sub>. No significant difference in term of intrinsic Q factor and resonant frequency exist between the two.

#### 4.4.2 Passive structure fabrication with thick plates

While the majority of structures and devices were fabricated using 0.34  $\mu\text{m}$  thick plates, several passive structures were also made with 1.3  $\mu\text{m}$  thick plates using a thicker SOI donor wafer. This approach was taken to prevent the buckling of resonators with large radius cavities ( $r > 20 \mu\text{m}$ ). Measurement results of a typical device ( $r = 18 \mu\text{m}$ ) with plate thickness  $t = 1.3 \mu\text{m}$  in secondary vacuum ( $10^{-6}$  mbar) using external piezo actuation is shown in Figure 4.27. Similar to measurement results for  $t = 0.34 \mu\text{m}$ , a Lorentzian curve can be seen at resonance. However, there are several notable differences in resonant frequency and Q factor between the devices of different thicknesses.

On average, it was found that devices with thicker plates have larger deviation between the analytical and experimentally measured resonant frequencies. As an example, the experimentally measured resonant frequency of the device which response is presented in Figure 4.27 is  $f_{\text{experimental}} = 7.35$  MHz. Using the analytical formula for resonant frequency (Equation 4.1, assuming zero radial stress), we found an analytical resonant frequency value

of  $f_{analytical} = 16.3$  MHz. Thus, the measured frequency of the device is less than half the theoretical frequency. Calculating the radial stress with Equation 4.2 yields a compressive stress value of 950 MPa, which is much larger than the one observed for devices with thinner plates. While we were unable to determine the cause of this result, it is possibly related to the difference of heat transfer characteristics between thick and thin plates during the thermal anneal process. Additionally, it was also found that devices with thicker plates have lower Q factors. As an example, the experimentally measured intrinsic Q factor of the device which response is presented in Figure 4.27 is  $Q = 1\,589$ . Of all the measured samples with  $t = 1.3$   $\mu\text{m}$ , none had an intrinsic Q factor exceeding 2 000, a value which is considered low for devices with  $t = 0.34$   $\mu\text{m}$ .

In terms of the original goal of avoiding buckling, the use of thicker plates can be considered successful. Out of 21 passive structures that were fabricated using 1.3  $\mu\text{m}$  thick plates, none were found to buckle when observed using an optical microscope. However, delamination was found to be the dominant failure mode for the 2<sup>nd</sup> sample batch. A total of 17 devices with 1.3  $\mu\text{m}$  plates were found to be delaminated (totally and partially), which correspond to a device yield of only 28.6%: this figure is barely any better compared to the 29.2% yield for 0.34  $\mu\text{m}$  thick plates from the same batch. Additionally, using thicker plates meant lower device sensitivity as a mass sensor and lower mechanical displacement for the same amount of driving voltage, which would render capacitive sensing more difficult. Thus, it was decided that active devices would not be fabricated using thick plates. However, this work demonstrated the possibility of using the micro-masonry technique for the fabrication of mechanical resonators of different thicknesses.

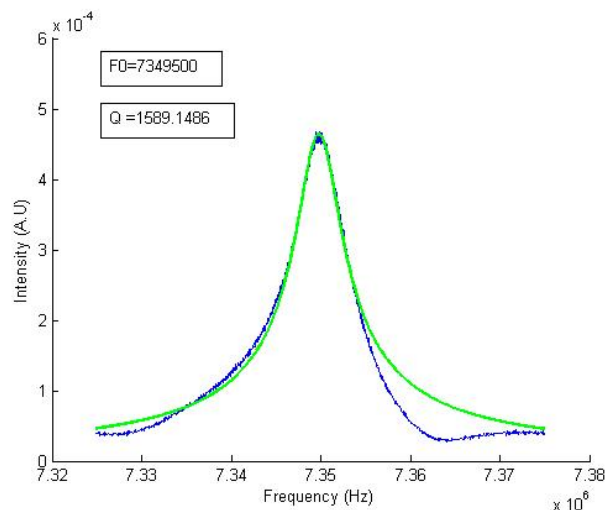


Figure 4.27. Frequency response of a device with thicker plates ( $r = 18$   $\mu\text{m}$ ,  $t = 1.3$   $\mu\text{m}$ ) actuated using the piezo disc in secondary vacuum ( $P = 10^{-6}$  mbar). The observed resonant frequency is much lower than the one predicted using the analytical formula, and the Q factor is lower compared to devices with thinner plates.

### 4.4.3 Transfer printing of silicon plates onto gold surface

During the course of this study, a new design for device with integrated actuation and sensing was proposed, as shown in Figure 4.28. In this design, the metallization layer (Au) acts both as an electrical interconnect for the resonator plate and as an adhesion layer, which contacts the bottom surface of the Si nanoplate. Au/Si layer has been shown to produce eutectic bonding [27] at lower anneal temperature than the one used for the Si-SiO<sub>2</sub> interface (340 vs 900 °C), which might reduce the thermal stress in the nanoplate. Additionally, this design enables a fully planar interconnect for both top and bottom electrodes, which is easy to achieve with evaporation techniques since it does not require a conformal coating. The Au layer is also used to create the bottom electrode of the device. Compared to the use of the highly-doped silicon substrate, the Au electrode has a lower *RC* time constant which enables it to be driven at higher frequencies. It also enables the usage of complex bottom electrode geometries, which might be interesting for actuating higher vibration modes. Additionally, the gold layer acts as an optical reflective layer, which gives higher S/N ratio for Fabry-Perot measurements. However, the resonator shape is then changed due to the necessity of getting an interconnect layer in the center of the cavity: because of the resolution of the photolithography process, we must leave a gap of at least 2 μm between the edge of the gold layer and that of the cavity. While not significant for circular cavities with large diameter ( $r = 30\text{-}20\ \mu\text{m}$ ), it alters the cross section of smaller cavities significantly. However, this does not affect the ability of the device to be actuated and sensed at its resonant frequency.

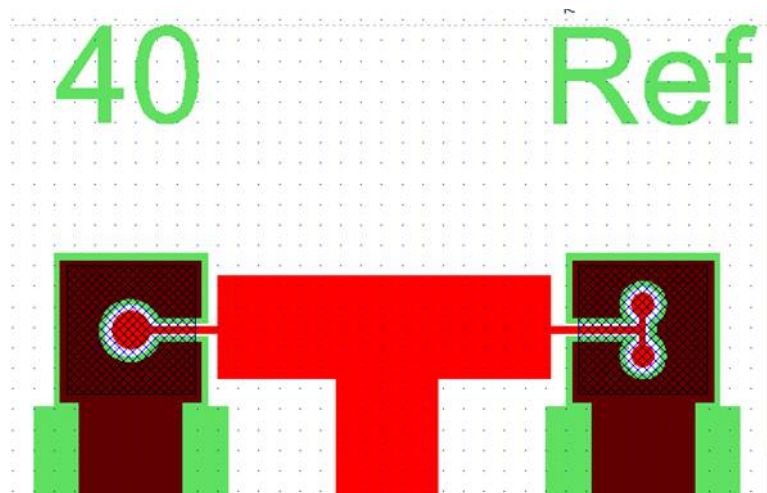
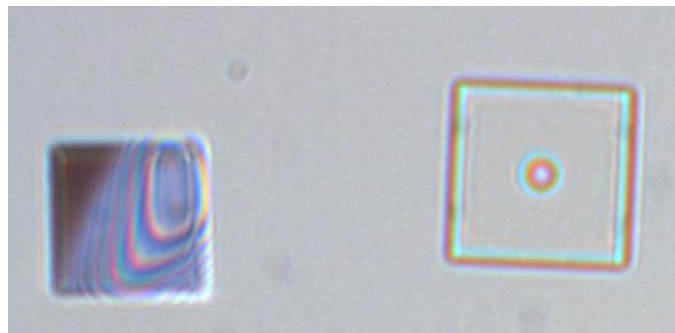


Figure 4.28. Schematics of the new device. The green surface represents the SiO<sub>2</sub> base structure; the red surface represents the Au interconnect/adhesion layer, and the blue crossed surface represents the Si nanoplate.

The primary challenge of this approach was to obtain an adequate adhesion between the silicon nanoplate and the Au surface from the micro-masonry process. Unfortunately the adhesion between the silicon and gold surface was found to be unsatisfactory, and delamination between the plate and the base structure was very frequent (see Figure 4.29). This result was unexpected, since previous works showed the successful transfer-printing of Au inks onto silicon surfaces [28]. It is possible that the poor adhesion problem might be solved by using some proper surface treatment or other metals as a welding material. However, this device was not developed further due to time limitation and minimal improvement to the performance of the finished device in atmospheric pressure; further study should be conducted if wishing to realize this type of devices.



*Figure 4.29. Optical Microscope image of delamination of the silicon plate from a base structure covered with Au.*

#### 4.4.4 Modelling of laser heating using COMSOL

During the dynamic measurements, we also observed that the value of  $f_0$  depended on the intensity of the laser used for the measurement. Figure 4.30.a shows a typical effect of laser intensity to the measured  $f_0$ . In general,  $f_0$  increased as the laser intensity was lowered. This was caused by the effect of laser heating up the membrane. Adsorption of the laser power and temperature increase within the membrane resulted in the built up of compressive thermal stress, which thus lowered the resonance frequency.

This was modeled in COMSOL, with results shown in Figure 4.30.b. The laser was modeled as a heat source with gaussian distribution in the membrane. The model itself was taken from COMSOL database, originally used for glass defect repair using laser [29]. As for the geometry, only the Si membrane and SiO<sub>2</sub> base were included, while the Si substrate was not considered. For temperature boundary condition, we did not include any convection effects (vacuum condition), and the bottom of the SiO<sub>2</sub> base was used as a heat sink with a fixed temperature of 27 °C. The effect of Si/SiO<sub>2</sub> contact resistance was determined to be

insignificant in this case [30]. The device was mechanically constrained at the bottom of the SiO<sub>2</sub> base, and free to move otherwise. The model first calculated the steady-state temperature of the system, then calculated the resulting stress, and finally the eigenfrequency of the stressed system. The results using full and half laser intensity were compared with the experimental measurements.

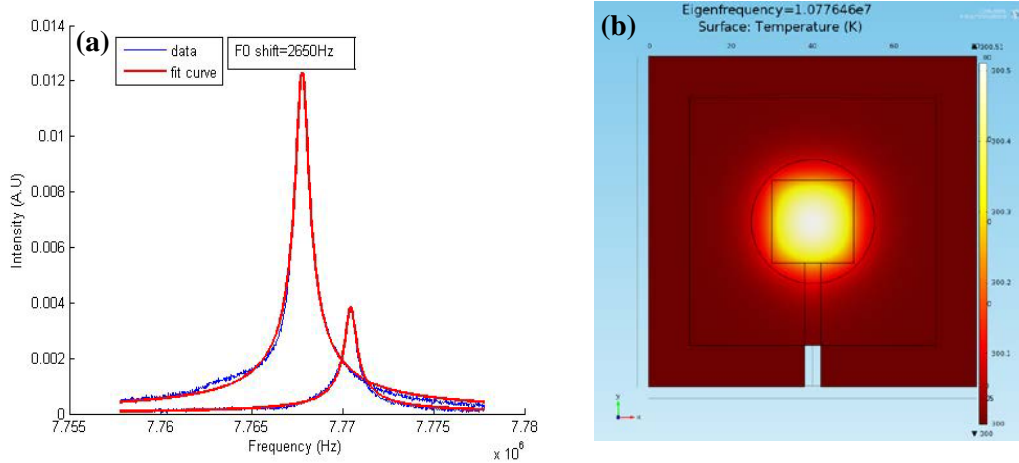


Figure 4.30. Effect of laser heating on the resonant frequency. (a) measurement results of a square, open cavity under full (large curve) and half (small curve) laser intensity. Note the shift to higher frequency as the intensity is lowered. (b) temperature distribution of a square, open cavity sample heated by laser modeled using comsol.

Table 4.5. Comparison between experimental and modeling results of frequency shift due to laser heating. The experimental measurements were done on 4 samples (square resonators with closed cavities) which were made using thermally-grown SiO<sub>2</sub> bases.

Experimental	Cmsol
$\Delta f$ (Khz)	$\Delta f$ (Khz)
2.3	2.63
2.15	
1.08	
2.65	

The results (Figure 4.30 and Table 4.5) show a reasonable agreement between the model and the experiments, both in magnitude and in trend, thus supporting our hypothesis.

#### 4.4.5 Effective parameter determination using Fabry-perot setup

This subchapter describes the experimental determination of effective parameters using harmonics as described in subchapter 3.3. A commercial silicon nitride AFM probe with a reflective layer (SNL – 10 from Bruker [31]) was used as the device under test, as shown in Figure 4.31. The AFM probe has a dimension of 120  $\mu\text{m}$ , 20  $\mu\text{m}$  and 0.6  $\mu\text{m}$  respectively for length, width, and thickness. The specification ranges given by the manufacturer are as follows: resonance frequency  $f_0$  between 40 – 75 kHz, effective spring constant  $K_{eff}$  between 0.12 – 0.48 N/m, and effective mass  $M_{eff}$  of  $1.94 \pm 0.75$  ng. The AFM probe chip was glued using cyanoacrylate onto a 1 cm  $\times$  1 cm silicon base, which was diced from a standard 100 mm wafer. This gives a gap value of around 300  $\mu\text{m}$  between the probe and the base. The probe and base assembly was then attached to the piezo disc for actuation.

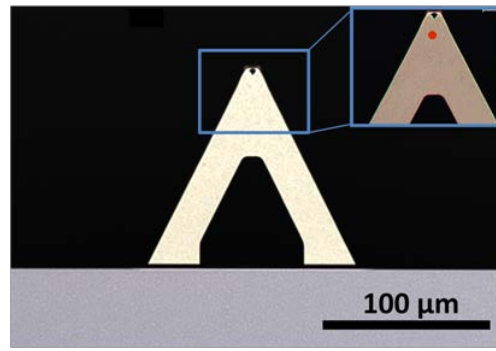


Figure 4.31. Optical microscope images of the AFM probe under study. The cantilever's dimensions are 120 $\mu\text{m}$   $\times$  20  $\mu\text{m}$   $\times$  0.6  $\mu\text{m}$  respectively for length, width and thickness. The red dot corresponds to the laser beam location during measurement. The AFM probe is glued to a piece of silicon substrate, which forms a Fabry-Perot cavity.

The 1<sup>st</sup>, 2<sup>nd</sup>, and 3<sup>rd</sup> resonance peaks obtained using piezo actuation at  $f_0 = 63.33$  kHz (mechanical resonance frequency),  $2 \times f_0 = 126.67$  kHz and  $3 \times f_0 = 190$  kHz, are shown in Figure 4.32.a. The signal magnitudes of the 1<sup>st</sup> and 3<sup>rd</sup> peak are -56.9 dBm and -93.3 dBm respectively, with a noise floor at around -120 dBm. From these values, the ratio  $L_3/L_1$  is determined to be -36.4 dB. Using this ratio and the value of  $\lambda = 632$  nm in Equation 3.17 (Chapter 3) yields the value of  $x_{pk} = 30.4$  nm, corresponding to a signal magnitude of the fundamental line  $L_1 = -56.9$  dBm.

Figure 4.32.b shows the measurement of the resonance peak at  $f_0$  caused by thermomechanical noise acquired using a resolution bandwidth (RBW) of 3 Hz. The data were averaged over 100 times to reduce the effect of noise, and a lorentzian curve was fitted to extract the noise spectral density at resonance  $L_{noise} = -117$  dBm with a noise floor of -123 dBm (RBW=3 Hz) and quality factor  $Q = 870$ . Substituting these values into Equation 3.12 yields displacement noise spectral density  $x_{noise} = 10.5$  pm/ $\sqrt{\text{Hz}}$  at resonance, effective spring

constant and effective mass values of  $K_{eff} = 0.324$  N/m and  $M_{eff} = 2.05$  ng respectively for the AFM probe. These values are consistent with the one obtained from the manufacturer's specifications, as can be summarized in Table 4.4, which takes into account error bars caused by measurement uncertainties related to the linearity and the flatness of the photodiode and analyzer response.

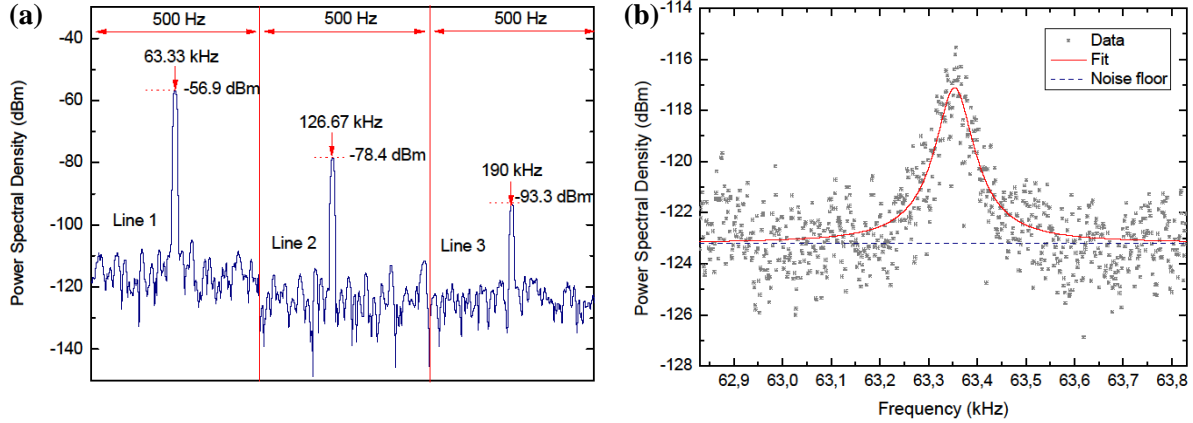


Figure 4.32: (a) Frequency spectrum of the interferometer signal of DUT when forced into vibration at the fundamental resonant frequency. An external piezo-shaker is used to drive the DUT vibration. (b) Thermomechanical noise spectrum of the DUT obtained at room temperature and in vacuum (0.5 mbar) using a resolution bandwidth of 3 Hz without any actuation signal.

Table 4.4: Comparison between theoretical values and measurement results obtained for the AFM cantilever shown in Figure 4.31. Fundamental mode of resonance of the DUT is studied. Nominal values are given with extrema values in brackets.

$J_3/J_1$ ratio	$0.0152 \pm 0.0019$	
$x_{peak}$ (nm)	$30.4 \pm 1.8$	
SA calib. (V/m)	$10\,503 \pm 622$	
Q-factor	$870 \pm 35$	
$x_{noise}$ (pm/ $\sqrt{\text{Hz}}$ )	$10.5 \pm 0.36$	
	<b>Theory</b>	<b>Experiment</b>
$f_0$ (kHz)	56 [40-75]	$63.354 \pm 0.001$
$K_{eff}$ (N/m)	0.24 [0.12-0.48]	$0.324 \pm 0.024$
$M_{eff}$ (ng)	$1.94 \pm 0.75$	$2.05 \pm 0.15$

It should be noted that in the present work, modeling and calculations presented in subchapter 3.3 assume that only one optical reflection occurs in the Fabry-Perot cavity. This is a reasonable approach for the device under test because of the low precision involved in preparing and assembling the AFM probe for measurement. In the case of released MEMS devices, especially fabricated from silicon-on-insulator substrates, the Fabry-Perot cavity will consist of 2 low-roughness single-crystal silicon surfaces and multiple optical reflections may be expected, leading to discrepancies between the present modeling and the actual effective parameters. In general, it was observed that our method overestimates the displacement spectrum of these devices by a factor of 2 to 4, leading to the underestimate of the effective spring constant  $K_{eff}$  and effective mass  $M_{eff}$ .

#### 4.5 Summary

This chapter describes the major experimental results obtained in this study. These include the analysis of failure modes of the structures and devices, the dynamic mechanical properties of both active and passive structures in various vacuum conditions, plus other results relevant to the study of nanoplate resonators fabricated with the micro-masonry technique. Buckling and delamination of the plates were found to be the major failure modes of micro-masonry plate resonator fabrication, delamination being more severe. Characterization of passive structures with Fabry-Perot method in vacuum showed an average intrinsic Q factor of around  $Q_{intrinsic} = 4\ 500$  and an average compressive stress level of around 36.7 MPa, which limits the maximum radius of fabricated resonators. In atmospheric pressure, the Q factor of the passive structures was observed to obey molecular damping model, while the resonant frequency increased due to the presence of air below the resonating plate. Frequency responses of structures with multiple cavities showed no sign of mechanical crosstalk, indicating good clamping between the base and the plate. Active device was observed to produce resonant peaks that were detectable using both optical and capacitive sensing techniques, and simultaneous detection of several cavities was possible with capacitive sensing. Similar to the passive structures, the estimated compressive stress in the plate was determined to be around 22 MPa and the Q factor in atmospheric pressure was observed to be well described with the molecular damping model. However, comparison of Q factor of active devices in primary vacuum and atmospheric pressure was not consistent with what has been observed in passive structures, suggesting that the seal between the plate and base structure is airtight.

## References

- [1] Tas N, Sonnenberg T, Jansen H, Legtenberg R and Elwenspoek M 1996 Stiction in surface micromachining *J. Micromech. Microeng.* **6** 385
- [2] Cheng C-L, Tsai M-H and Fang W 2015 Determining the thermal expansion coefficient of thin films for a CMOS MEMS process using test cantilevers *J. Micromech. Microeng.* **25** 025014
- [3] Rogers T and Kowal J 1995 Selection of glass, anodic bonding conditions and material compatibility for silicon-glass capacitive sensors *Sensors and Actuators A: Physical* **46** 113–20
- [4] Tong Q-Y and Goesele U 1999 Semiconductor wafer bonding: science and technology
- [5] Suni T, Henttinen K, Suni I and Mäkinen J 2002 Effects of Plasma Activation on Hydrophilic Bonding of Si and SiO<sub>2</sub> *J. Electrochem. Soc.* **149** G348–51
- [6] Shavezipur M, Ponnambalam K, Khajepour A and Hashemi S M 2008 Fabrication uncertainties and yield optimization in MEMS tunable capacitors *Sensors and Actuators A: Physical* **147** 613–22
- [7] Ramm P, Lu J J-Q and Taklo M M V 2012 *Handbook of Wafer Bonding* (John Wiley & Sons)
- [8] Schomburg W K 2011 *Introduction to Microsystem Design* vol 1 (Berlin, Heidelberg: Springer Berlin Heidelberg)
- [9] Hopcroft M A, Nix W D and Kenny T W 2010 What is the Young's Modulus of Silicon? *Microelectromechanical Systems, Journal of* **19** 229–38
- [10] Pérez Garza H H, Kievit E W, Schneider G F and Staufer U 2014 Controlled, Reversible, and Nondestructive Generation of Uniaxial Extreme Strains (>10%) in Graphene *Nano Lett.* **14** 4107–13
- [11] Shchepetov A, Prunnila M, Alzina F, Schneider L, Cuffe J, Jiang H, Kauppinen E I, Torres C M S and Ahopelto J 2013 Ultra-thin free-standing single crystalline silicon membranes with strain control *Appl. Phys. Lett.* **102** 192108
- [12] Ko S C, Kim Y C, Lee S S, Choi S H and Kim S R 2003 Micromachined piezoelectric membrane acoustic device *Sensors and Actuators A: Physical* **103** 130–4
- [13] Ayela C and Nicu L 2007 Micromachined piezoelectric membranes with high nominal quality factors in newtonian liquid media: A Lamb's model validation at the microscale *Sensors and Actuators B: Chemical* **123** 860–8
- [14] Cha M, Shin J, Kim J-H, Kim I, Choi J, Lee N, Kim B-G and Lee J 2008 Biomolecular detection with a thin membrane transducer *Lab Chip* **8** 932–7
- [15] Lu X, Guo Q, Xu Z, Ren W and Cheng Z-Y 2012 Biosensor platform based on stress-improved piezoelectric membrane *Sensors and Actuators A: Physical* **179** 32–8
- [16] Xu T, Wang Z, Miao J, Yu L and Li C M 2008 Micro-machined piezoelectric membrane-based immunosensor array *Biosensors and Bioelectronics* **24** 638–43
- [17] Alava T, Mathieu F, Mazonq L, Soyer C, Remiens D and Nicu L 2010 Silicon-based micromembranes with piezoelectric actuation and piezoresistive detection for sensing purposes in liquid media *J. Micromech. Microeng.* **20** 075014
- [18] Zhang Q, Cicek P-V, Allidina K, Nabki F and El-Gamal M N 2014 Surface-Micromachined CMUT Using Low-Temperature Deposited Silicon Carbide Membranes for Above-IC Integration *Journal of Microelectromechanical Systems* **23** 482–93
- [19] Timoshenko S and Woinowsky-Krieger S 1959 *Theory of plates and shells* (McGraw-Hill)
- [20] Yang Y-J, Gretillat M-A and Senturia S D 1997 Effect of air damping on the dynamics of nonuniform deformations of microstructures , 1997 *International Conference on Solid*

*State Sensors and Actuators, 1997. TRANSDUCERS '97 Chicago* , 1997 International Conference on Solid State Sensors and Actuators, 1997. TRANSDUCERS '97 Chicago vol 2 pp 1093–6 vol.2

[21] Martin M J, Houston B H, Baldwin J W and Zalalutdinov M K 2008 Damping models for microcantilevers, bridges, and torsional resonators in the free-molecular-flow regime *Microelectromechanical Systems, Journal of* **17** 503–11

[22] Weinberg M, Candler R, Chandorkar S, Varsanik J, Kenny T and Duwel A 2009 Energy loss in MEMS resonators and the impact on inertial and RF devices *Solid-State Sensors, Actuators and Microsystems Conference, 2009. TRANSDUCERS 2009. International Solid-State Sensors, Actuators and Microsystems Conference, 2009. TRANSDUCERS 2009. International* pp 688–95

[23] Bao M, Yang H, Yin H and Sun Y 2002 Energy transfer model for squeeze-film air damping in low vacuum *Journal of Micromechanics and Microengineering* **12** 341

[24] Kim B, Candler R N, Hopcroft M A, Agarwal M, Park W-T and Kenny T W 2007 Frequency stability of wafer-scale film encapsulated silicon based MEMS resonators *Sensors and Actuators A: Physical* **136** 125–31

[25] Ahmad B and Pratap R 2010 Elasto-Electrostatic Analysis of Circular Microplates Used in Capacitive Micromachined Ultrasonic Transducers *IEEE Sensors Journal* **10** 1767–73

[26] Seeger J I and Boser B E 2003 Charge control of parallel-plate, electrostatic actuators and the tip-in instability *Journal of Microelectromechanical Systems* **12** 656–71

[27] Wolffenbuttel R F 1997 Low-temperature intermediate Au-Si wafer bonding; eutectic or silicide bond *Sensors and Actuators A: Physical* **62** 680–6

[28] Keum H, Chung H-J and Kim S 2013 Electrical Contact at the Interface between Silicon and Transfer-Printed Gold Films by Eutectic Joining *ACS Appl. Mater. Interfaces* **5** 6061–5

[29] Matthews M J, Elhadj S, Guss G M, Sridharan A, Nielsen N D, Yoo J-H, Lee D and Grigoropoulos C 2013 Localized planarization of optical damage using laser-based chemical vapor deposition vol 8885 pp 888526–888526 – 9

[30] Chen J, Zhang G and Li B 2012 Thermal contact resistance across nanoscale silicon dioxide and silicon interface *Journal of Applied Physics* **112** 064319

[31] BrukerAFMprobes.com. SNL-10 - Bruker AFM Probes [Internet]. 2015 [cited 8 October 2015]. Available from: <http://www.brukerafmprobes.com/p-3693-snl-10.aspx>

## Chapter 5

# Conclusion and Perspectives

*This final chapter summarizes the important discoveries of this study and recommendations for future research work.*

## 5.1 Conclusion

This study focused on the fabrication of suspended plates for their use as MEMS resonators by micro-masonry. Micro-masonry is a form of transfer-printing, where silicon elements (in our case nanoplates) that are fabricated from a donor SOI wafer, are picked up using microtip polymeric stamps, and released onto another substrate that contains base structures with cavities. Sealing the nanoplate with the base using a thermal annealing process results in suspended structures that can be used as resonators. From this general fabrication method, we have realized two generations of devices: passive structures that were used to study the influence of micro-masonry onto the performances of the resonating device and active devices with integrated actuation and sensing schemes that were used as proof-of-concept of our approach for the fabrication of fully integrated MEMS resonating plates with sealed cavities. The devices were characterized using optical and infrared microscopy, Fabry-Perot interferometry, and capacitive actuation and sensing techniques.

The passive structures and active devices exhibited behaviors consistent with theoretical predictions. The passive structures acted as suspended plates (not as membranes), and the active devices were found to behave as parallel plate capacitive devices. For passive structures, the variation of Q factor under different pressures was adequately explained by molecular damping mechanisms. For active structures, the Q factor did not show significant variations between operation in atmospheric pressure and in vacuum, indicating a sealed air cavity between the plate and the substrate. The tested devices and structures exhibited intrinsic Q factors between 3 000 – 14 000, e.g. modest values compared to similar devices fabricated with conventional fabrication methods. When used as mass sensors in vacuum, this implies comparable or lower sensitivity. When used as mass sensors in air or liquid, the damping is dominated by the surrounding fluid instead of the intrinsic damping, and in this regard, our fabricated resonators are not better or worse than resonators of similar dimensions and materials. In atmospheric pressure, the devices studied showed Q factors in range of 10 – 100, depending on the dimensions and in accordance with the molecular damping model.

The tight bond between the silicon nanoplate and the silicon dioxide base offers several advantages. No mechanical crosstalk was observed between different parts of a single plate suspended under different cavities, which enables the fabrication of device arrays with a single plate. The bond was also found to be strong enough to withstand post-processing fabrication steps, including photolithography, metallization with sputtering, and lift-off processes. Finally, the airtight nature of the cavity of the resonators allow their operation in liquid environment, thus rendering them suitable for mass sensing applications in liquid, e.g. for real-time biosensing.

The current largest limitation of the micro-masonry technique is the low and inconsistent yield. Several approaches such as the use of plasma treatment before bonding and the application of a pressure along the circumference of the cavities after plate transfer were investigated and turned out to be quite successful, thus showing the way to possible

improvements of the micro-masonry technique. Examination of the process yield per fabrication batch showed that it was possible to obtain high yields (above 80%). The vast majority of the yield problems were caused by the delamination of the plates. Another limitation of the micro-masonry technique was found to be the compressive stress introduced into the suspended plate as a result of the thermal annealing step. Compressive stress in the range of 20 MPa induced mechanical constraints in the fabrication of suspended plates with large span and small thickness, because of plate buckling.

In summary, we have demonstrated in this thesis work that suspended plates and active mechanical resonators can be fabricated with the micro-masonry technique. The main advantages of this fabrication technique compared to more conventional approaches lie in its simplicity and the possibility to obtain fully sealed cavities in a single step, making this alternative fabrication method attractive for specific applications.

## **5.2 Perspectives for Future Work**

In order to ensure that micro-masonry can be reliably used to deliver devices for specific applications, the first task would be to proceed with the refinement of this fabrication technique. The focus would be the increase of device yield by minimizing plate delamination. In addition to the improvements proposed in this study, one could also work on adding a tilt control system into the micro-masonry set-up to ensure a better control of the contact during the transfer-printing process. Another related direction of study would focus on transferring other materials than those related to silicon, especially metal layers, which would open up new possibilities in device design and processing.

The second implementation would concern the use of fabricated resonators for dedicated applications: the possibility to obtain sealed cavities using micro-masonry offers a direct advantage for fabricated devices to operate in liquid environment, and thus to act as biosensors. To this aim, the devices presented in this work would still require to see additional process steps. Indeed, operation in liquid would require the insulation of the metal lines and the encapsulation of the conductive silicon plate: in fact, preliminary results not discussed here have shown that this is feasible. Other applications of MEMS devices that operate at quasistatic conditions and require sealed cavities could also be investigated, such as pressure sensors or peristaltic microfluidic pumps.



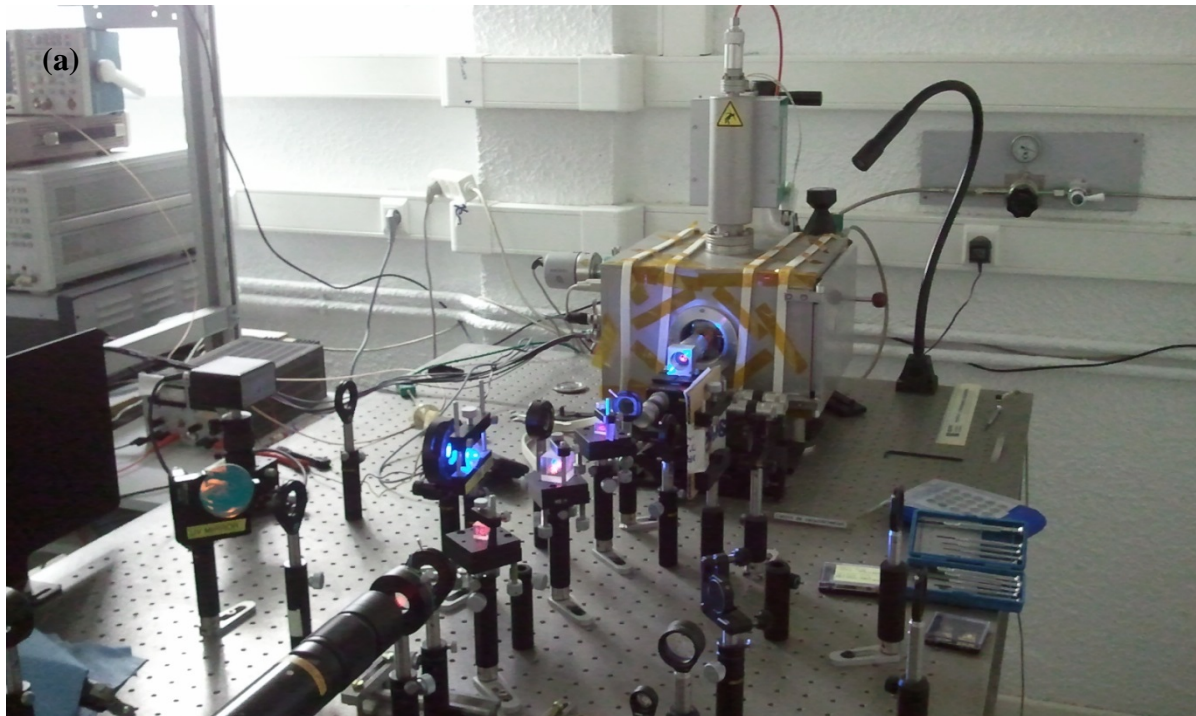
## Appendix A

### Experimental Setup for Optical Measurements

The experimental setup used for Fabry-Perot characterization used in this study is shown in Figure A.1.a, while the schematic is shown in Figure A.1.b. When compared with idealized scheme shown in Figure 3.3.a, the actual experimental setup is more complicated and requires more components. For the detailed description purposes, the setup is subdivided into five components:

1. The electrical components of the interferometer, which include the laser source, the diode, and the network analyser.
2. The optical components of the interferometer, which include the beam expander, the quarter wavelength filter, beam splitters, and a microscope objective.
3. The illumination and imaging components, which include the camera with its objective lenses and the illumination diode.
4. The vacuum chamber.
5. The vacuum system, which include the vacuum pumps, pressure sensors, and valves.

Each of these components will be described in more detail below.



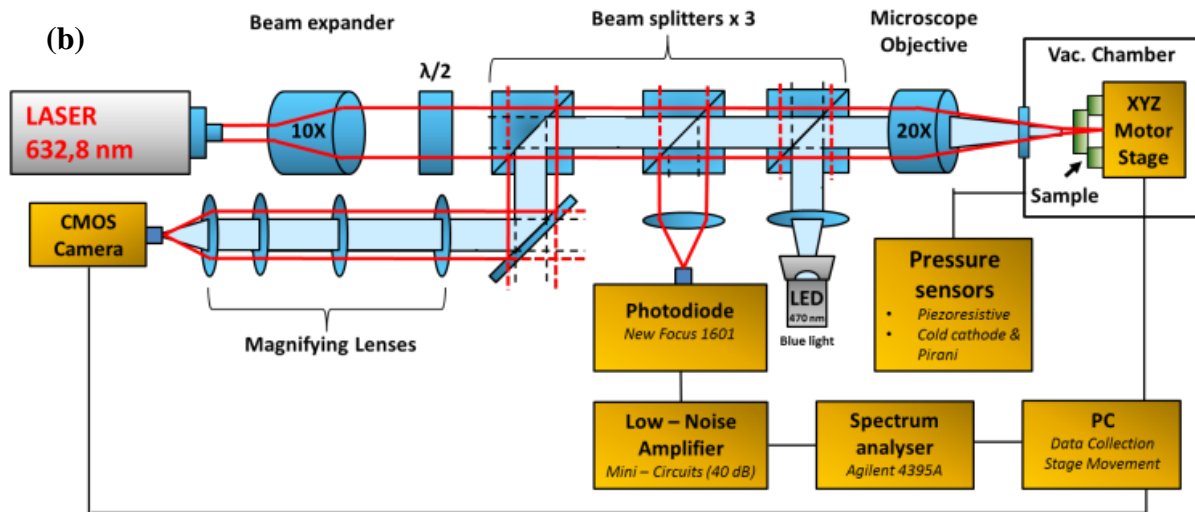
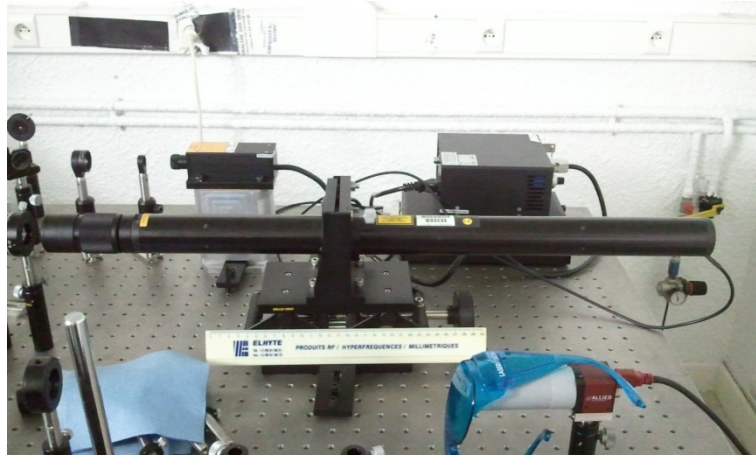


Figure A.1. (a) Photograph and (b) schematics of the optical bench (Fabry-Perot interferometer) used in this study. Note the difference with Figure 3.3.a, which is a simplified view of the setup.

### Electrical components

The laser used as a light source in this study is a 05-LHP-845 model by Melles Griot (Figure A.2, foreground). This laser is a helium-neon laser typically used in optical experiments, and produces 632.8 nm wavelength light (red color) with a minimum rated output power of 30 mW (class IIIb). This laser is linearly polarized to facilitate interferometry. As the laser beam passes through the optical elements, the light is adsorbed and loses its intensity. As a result, measurements carried out with a calibration photodiode showed that only a total light power of around 5 mW reaches the sample. The laser source is clamped tightly to the optical table for stability, and along its light path a beam expander and a microscope lens are installed in front of and behind the beam splitter respectively to facilitate a sharp focus on the sample. A polarizing filter was placed in front of the beam expander to control the intensity of the laser.

In addition to the He-Ne Laser mentioned above, a solid-state laser with the same wavelength (627 nm) is also available as an alternative light source (Figure A.2, background). This laser is a MRL-III-627 produced by CNI. This laser is set beside the He-Ne laser, with its own magnifying lenses and a mirror that joined the beam path on the first beam splitter. Although this laser has higher optical power (100 mW), it was not used during the course of this study due to fluctuations of laser power output.



*Figure A.2. Laser used as a light source for Fabry-Perot interferometry (05-LHP-845 He-Ne laser by Melles Griot). The black boxes in the background are the power source for both lasers. Note the adjustable clamp of the laser, and the beam expander attached to the front of the laser.*

A measurement diode (New Focus 1601) is positioned on the output of the 3<sup>rd</sup> beam splitter (in order to obtain the maximum measurement signal), with a focusing lens on the optical path, as can be seen in Figure 6.3. This diode exhibits DC and AC output signals; the DC output is connected to an oscilloscope for control of laser intensity, while the AC output (relevant for frequency characterization) is connected to the spectrum/network analyzer (Agilent 4395 A). This diode is powered by its own DC power supply. For signal amplification, a low-noise amplifier (40 dB amplification from mini-circuits) and a low-pass filter are installed between the AC output of the diode and the spectrum network analyzer. The cables are shielded using aluminum foil to minimize electrical disturbance and crosstalk. The diode is mounted on a support with micrometer screw for fine-tuning and optimization of the measurement signal.



*Figure A.3. (a) Front view of the diode. The micrometer support of the diode is adjusted so that the beam falls inside the circular glass window at the front of the diode. (b) Back view of the diode. The micrometer support, the amplifier, the power supply, and the coaxial cable carrying the AC and DC signal can be seen.*

The analyzer used in this study is an Agilent 4395A (Figure A.4). This analyzer is capable of being used either in network or spectrum analyzer mode, depending on the requirements. In the network analyzer mode, the analyzer sends an RF signal at a certain frequency as an output and receives the response signal at the same frequency as an input; a scan in the desired frequency range is then done, resulting in the amplitude and phase information of the device's frequency response. This mode is used for observing the frequency response of the device when its actuation is connected to the driving signal by means of *e.g.* a piezo disc or capacitive actuation. In the spectrum analyzer mode, the analyzer records the response of the device at the desired frequency range, without sending an output or driving signal on its own to the device. This mode is used for detecting resonant peaks using thermomechanical actuation, or observing the device harmonics when driven at a specific frequency (such as using a signal generator). Data acquisition is done by connecting the spectrum/network analyzer to a PC that tabulates the data in an Excel format. The analyzer is connected to the piezo disc or device and the measurement diode by coaxial cables with BNC connectors. Specifications of the analyzer are presented in Table A.1.



*Figure A.4. The spectrum/network analyzer used to process the measurement signal from the photodiode (Agilent 4395A).*

Network analyzer specification		Spectrum analyzer specification	
Frequency range	10 Hz to 500 MHz <sup>1</sup>	Frequency range	10 Hz to 500 MHz
Frequency resolution	1 mHz	Noise sidebands	< -104 dBc/Hz typical at 10 kHz offset
Output power range	-50 to 15 dBm	Resolution bandwidth	1 Hz to 1 MHz in 1-3-10 steps
Dynamic range	115 dB @ 10 Hz IFBW	Dynamic range	> 100 dB third-order free dynamic range
Dynamic accuracy	±0.05 dB/0.3 deg.	Level accuracy	±0.8 dB @ 50 MHz
Calibration	Full two-port	Sensitivity	-145 dBm/Hz @ freq. = 10 MHz

Table A.1. Specifications for Agilent 4395A in both network analyzer and spectrum analyzer modes, from the data sheet of the analyzer manual.

## Optical components

Starting from the beginning of the optical path, a 10 × beam expander is installed in front of the laser tube. This beam expander has a function of increasing the laser beam waist size before it passes through the rest of the optical elements. While this seems contradictory to the requirement of small and tightly focused beam required to probe the surface of the MEMS device, this step is necessary since a laser beam diverges due to diffraction, with divergence  $\theta$  proportional to laser wavelength  $\lambda$  and beam waist size  $w$ :

$$\theta = \frac{\lambda}{\pi w} \quad (\text{A.1})$$

Thus, a beam with waist size of 1 mm diverges 10 times more than an identical beam with waist size of 1 cm. Increasing the beam waist size thus reduces the divergence of the beam as it passes through the optical elements, which facilitates final focusing on the device.

A rotating frame holding a quarter wavelength filter (Melles Griot) is installed after the beam expander. Its function is to control the intensity of the laser beam that reaches the sample: by varying the orientation of the filter, the light intensity can be adjusted from maximum power to zero intensity. Then, the beam passes through three beam splitters (see Figure A.5). Unlike what is required for a theoretical setup, which includes only 1 beam splitter, here we need to add two beam splitters in order to enable MEMS device observation and alignment (by using a CCD camera and an illumination diode). This has the effect of cutting the light intensity by 75%, since each splitter cut the light intensity by half.

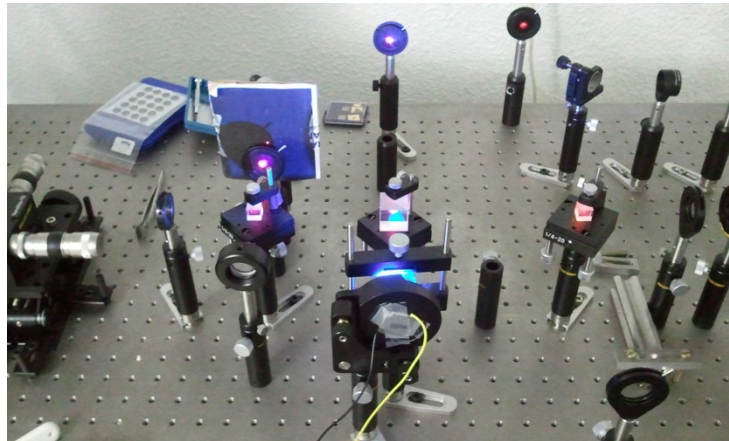


*Figure A.5. Three beam splitters are used in the experimental setup. Two beam splitters are used to provide sample illumination with blue LED (middle splitter) and sample imaging with CCD camera (far right splitter). The third beam splitter (far left) is used to direct the interferometry signal to the photodiode.*

Finally, the laser beam goes through a 20x microscope objective lens (Mitutoyo) for focusing purposes (see Figure A.6). Indeed, the beam that has been enlarged into 1 cm diameter by the beam expander needs to downsize to a spot size of few  $\mu\text{m}$  on the sample surface.



*Figure A.6. Microscope lens used to focus the laser beam onto the sample (placed inside the measurement chamber). The lens is mounted on a micrometer holder for fine-tuning. Note the measurement chamber on the right side, with the optical window and kapton tape holding the heating elements used for chamber cleaning.*

### **Illumination and Imaging Components**

The CCD camera used in the setup is a GUPPY by Allied Vision (see Figure A.7). The camera is powered and connected to a PC with a firewire interface and is capable of taking

pictures and videos of the MEMS sample surface. A magnifying lens and a UV mirror are installed between the CCD camera and the beam splitter, and the magnifying lens is interchangeable in order to enable appropriate magnification for different purposes: small magnification for locating a specific sample in a chip and large magnification for beam positioning and focusing on that sample surface. Due to the different focal length of these lenses, the CCD camera is not permanently fixed to the optical bench, and is movable. A dielectric UV mirror aligned to the beam splitter provides an optical path between the CCD camera and the sample.

A blue diode (470 nm) is positioned before the 2<sup>nd</sup> beam splitter, with a focusing lens in between (Figure A.8). The diode has a maximum current rating of 400 mA, although a value of around 300 mA is typically used in our experiment for the current source. This diode acts as an illumination source for the sample, so that it can be imaged with the CCD camera. The wavelength of the diode is chosen so that it does not interfere with the measurement signal (the measurement diode responds to red light).



*Figure A.7. The CCD camera used for sample imaging and beam focusing, GUPPY from Allied Vision. The cable is connected directly to the PC using firewire interface, which also acts as the power line. The stand is not fixed to the optical table to accommodate different focus length of magnifying lenses in front of it.*



*Figure A.8. The LED used for sample illumination, along with the focusing lens.*

### **The vacuum chamber**

The most conspicuous part of the experimental setup is the vacuum chamber that allows dynamic MEMS measurements under high and low vacuum conditions. While most optical measurements do not inherently require the presence of vacuum environment, it is critical for performance evaluation of MEMS devices. The typical scale and size of a MEMS device is such that vibration damping due to air dominates over the intrinsic damping of the device itself. As an example, a typical nanostructure fabricated in this study has  $Q$  factor in vacuum  $Q_{vacuum}$  around 3 000; the same device measured in atmospheric pressure has a quality ( $Q$ ) factor  $Q_{air}$  around 10-30. A vacuum chamber is therefore necessary in order to evaluate the device's  $Q$  factor under various pressure environments (which represents different practical operating conditions), and extract the intrinsic  $Q$  factor of the device. In addition, the chamber might also be used for the calibration of MEMS pressure sensors.

In addition to the components additionally required to create a vacuum chamber (such as vacuum pumps, purging lines, and pressure sensors), additional features are required to carry out optical interferometry experiments:

1. An optical window for the laser beam and the imaging light to reach the sample inside the chamber.

## Appendix A Experimental Setup for Optical Measurements

2. A sample stage that can move the chip in x, y, and z directions for the purpose of selecting different devices within the same chip and of focusing of the laser beam onto the selected device.
3. An ability to maintain the vacuum without any mechanical vibrations, as normally expected from vacuum pumps.
4. An electrical connection to the sample for piezo or electrical actuation and capacitive sensing.

The vacuum chamber used in this study (commissioned for previous NBS group projects) is manufactured by MECA 2000 division of Vinci Technologies (Figure A.9.a and b). It has one optical window on the front, a plug door held by air pressure on one side, 5 ports for electrical connections and sensors on another side, 1 port for vacuum pumping and 1 for purging on the back, and 1 port located at the top of the chamber to plug an ion pump. Inside the chamber sits a sliding sample stage equipped with a stepper motor for laser beam alignment and focusing. The chamber is positioned at the edge of the optical table in order to accommodate the vacuum and nitrogen purging lines. Unlike the optical components, the chamber's four support pillars are clamped fixed into the optical table. A simple resistance heater is wrapped around the chamber exterior and held using pieces of kapton tape for purpose of chamber heating and cleaning.

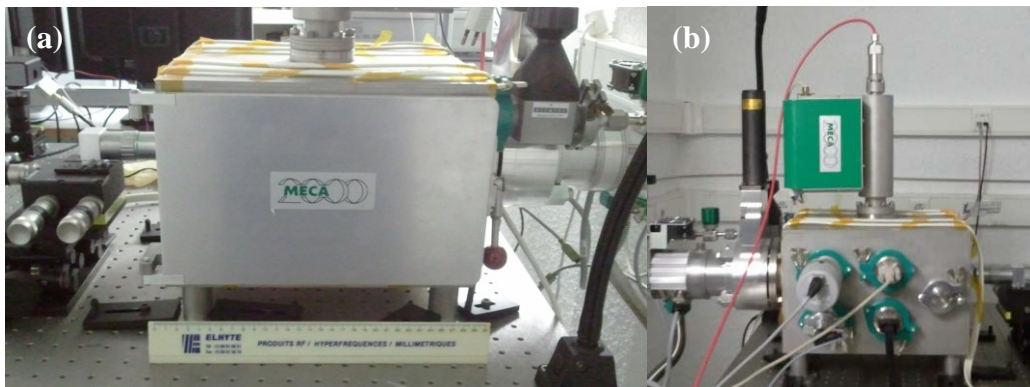


*Figure A.9. (a) Side view of the vacuum chamber, showing the plug door when it is closed. (b) Side view opposite of the door, showing the multiple ports used for pressure sensors and electrical connections. Note the turbo pump on the back, and ion pump on top of the chamber.*

The sample stage located inside the chamber is shown in Figure A.10. It can be divided into 3 components:

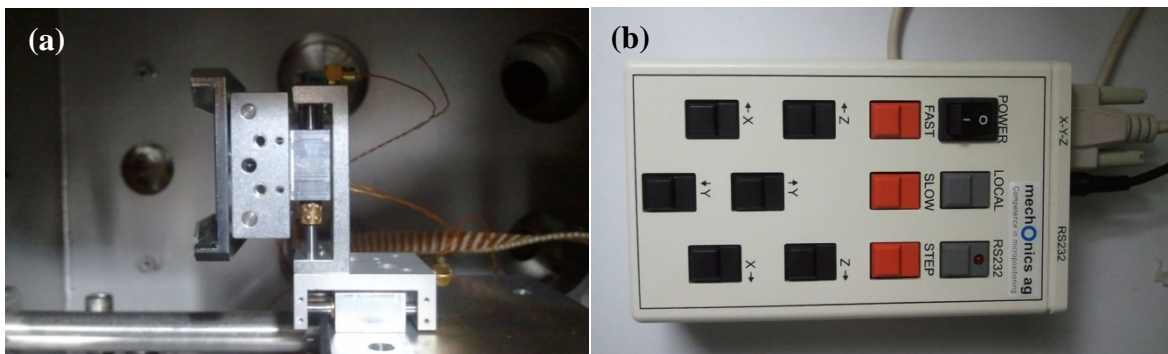
1. The base.
2. The motorized stage, which can be controlled and actuated for laser beam alignment.
3. The sample holder, which holds the sample chip itself.



Figure A.10. The sample stage located inside the vacuum chamber. (a) Base pushed completely towards the optical window, ready for optical measurement. (b) Base retracted for sample placement.

The base is designed so that it can be moved in the z axis, parallel to the direction of the laser beam. It is guided by two cylindrical rails. The base is to be moved completely forward in the direction of the optical window for measurement (Figure A.10.a) and backwards in the direction of the vacuum port (Figure A.10.b) for sample placement. During the measurement, the base is fastened to the rails by an allen screw located on the base.

The motorized stage has three linear piezo motors integrated into it, each for x, y, and z axis displacement (Figure A.11.a). The cables connecting the motors run through a port on the side using an DE-9 plug interface, only 3 of which are connected. The wires are then connected to a piezo control box outside the chamber (Figure A.11.b), which can be directly used to move the stage or remotely operated from the PC. Three movement speeds are available directly through the control box (fast, slow, and step), and controlling the stage through the PC enables definition of the step movements from  $0.3 \mu\text{m}$  to  $200 \mu\text{m}$  nominal value. However, in practice the step size is neither accurate nor symmetrical, and should only be used as a guideline. The stage is designed to accept the sample holder by sliding it into place.



*Figure A.11. (a) Details of the motorized stage, without the sample holder attached. The piezo stepper motor with the wrings can be clearly seen. (b) Piezo -control box connected to the motorized stage. The piezo stepper motor can be controlled by pressing the buttons on the control box directly, or using a PC connected to the control box via the RS 232 interface.*

The sample holder is a metal frame with a metal clamp on each side, which can be fastened by 4 screws (Figure A.12.a). The side of the holder is designed with a screw hole to accommodate a detachable metal handle to pull out the holder from the motorized stage. It is designed to host samples of 2 cm × 2 cm in size, with 1-2 mm thickness. In practice, it is common to use printed circuit board (PCB) of 2 cm × 2 cm in size on which the sample chip is fixed. For passive structures, a PCB with piezo disc (PI ceramics) is used for actuation and a carbon tab is used as an adhesive between the chip and the piezo. Experience has shown that sample size of 1 cm × 1 cm or less is ideal for actuation using piezo disc; larger samples have shown tendencies to produce non-lorentzian resonance peaks, which might be caused by bad coupling between the sample and the piezo. It is recommended that large samples be cut to fit the piezo disc. For active structures with integrated sensing and detection schemes, the chip is glued to a PCB of the same size, which has metal leads, and gold wire bonding is used to connect the chip and the PCB. An example of appropriate samples, as well as the way the sample are attached to the sample holder, are shown in Figure A.12.

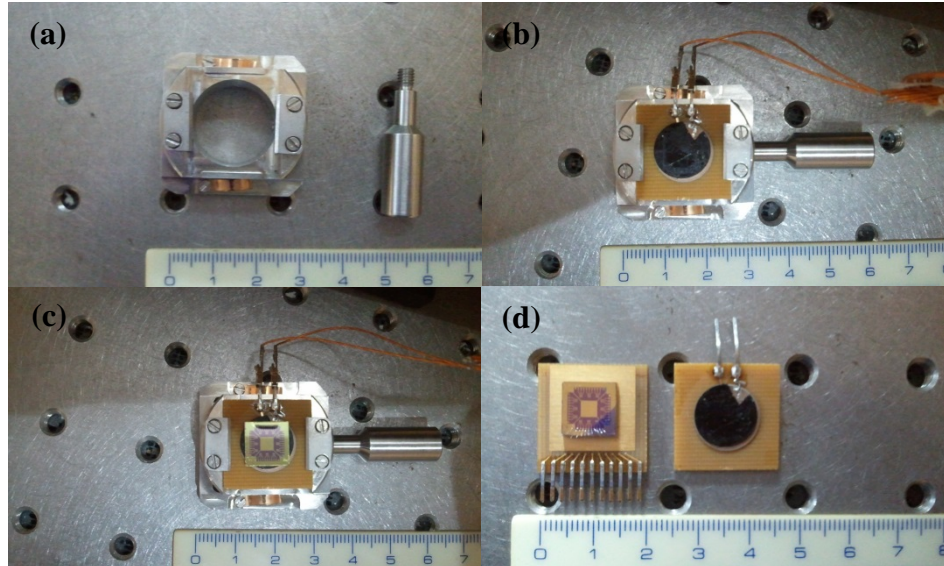


*Figure A.12. (a) Sample holder without any sample, and detachable metal handle on its right. (b) Sample holder with the PCB holding the piezo disc and the metal handle attached. (c) Sample holder with the PCB with piezo disc and a sample containing passive structures on top of it. This sample holder is ready to be put on the motorized stage and measured. (d) An example of samples suitable for the holder: an active device wire-bonded to a PCB with metal leads (left), and a PCB with piezo disc attached. The black surface of the piezo disc is a carbon tab, which is used as adhesive.*

The complete steps taken to mount the sample inside the chamber are as follows. First, nitrile gloves are worn to prevent contamination of the vacuum chamber. Afterwards, the sample is attached into the piezo assembly at the backside using a carbon tab. When the carbon tab has lost its adhesive properties, it is strongly recommended to replace both the carbon tab and the piezo assembly entirely. Attempts to peel the carbon tab from the piezo most likely peels off the upper piezo electrode and results in some parasitic mechanical responses. The wiring of the assembly is then plugged to the connector of the chamber. This requires the wiring port of the chamber to be opened, and the plugs to be connected outside of the chamber. The connection is tested by doing a frequency sweep using the analyzer between 1-20 kHz at 15 dBm. The piezo disc vibrates at an auditory frequency range, and an increasing ringing noise can be heard if the connection is working properly. The sample holder is then slid fully into the piezo stage until it reaches the end of the stage and cannot be pushed anymore; the handle of the sample holder is then unscrewed. The piezo stage is then pushed completely to the measurement window until it reaches a stopper (Figure A.12. b), and the fastening bolt is tightened using the Allen key. Care has to be taken not to let the wirings obstructing the sample before the chamber is closed.

### **The vacuum system**

The vacuum chamber is equipped with three pumps, each fulfilling a different purpose. The primary or the coarser pump is used to achieve low vacuum, which enables the secondary pump to start operating without stalling. The secondary pump is used to achieve high vacuum, which is suitable for measurement of intrinsic Q factor of MEMS devices. To enable measurements without any mechanical vibration from the primary and secondary pumps, an ion pump is used while the two other pumps are turned off. IDP-3 from Varian (Figure A.13.a) is used as the primary pump: it can achieve a maximum vacuum level of 0.33 mbar. V 81-M from Agilent Technologies (Figure A.13.b) is used as the secondary pump. This pump is a turbomolecular pump that can achieve vacuum level around  $10^{-7}$  mbar. A custom-built ion pump from MECA 2000 (Figure A.13.c) is then used to maintain the vacuum level after the primary and secondary pumps are turned off. When the chamber is relatively clean of contaminants, this pump maintains the chamber's vacuum level at around  $10^{-6}$  mbar.



*Figure A.13. Vacuum pumps used to create vacuum in the chamber: (a) The primary pump (IDP-3, Varian), (b) the secondary pump (V 81-M, Agilent Technologies) with the cooling fan and vent valve visible, (c) the ion pump (custom made, MECA 2000). The primary pump is activated by a switch on the pump, while the primary and secondary pumps are operated from (d) the control box, which contains controller for both ion pump (left hand-side) and turbo pump (right hand-side).*

The primary and secondary pumps are connected in series to the back of the vacuum chamber, and the ion pump is connected to a port on top of the vacuum chamber. A cooler fan is attached to the top of the secondary pump, and is plugged manually during its operation. The primary pump is activated by a switch on the pump itself, while the secondary and ion pump is operated via a pump control box (Figure A.13.d).

Since the different pumps operate under very different vacuum regimes, pressure sensors that measure various vacuum ranges are necessary in order to ensure proper pump operation. Three pressure sensors were used to measure the air pressure inside the vacuum chamber:

1. A piezoresistive pressure sensor (VD-8) by Thyracont (Figure A.13.a) that is rated at 3% error and is used for measurements at relatively higher pressures (low vacuum) between 1 mbar and 1 012 mbar. This sensor is particularly useful during measurements of Q factor vs. pressure, since this pressure range is where the molecular damping model of the resonator applies.

## Appendix A Experimental Setup for Optical Measurements

2. A combined Pirani and cold cathode pressure sensor (FRG-700) by Agilent technologies (Figure A.13.b), which is rated at 30% error and can be used for measurements between 1 012 mbar and  $10^{-8}$  mbar. In practice, this sensor is used to check whether the vacuum level is good enough for switching to the ion pump, which is normally done around  $10^{-7}$  mbar.
3. The pressure sensor located in the ion pump. This sensor indicates the vacuum level in the vicinity of the ion pump, and is only active when the ion pump itself is activated. The sensor gives pressure values around 1 order of magnitude lower compared to the FRG-700.

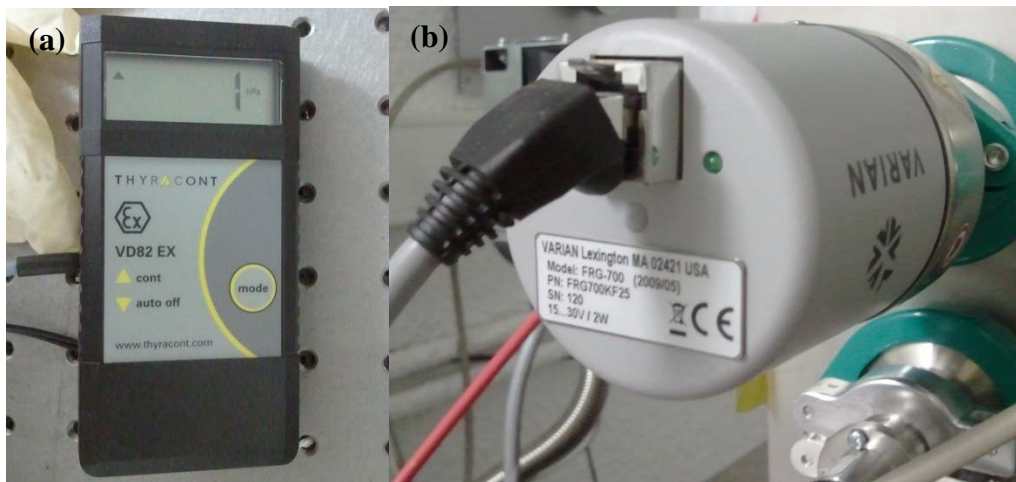
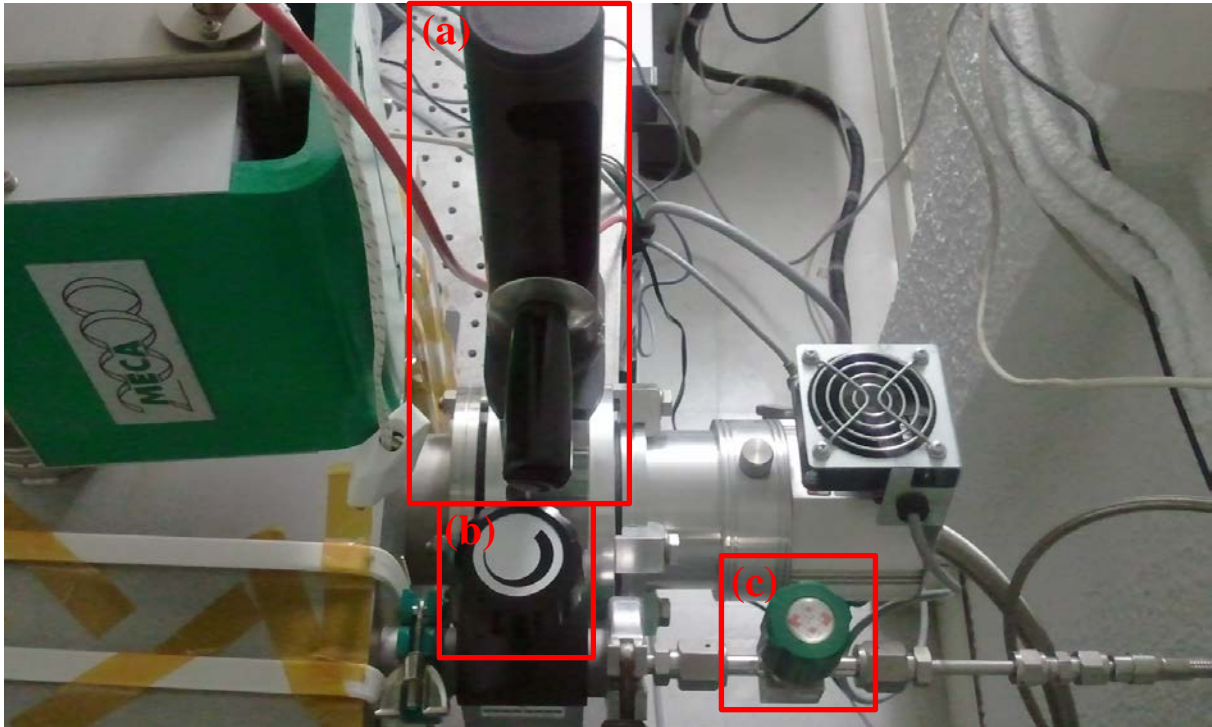


Figure A.14. (a) The display of the piezoresistive pressure sensor, with a resolution of 1 mbar and a measurement range between 1-1012 mbar. (b) The combined Pirani gauge / cold cathode sensor, FRG-700.

The VD-8 has its own portable digital display, while the FRG-700 and the ion pump pressure sensor displays are located in the control box shown in Figure A.14.d.

A series of valves is installed to regulate the air flow between the vacuum chamber and the pumps and the nitrogen purging lines. The access between the chamber and the primary and secondary vacuum pumps is controlled by one gate valve, while the nitrogen flow for purging the chamber is controlled by a diaphragm valve and a leak valve (Figure A.15). The gate valve is operated by moving the handle to the top and bottom position to open and close the valve respectively. The diaphragm valve and the leak valve give a coarse and fine control respectively over the nitrogen flow used for purging. Additionally, a vent valve is located on top of the secondary pump for exposing the vacuum lines between the secondary pump and the primary pump to atmospheric pressure after the gate valve is closed.



*Figure A.15. Valves connected to the vacuum chamber. The gate valve (a) controls the connection between the vacuum pumps and the chamber, and is equipped with a large handle for opening and closing (shown here in closed position). The diaphragm valve (b) and the leak valve (c) controls the connection between the nitrogen purging lines and the chamber.*

When unused, the vacuum chamber is normally kept under primary vacuum (0.1 mbar) or secondary vacuum ( $10^{-6}$  mbar) and the gate valve is closed. Opening the vacuum chamber is done by following these steps. First, all of the vacuum pumps are turned off in the following order: first, the ion pump, second, the secondary pump, and finally the primary pump. Special attention has to be given to ensure that the ion pump is turned off, since it does not emit any sound when operating. After the turbo pump has stopped operating (around 30 minutes after it is shut down), the vent valve located at the turbo pump is opened to let air enter the turbo pump, and closed again. Afterwards, the leak and the diaphragm valves are opened until an increase in pressure can be observed on the piezoresistive pressure sensor. At the same time, the sound of nitrogen entering the chamber should be heard. When the chamber pressure is equal to 1 atm ( $P = 1000$  mbar), the door of the chamber opens naturally. While the door is open, the nitrogen flow should be kept open to prevent contamination from entering the chamber.

Closing the chamber for measurement under vacuum or for shutting down the system is done by following these steps. First, the chamber door is closed and the locking handle lowered

after making sure that the diaphragm, leak, and the vent valve are closed and the gate valve is opened (handle should be on the top). This is important since the chamber is not designed to handle overpressure. Afterwards, the primary pump is turned on to bring the chamber into primary vacuum (in the order of 0.1 mbar). In case of unusual/loud noise, the pump is to be stopped as soon as possible. In normal operation, it is possible to bring the chamber pressure under 0.3 mbar within 10 minutes. To bring the chamber into secondary vacuum, the turbo pump is turned on after the Pirani sensor indicates that the pressure has reached around  $10^{-2}$  mbar. The pumping can be continued until the vacuum level saturates around  $10^{-7}$  mbar.

To do measurements with minimum mechanical vibrations at secondary vacuum ( $10^{-6}$  mbar), only the ion pump should be used. This is done by turning the ion pump on, followed by closing off the gate valve and shutting down the secondary and primary pumps. If the chamber is clean and free of contamination, the ion pump will maintain the chamber pressure level at around  $10^{-6}$  mbar. An increasing vacuum pressure while the ion pump is turned on is a sign of either a leak or chamber contamination. In this case, it might prove necessary to clean the chamber to enable the ion pump to maintain the secondary vacuum.

The procedure taken to clean the chamber of contaminants is described as follows. First, the chamber is closed and brought into the secondary vacuum level as described in the previous paragraphs. Afterwards, the ion pump is turned on without shutting down the primary and secondary vacuum pumps. The heating element of the vacuum chamber is then plugged on; this will cause an increase of pressure due to the evaporation of volatile contaminants. This configuration is kept for at least 48 hours or as required if the contamination is particularly heavy. To test the cleanliness of the chamber after the procedure, the heating element is unplugged and the vacuum chamber is left until it reached room temperature. Afterwards, the gate valve is closed and the primary and the secondary pumps are shut down while only the ion pump is kept in operation. If the chamber is clean and free of contamination, the ion pump will maintain a vacuum at around  $10^{-6}$  mbar.

### **Protocol for Fabry-Perot measurement**

After the sample is mounted as described, the sample is ready for measurement in atmospheric pressure. For measurement under vacuum, the procedure for putting the chamber under vacuum described previously needs to be followed before the measurement can begin. In both cases, the first step of sample measurement is getting the laser spot focused and positioned in the desired location on the sample. This is done by first moving coarsely the piezo stage in z direction until a bright laser dot is clearly observed on the camera. In case where a glaring reflection is observed at the surface of the sample, a protective google might be used and placed in front of the camera to give a clear picture of the laser spot shape. Afterwards, the stage is moved in the x-y plane until the device under interest appears and the laser spot falls onto the area where the maximum amplitude is expected. As an example: for

the 1<sup>st</sup> vibration mode of a cantilever, this area is the edge opposite of the clamping side, while for the 1<sup>st</sup> vibration mode of a circular plate resonator, this area is in the center of the circle.

The second step of the measurement is to locate the resonant peak of the device. A wide frequency span is set around the expected resonant frequency; for the case of this study, a frequency span between 1 MHz-30 MHz is typical. For initial sweep, a measurement bandwidth of 1 kHz and a number of points of 801 provide a good compromise between measurement speed and signal-to-noise ratio. The output power of the device is set to maximum (15 dBm for the Agilent 4395 A) to facilitate the identification of the peak. A well-functioning device will produce a Lorentzian peak close (between 1-3 MHz) to the theoretical resonant frequency. Defective devices will produce multiple peaks at low frequencies (delaminated device) or no peaks at all (buckled device).

The third step of the measurement is the optimization of the measurement signal. This is done by monitoring the diode signal at the resonant peak with sweep width set to 1 Hz, or by simply observing the diode DC output on the oscilloscope. Afterwards, the piezo stage is moved in step mode in x, y, and z direction until the maximum signal amplitude is achieved. The diode position is adjusted using the micrometer screw until the DC signal measured at the oscilloscope is at maximum. Amplifiers might be used between the diode and the spectrum/network analyzer for detection of very weak signals, such as thermomechanical noise in atmospheric pressure.

The final step of the measurement is the data acquisition using the analyzer. For measurements with actuation signals such as passive device with piezo disc attached or active devices, the analyzer is set to the network analyzer mode. In the network analyzer mode, an attempt should be made to observe the frequency response at power level as low as possible to avoid nonlinear effects. For measurements of thermomechanical noise, the analyzer is set to the spectrum analyzer mode. In this mode, averaging and low measurement bandwidth is commonly used due to the low signal-to-noise ratio of thermomechanical measurement, with typical averaging value of 200 times and 3-10 Hz bandwidth. In both cases, the acquired data is saved to a PC in an Excel file format and analyzed.



## Appendix B

### Experimental setup for Capacitive Measurements

The main equipment used for capacitive measurements is a custom-made measurement card built at LAAS shown in Figure B.1. The card has two AC output ports (corresponding to  $V_{AC1}$  and  $V_{AC2}$  in Figure 3.4) with minimum voltage step of 0.1 mV, and maximum amplitude of 800 mV. The input port is connected to a charge amplifier, and has bandwidth filter of 4 kHz and noise magnitude of 25  $\mu$ V. The card is not designed with a DC bias port, and  $V_{DC}$  is provided by a DC power source. Control and measurement using the card is done via a PC linked using a USB interface. The charge amplifier connected to the input port has a bandwidth of 15 MHz and a reference capacitor of 1 pF, which gives a transduction factor of 1 pC/Volt.

Measurement of the sample using capacitive detection is as follows. The two output ports are connected to the two metal leads of the paired devices' top electrodes. The output port of the device to be measured is connected to a DC power source using a T-connector; the  $V_{DC}$  is set at 0 Volt at this stage. If one of the paired devices is not functional due to buckling or short circuit, an external capacitor with similar capacitance (1 pF) can be substituted at the other output port for compensation. The charge amplifier is then connected to the middle pin of the device and plugged into a voltage source.

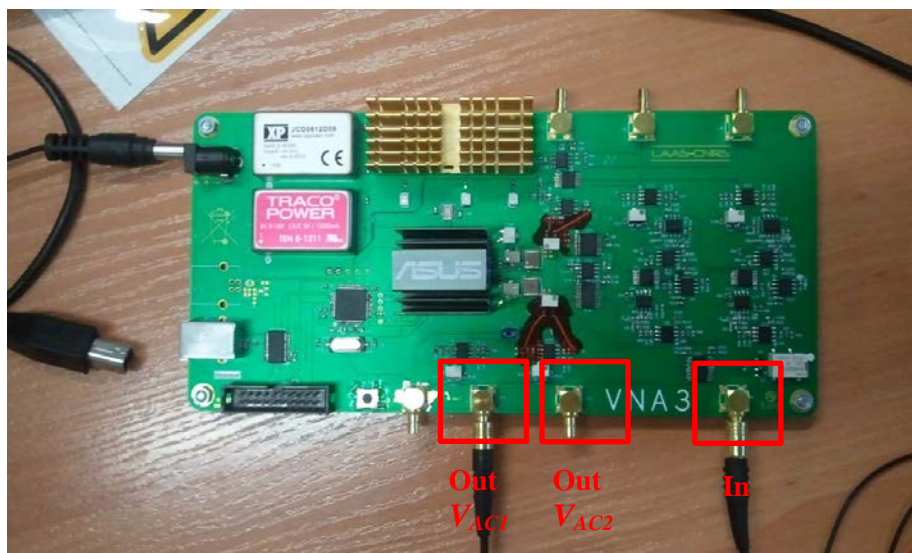


*Figure B.1. Measurement card used for capacitive detection. The card has two outputs for  $V_{AC1}$  and  $V_{AC2}$ , and one input to measure the voltage from the charge amplifier.*

From the PC, the AC voltage is then applied to both output ports, with a phase difference of  $180^\circ$  between the outputs. On the input port, frequency span is adjusted close (around 1 MHz span) to the expected resonant frequency value of the device obtained either through analytical method or optical measurements. The amplitude of  $V_{AC1}$  and  $V_{AC2}$  are then adjusted so that the output signals around the expected resonant frequency cancel out. The  $V_{DC}$  from the voltage source is then increased slowly, taking care not to exceed the pull-in voltage of the device, which varies between 5 to 20 Volts depending on the diameter of the device. Due to the fact that the total parasitic impedance (especially resistance and capacitance) of the device is a function of frequency, this compensation scheme typically does not produce perfectly flat response when viewed in the frequency domain. While the peak response of the device can be clearly seen, it is noted that it is located in a slope. To make the results easier to interpret, the data is subtracted with the background signal at  $V_{DC} = 0$  V, and filtered using the moving average method to remove the noise. This process is illustrated in Figure B.2.

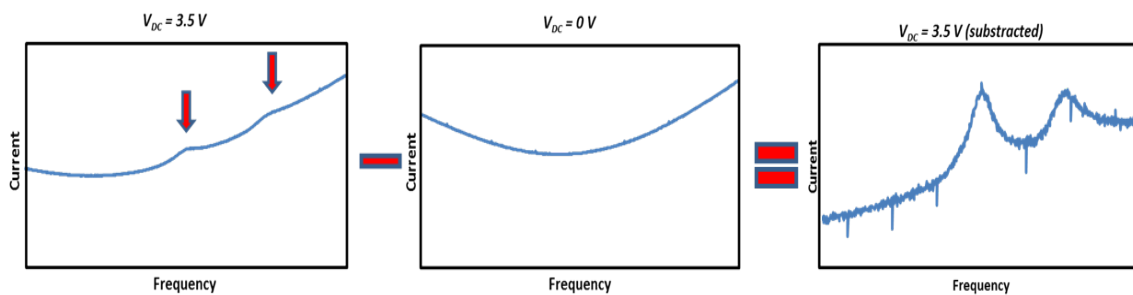


*Figure B.2. Illustration of the process used to extract the frequency response from the raw capacitance measurement data. The data obtained at a certain  $V_{DC}$  bias (in this case 3.5 V for the active plate device with integrated actuation and sensing) showed some resonant peaks (as showcased with arrows), although it is not very clear due to existence of a background current. This data is then subtracted with the data at  $V_{DC} = 0$  V, which provides the background current of the structure. Thus a clearer peak data can be found. The shape of the background current is different at different  $V_{DC}$  due to the existence of parasitic resistance, and thus the resulting peak after subtraction is not leveled. The subtraction, as well as leveling and smoothing of the data is done using Matlab*

**Author** : Adhitya BHASWARA

**Title** : Fabrication of suspended plate MEMS resonators by micro-masonry

**Thesis director** : Liviu NICU and Thierry LEICHLE

**Place and date of the defense** : LAAS – CNRS, 25<sup>th</sup> November 2015

---

## **Summary**

Lately, transfer printing, a technique that is used to transfer diverse materials such as DNA molecules, photoresist, or semiconductor nanowires, has been proven useful for the fabrication of various static silicon structures under the name micro-masonry. The present study explores the suitability of the micro-masonry technique to fabricate MEMS resonators. To this aim, silicon microplates were transfer-printed by microtip polymer stamps onto dedicated oxide bases with integrated cavities in order to create suspended plate structures. The dynamic behavior of fabricated passive structures was studied under atmospheric pressure and vacuum using both external piezo-actuation and thermomechanical noise. Then, active MEMS resonators with integrated electrostatic actuation and capacitive sensing were fabricated using additional post-processing steps. These devices were fully characterized under atmospheric pressure. The intrinsic Q factor of fabricated devices is in the range of 3000, which is sufficient for practical sensing applications in atmospheric pressure and liquid. We have demonstrated that since the bonding between the plate and the device is rigid enough to prevent mechanical crosstalk between different cavities in the same base, multiple resonators can be conveniently realized in a single printing step. This thesis work shows that micro-masonry is a powerful technique for the simple fabrication of sealed MEMS plate resonators.

---

**Keywords** : MEMS, Resonator, Parallel plate capacitor, Interferometry, Soft lithography

---

**Discipline** : Micro and nanosystems

**Auteur** : Adhitya BHASWARA

**Titre** : Fabrication de nanoplaques résonantes à l'aide de la micro-maçonnerie

**Directeurs de thèse** : Liviu NICU et Thierry LEICHLE

**Lieu et date de soutenance** : LAAS – CNRS le 25 Novembre 2015

---

## **Résumé**

L'impression par transfert, une technique utilisée pour transférer divers matériaux tels que des molécules d'ADN, de la résine photosensible ou des nanofils semi-conducteurs, s'est dernièrement révélée utile pour la réalisation de structures de silicium statiques sous le nom de micro-maçonnerie. L'étude présentée ici explore le potentiel de la technique de micro-maçonnerie pour la fabrication de résonateurs MEMS. Dans ce but, des microplaques de silicium ont été transférées sur des couches d'oxyde avec cavités intégrées à l'aide de timbres de polymère afin de créer des structures de type plaques suspendues. Le comportement dynamique de ces structures passives a été étudié sous pression atmosphérique et sous vide en utilisant une excitation externe par pastille piézo-électrique mais aussi le bruit thermomécanique. Par la suite, des résonateurs MEMS actifs, à actionnement électrostatique et détection capacitive intégrés, ont été fabriqués en utilisant des étapes supplémentaires de fabrication après impression. Ces dispositifs ont été caractérisés sous pression atmosphérique. Les facteurs de qualité intrinsèques des dispositifs fabriqués ont été évalués à 3000, ce qui est suffisant pour les applications de mesure à pression atmosphérique et en milieu liquide. Nous avons démontré que, puisque l'adhérence entre la plaque et l'oxyde est suffisamment forte pour empêcher une diaphonie mécanique entre les différentes cavités d'une même base, plusieurs résonateurs peuvent être facilement réalisés en une seule étape d'impression. Ce travail de thèse montre que la micro-maçonnerie est une technique simple et efficace pour la réalisation de résonateurs MEMS actifs de type plaque à cavité scellée.

---

**Mots-clés** : Microsystèmes, Résonateur, Condensateur à plaques parallèles, Interférométrie, Lithographie douce

---

**Discipline** : Micro et nano systèmes